# Longitudinal Single-Spin Asymmetry and Cross Section for $W^{\pm}$ Boson Production in Polarized Proton-Proton Collisions at $\sqrt{s} = 500$ GeV

Justin R. Stevens

Submitted to the faculty of the University Graduate School
in partial fulfillment of the requirements
for the degree
Doctor of Philosophy
in the Department of Physics,
Indiana University
June 2012

Accepted by the Graduate Faculty, Indiana University, in partial fulfillment of the requirements of the degree of Doctor of Philosophy.

Doctoral Committee

Scott W. Wissink(Chair)

Charles J. Horowitz

William W. Jacobs

May 10, 2012

W. Michael Snow

# Acknowledgements

First, I would like to acknowledge and thank the members of my committee. In particular to my adviser, Scott Wissink, thank you for your guidance and encouragement during my graduate career at IU, and helping to shape this thesis and analysis. To Will Jacobs, thank you for your passion and energy, and teaching me everything I know about the electromagnetic calorimeters at STAR. It was truly a privilege to work with you both.

To the members of the "W Team" at STAR, especially Jan Balewski, Ross Corrliss, Joe Seele, Bernd Surrow, and Gene Van Buren, thank you for all your efforts. It was a great privilege to work with you during this exciting analysis. I am also grateful to the STAR software and computing team, in particular Jerome Lauret and Gene Van Buren, for providing me the opportunity to serve as a software coordinator for the $EMC^2$ group, and for their guidance in this role. To the remaining members of the STAR group at IU (both past and present): Seema Dhamija, Pibero Djawotho, Weihong He, Brian Page, Ilya Selyuzhenkov, Mike Skoby, Jim Sowinski, and Anselm Vossen, thanks for your friendship and the helpful discussions over the last five years. I would be remiss if I did not also express my gratitude to Andy Bacher and Steve Vigdor for inviting me to Bloomington through the REU program six years ago, and for motivating me to continue in nuclear physics research.

To my parents, thank you for encouraging me to dream big and demonstrating the hard work necessary to make them come true. Finally, to my wife Jaime, who has supported and encouraged me through the highs and lows all while managing to raise our two boys and continuing to support our family, thank you for your constant love and support. I would not be where I am today without you.

Justin R. Stevens

# Longitudinal Single-Spin Asymmetry and Cross Section for $W^{\pm}$ Boson Production in Polarized Proton-Proton Collisions at $\sqrt{s} = 500$ GeV

Measurements of $W^{\pm}$ boson production in longitudinally polarized proton-proton collisions at RHIC provide a new means of studying the spin-flavor asymmetries of the proton sea quark distributions. $W^{-(+)}$ bosons are produced in $\bar{u} + d\,(\bar{d} + u)$ collisions and can be detected through their leptonic decays, $e^- + \bar{\nu}_e\,(e^+ + \nu_e)$, where only the charged lepton is observed, with a large missing transverse energy opposite in azimuth. Details of the $W \to e\nu$ event reconstruction algorithm will be described, including the use of the large acceptance of the Time Projection Chamber and Electromagnetic Calorimeters to identify isolated high-$p_T$ $e^{\pm}$ candidates and reduce the significant QCD background to identify a clear $W$ signal.

First measurements of the parity-violating single-spin asymmetry for $W$ production and the $W \to e\nu$ and $Z/\gamma^* \to e^+e^-$ production cross sections will be reported, as well as the $\sigma_{W^+}/\sigma_{W^-}$ cross section ratio. These results are based on 13.2 pb$^{-1}$ of data recorded during 2009 in longitudinally polarized proton-proton collisions at $\sqrt{s} = 500$ GeV by the STAR experiment at RHIC. Theoretical predictions for the spin asymmetries and cross sections, calculated using recent polarized and unpolarized parton distribution functions, are consistent with the measured values.

Scott W. Wissink(Chair)

Charles J. Horowitz

William W. Jacobs

W. Michael Snow

# Contents

**Acknowledgements** **iii**

**Abstract** **iv**

**1 Introduction and Theory** **1**
1.1 Proton Structure . . . 1
1.1.1 Parton Distribution Functions . . . 4
1.1.2 Sea Quark Flavor Asymmetry . . . 8
1.1.3 Helicity Structure of the Proton . . . 13
1.2 $W$ Boson Production in Polarized Proton-Proton Collisions . . . 18
1.3 Structure of This Thesis . . . 25

**2 Experimental Setup** **26**
2.1 Polarized Protons at RHIC . . . 26
2.1.1 Accelerator Complex . . . 27
2.1.2 Polarimeters . . . 31
2.2 Solenoidal Tracker at RHIC (STAR) . . . 35
2.2.1 Time Projection Chamber . . . 36
2.2.2 Barrel Electromagnetic Calorimeter . . . 38
2.2.3 Endcap Electromagnetic Calorimeter . . . 40

**3 Data and Simulation Samples** **41**
3.1 Trigger Selection . . . 42
3.2 Integrated Luminosity Measurement . . . 43
3.3 Simulation Samples . . . 45
3.3.1 Pile-up Effects . . . 45

**4 $W$ and $Z$ Signal Reconstruction** **50**
4.1 Primary Vertex Finder . . . 51
4.2 Identification of High-$E_T$ Isolated $e^{\pm}$ Candidates . . . 53
4.2.1 Track Quality Requirements . . . 53
4.2.2 Track and Cluster Matching . . . 55
4.2.3 Isolation Requirements . . . 56
4.3 $W$ Candidate Event Selection . . . 59
4.3.1 Signed $P_T$-Balance Requirement . . . 59

4.3.2 Reduction of Background by Cuts . . . 61
4.3.3 Charge Sign Reconstruction . . . 61
4.3.4 Charge Separated Yields . . . 63
4.4 $Z$ Candidate Event Selection . . . 64
4.4.1 Reduction of Background by Cuts . . . 64

**5 Background Estimation** **67**
5.1 Background Estimation for $W$ Signal . . . 67
5.1.1 $W \to \tau\nu$ Background . . . 68
5.1.2 $Z \to e^+e^-$ Background . . . 69
5.1.3 Second EEMC Background . . . 70
5.1.4 Data-driven QCD Background . . . 71
5.1.5 $Z \to e^+e^-$ Events in the QCD Background Distribution . . . 74
5.1.6 Summary of Background Contributions to the $W$ signal . . . 74
5.2 Background Estimation for $Z$ Signal . . . 75
5.3 Comparison of Data and Simulation . . . 76

**6 Cross Section Analysis** **79**
6.1 Efficiency Corrections . . . 81
6.1.1 $W$ Efficiency Correction Factors . . . 81
6.1.2 $Z$ Efficiency Correction Factors . . . 97
6.2 Acceptance Corrections . . . 101
6.3 Results . . . 103
6.3.1 $W^+$ and $W^-$ Cross Sections . . . 103
6.3.2 $Z/\gamma^*$ Cross Section . . . 105
6.3.3 $W^+/W^-$ Cross Section Ratio . . . 106
6.4 Theory Calculations . . . 108

**7 Spin Asymmetry Analysis** **110**
7.1 Extraction of $A_L$ from Spin Dependent Yields . . . 111
7.2 Beam Polarization . . . 113
7.3 Spin Patterns . . . 114
7.4 Relative Luminosity . . . 117
7.5 Background Corrections . . . 119
7.6 Results . . . 122

**8 Conclusions and Outlook** **124**

**A Jet finding parameters** **126**

**B RHIC Fill Polarization Values** **128**

**C List of STAR Runs** **130**

# List of Tables


3.1 Summary of embedded Monte-Carlo samples. . . . . 45

5.1 Summary of background yield contributions to the $W$ signals with $E_T^e > 25$ GeV and $|\eta_e| < 1$. . . . . 75

6.1 $W$ trigger efficiency for different $E_T^e$ bins . . . . . 86
6.2 Track quality cut efficiencies and corrections for re-weighting the simulations by the data reconstructed $1/p_T$ distribution. . . . . 90
6.3 Total tracking efficiencies and corrections for re-weighting the simulations by the data reconstructed $1/p_T$ distribution. . . . . 90
6.4 TPC sectors with dead regions caused by electronics malfunctions. . . . . 92
6.5 $W$ algorithm efficiencies for different $E_T$ bins . . . . . 94
6.6 Summary of acceptance values calculated with the FEWZ program. The MSTW 2008 NLO values are used for the total cross section calculations. . 101
6.7 Summary of the relative uncertainties in the acceptance correction factors, $A_W$ and $A_Z$, as computed by the FEWZ program. . . . . 102
6.8 Summary of input values for the $W \to e\nu$ fiducial cross section measurement, with their statistical, systematic, and luminosity uncertainties. As noted in Sec. 6.1.1, an $E_T^e$-dependent efficiency correction factor is used for the actual cross section measurement, and only the average value is given here. . . . . 103
6.9 Summary of input values for the $Z \to e^+e^-$ fiducial cross section, with their statistical, systematic, and luminosity uncertainties. . . . . 105
6.10 Measurements of the $W$ cross section ratio, $R_W$, for the two $e^\pm$ pseudorapidity bins. . . . . 106
6.11 Summary of FEWZ and RHICBOS cross section calculations and uncertainties at $\sqrt{s} = 500$GeV. The $Z/\gamma^*$ values are defined within the invariant mass range of $70 < m_{e^+e^-} < 110$ GeV/$c^2$. . . . . 109

7.1 Correspondence of spin-4 value and helicity state of the blue and yellow colliding beams at STAR. . . . . 115
7.2 Spin-dependent yields for the QCD background events used for relative luminosity corrections and the relative luminosity correction factors, $R_i$. . . . . 118
7.3 Summary of background contributions to the "observed" $A_L$ (see Eq. 7.14). 121

B.1 Measured beam polarizations and uncertainties reported by the polarimetery group for the RHIC fills in 2009 used in the asymmetry analysis. . . . . 129

# List of Figures


1.1 Feynman diagram for Deep Inelastic Scattering of a charged lepton beam on a proton target. . . . . 2
1.2 Parton distribution functions from the MSTW 2008 [1] set evaluated at $Q^2 = 10$ GeV$^2$ and $10^4$ GeV$^2$. . . . . 6
1.3 The $\bar{d}(x)/\bar{u}(x)$ ratio measured by the E866/NuSea [2] and NA51 [3] collaborations. The curves are parametrizations from a variety parton distributions function sets, see Ref. [4] for details. . . . . 10
1.4 The difference between the $\bar{u}$ and $\bar{d}$ helicity distribution at $Q^2 = 10$ GeV$^2$ from the DSSV global analysis [5]. The green (yellow) bands represent the $\Delta\chi^2 = 1$ ($\Delta\chi^2/\chi^2 = 2\%$) uncertainties of the global fit. . . . . 16
1.5 The difference between the $\bar{u}$ and $\bar{d}$ quark helicity distributions extracted from SIDIS data at the COMPASS experiment [6]. The model curves are explained further in the text. . . . . 17
1.6 Feynman diagrams for $W^+$ boson production in polarized $pp$ collisions [7]. In (a) the polarized proton provides the $u$ quark, while in (b) the $\bar{d}$ quark is a constituent of the polarized proton. The helicity of the proton (quark) is indicated by the subscript (superscript) on the quark coming from the polarized proton. . . . . 18
1.7 Diagrams illustrating the helicity configurations of $W^-$ (left) and $W^+$ (right) production [8]. The single arrows ($\rightarrow$) indicate the particle direction of motion, while the double arrows ($\Rightarrow$) indicate the spin direction. The incoming quark and antiquark with fixed helicity are shown above the $z$ axis, while the outgoing $e^\pm$ and neutrino are shown below it. . . . . 19
1.8 Predictions for the longitudinal single-spin asymmetry $A_L$ for $W^\pm$ production at $\sqrt{s} = 500$ GeV, as a function of the decay $e^\pm$ pseudorapidity. The curves from different helicity distributions are discussed in Ref. [9]. . . . . 23

2.1 Diagram of the Relativistic Heavy Ion Collider complex. . . . . 28
2.2 A cross section view of the pC polarimeter with six silicon detectors inside the beam pipe. . . . . 31
2.3 Diagram of H-Jet polarimeter. . . . . 33
2.4 $W$ candidate event display embedded in a schematic of the STAR detector. Descriptions of the subsystems relevant for this analysis are given in Sec. 2.2 35

3.1 Trigger rate as a function of vernier scan beam displacement in the $x$ and $y$ directions. The transverse beam widths ($\sigma_x$ and $\sigma_y$) and maximum trigger rate ($R_{ver}^{max}$) were extracted from the fit, which is superimposed. . . . . 44
3.2 Event display of all TPC tracks recorded in a typical $pp$ event at $\sqrt{s}$=500 GeV in 2009. The vast majority of tracks are not from the triggered collision, but are instead due to pile-up as described in the text. . . . . 46
3.3 Raw distributions of zero-bias events and integrated luminosity using each zero-bias event once.
Top row (L to R): (# zero-bias events)/(Integ. Lumi.) vs RunID; Integ. Lumi. vs RunID; (# zero-bias events)/(Integ. Lumi.) vs. ZDC coin. rate.
Bottom row (L to R) Total # zero-bias events vs ZDC coin. rate; Total Integ. Lumi. vs ZDC coin. rate; Total (# zero-bias events)/(Integ. Lumi.) vs ZDC coin. rate. . . . . 48
3.4 Total integrated luminosity as a function of ZDC coincidence rate (blue) and normalized number of zero-bias events as a function of ZDC coincidence rate. 49
3.5 $z_{\text{vertex}}$ distributions of data (black), generated embedding (blue), and re-weighted embedding (red). . . . . 49

4.1 Properties of primary vertices reconstructed by PPV: a) rank of all vertices, b) $z_{\text{vertex}}$ distribution for vertices with rank $>$ 0, and c) rank of vertices for reconstructed $W$ candidates (described in Sec. 4.3). . . . . 52
4.2 Track quality variables, where the values of the quality requirements are shown in red: a) Number of TPC points used in track reconstruction, b) Fraction of the maximum number of TPC points allowed used in track reconstruction, c) Radius of the track hit nearest to the beamline, and d) Radius of the track hit farthest from the beamline. . . . . 54
4.3 Diagram of extrapolating the candidate $e^{\pm}$ track to the front of the BEMC tower grid and reconstruction of the highest $E_T$ 2×2 tower cluster pointed to by the track, as well as the 4×4 tower cluster used in the isolation requirement described in Sec. 4.2.3. . . . . 55
4.4 Distributions for matching candidate track and BEMC tower clusters for data and $W \to e\nu$ MC: (a) and (d) 2×2 cluster $E_T$, (b) and (e) 2D distance between extrapolated track and centroid of tower cluster vs. $E_T^e$, (c) and (f) 2D distance between extrapolated track and centroid of tower cluster. . . . . 56
4.5 $e^{\pm}$ candidate isolation cut ratio distributions for data and $W \to e\nu$ MC: (a) and (c) Cluster isolation ratio $E_T^e/E_T^{4\times4}$; (b) and (d) Near-side cone sum ratio $E_T^e/E_T^{\Delta R<0.7}$. . . . . 57
4.6 Diagram of an $e^{\pm}$ candidate (red) in the transverse plane, surrounded by a "near-side cone" (pink) in which the BEMC and EEMC tower $E_T$ and TPC track $p_T$ are summed to determine $E_T^{\Delta R<0.7}$. The purple region is where the transverse components of the reconstructed jet momenta are summed to construct the $p_T$-balance vector for $W$ event selection as described in Sec. 4.3. 58
4.7 Signed $p_T$-balance vs. $E_T^e$ for data (a) and $W \to e\nu$ MC (b). . . . . 60
4.8 Candidate $E_T^e$ distribution from the data after various cuts described above. 61

4.9 GEANT simulation of separation distance between a positron and electron with $p_T = 5$ GeV/$c$ bending in the 0.5 T magnetic field at STAR. . . . . 62
4.10 Product of the reconstructed candidate TPC track charge sign and $1/p_T$ as a function of $E_T^e$ measured in BEMC towers for events satisfying all the $W$ candidate event selection requirements. Global tracks are on the left and primary tracks on the right. . . . . 63
4.11 Raw $W$ candidate yields as a function of $E_T^e$ after passing all selection cuts ($W^+$ on the left and $W^-$ on the right). . . . . 64
4.12 Reconstructed $e^+e^-$ invariant mass distributions after the various cuts described in section 4.2 have been applied. . . . . 65
4.13 Invariant mass distribution of the final $Z$ candidate yield, compared to the $Z/\gamma*$ signal MC yield. . . . . 66

5.1 $W \to \tau\nu$ background contributions (brown), corrected for polarization effects, plotted along with the raw $W$ candidate yields for comparison ($W^+$ on the left and $W^-$ on the right). . . . . 69
5.2 $Z/\gamma^* \to e^+e^-$ background contribution (blue) plotted along with the raw $W$ candidate yield for comparison ($W^+$ on the left and $W^-$ on the right). . . . 70
5.3 Second EEMC background contribution (green) plotted along with the raw $W$ candidate yield for comparison ($W^+$ on the left and $W^-$ on the right). . 72
5.4 Normalized data-driven QCD background shape contributions (light blue) plotted along with the raw $W$ candidate yields ($W^+$ on the left and $W^-$ on the right). . . . . 73
5.5 Reconstructed invariant mass of same charge-sign lepton pairs after applying various cuts, as described in Sec. 4.2. . . . . 76
5.6 $E_T^e$ distribution of $W^+$ (left) and $W^-$ (right) candidate events, background components, and $W \to e\nu$ MC signal for comparison. Note the factor of two difference in the vertical scales. The various background contributions and $W \to e\nu$ MC signal are "stacked" on top of each other for comparison to the data. . . . . 77
5.7 Lepton pseudorapidity distribution of $W^+$ (left) and $W^-$ (right) candidate events, background components, and $W \to e\nu$ MC signal for comparison. The various background contributions and $W \to e\nu$ MC signal are "stacked" on top of each other for comparison to the data. . . . . 78

6.1 $W^+$ trigger efficiency as a function of physical $\eta_e$ (a), detector $\eta_e$ (b), $E_T^e$(c), and $\phi_e$ modulo 12 degrees (d). . . . . 83
6.2 $W^-$ trigger efficiency as a function of physical $\eta_e$ (a), detector $\eta_e$ (b), $E_T^e$(c), and $\phi_e$ modulo 12 degrees (d). . . . . 84
6.3 Detector $\eta_e$ distribution of $e^-$ tracks from the $W^-$ MC sample for four bins in $E_T^e$. . . . . 85
6.4 $W^+$ vertex finding efficiency as a function of $z_{\text{vertex}}$ (a) and ZDC coincidence rate (b). . . . . 87
6.5 $W^-$ vertex finding efficiency as a function of $z_{\text{vertex}}$ (a) and ZDC coincidence rate (b). . . . . 87

6.6 Reconstructed track $1/p_T$ distributions for $W^{\pm}$candidates satisfying all $W$ signal requirements with $E_T^e > 25$ GeV for the data and simulation samples, displayed in the left and middle plots, respectively. The right plot shows the ratio of data to simulation distributions. . . . . 88
6.7 Track quality cut efficiency vs reconstructed track $1/p_T$ for $W^+$ (left) and $W^-$ (right). . . . . 89
6.8 $W^+$ tracking efficiency as a function of ZDC coincidence rate (a) and $\phi_e$ (b). 91
6.9 $W^-$ tracking efficiency as a function of ZDC coincidence rate (a) and $\phi_e$ (b). 91
6.10 $W^+$ algorithm efficiencies as a function of $E_T^e$ and the ZDC coincidence rate. 93
6.11 $W^-$ algorithm efficiencies as a function of $E_T^e$ and the ZDC coincidence rate. 93
6.12 $W^+$ distributions relevant to the $W$ reconstruction algorithm cuts, each as a function of $E_T^e$. (a) 3D distance between track and tower centroid, (b) cluster ratio $E_T^e/E_T^{4\times4}$, (c) near-side cone sum ratio $E_T^e/E_T^{\Delta R<0.7}$, and (d) signed $P_T$-Balance. . . . . 95
6.13 $W^-$ distributions relevant to the $W$ reconstruction algorithm cuts, each as a function of $E_T^e$. (a) 3D distance between track and tower centroid, (b) cluster ratio $E_T^e/E_T^{4\times4}$, (c) near-side cone sum ratio $E_T^e/E_T^{\Delta R<0.7}$, and (d) signed $P_T$-Balance. . . . . 96
6.14 $Z$ trigger efficiency plotted as a function of $m_{e^+e^-}$ and the ZDC coincidence rate. . . . . 98
6.15 $Z$ vertex finding efficiency plotted as a function of $m_{e^+e^-}$ and the ZDC coincidence rate. . . . . 99
6.16 $Z$ tracking efficiency plotted as a function of $m_{e^+e^-}$ and the ZDC coincidence rate. . . . . 100
6.17 $Z$ algorithm efficiency plotted as a function of $m_{e^+e^-}$ and the ZDC coincidence rate. . . . . 100
6.18 Measurements of the $W^{\pm}$ and $Z$ ($70 < m_{e^+e^-} < 110$ GeV/$c^2$) total cross section times branching ratio as a function of center-of-mass energy. For the $W^{\pm}$ cross sections in $pp$ collisions, the closed symbols represent $W^+$ and the open symbols represent $W^-$. The theory curves are from the FEWZ program at NLO using the MSTW 2008 PDF set. . . . . 104
6.19 $W$ cross section ratio, $R_W$, for two $e^{\pm}$ pseudorapidity bins. Theory calculations at NLO from the FEWZ program using the MSTW 2008 and CTEQ 6.6 PDF sets (with 90% confidence level error eigenvector uncertainties) are shown for comparison. . . . . 107

7.1 Polarization of the blue (top) and yellow (bottom) beams corrected for polarization profile vs. RHIC fill number, as reported in Ref. [10]. . . . . 113
7.2 Cartoon of one particular spin pattern for the blue and yellow beams colliding at the STAR interaction region. . . . . 114
7.3 Correlation of STAR spin-4 value (*i.e.,* two-beam helicity combination) and the bunch crossing ID at STAR for each of the four fill polarization patterns used in 2009. . . . . 116

7.4 Spin asymmetries, defined in Eqs. 7.6-7.10 and corrected for relative luminosity and backgrounds, for $W^+$ (left) and $W^-$ (right) with $|\eta_e| < 1$ and $25 < E_T^e < 50$ GeV. . . . . 122
7.5 Longitudinal single-spin asymmetry, $A_L$, for $W^\pm$ production as a function of $e^\pm$ pseudorapidity. . . . . 123

# Chapter 1

# Introduction and Theory

## 1.1 Proton Structure

Although the proton is a basic building block of the atomic nuclei that make up most of the matter around us and has been studied intensely for many years, our understanding of the internal structure of this particle remains incomplete. The study of the proton's internal structure has led to many exciting discoveries and exposed some interesting puzzles, and also limitations, in our understanding of the strong interaction, which will be discussed later in this chapter. One of our primary tools for studying the internal structure of the nucleon is Deep Inelastic Scattering (DIS), in which a charged lepton beam is inelastically scattered from a target or beam of nucleons or nuclei at large momentum transfers. Some of the relevant aspects of DIS will be briefly described in this section; for a more thorough review see Refs. [11, 12, 13, 14].

In the case of inelastic electron scattering with a proton target (shown in Fig. 1.1), the unpolarized cross section can be written as

$$\frac{d\sigma}{dE'd\Omega} = \frac{4\alpha^2 E'^2}{Q^4}\left(W_2(\nu, Q^2)\cos^2\frac{\theta}{2} + 2W_1(\nu, Q^2)\sin^2\frac{\theta}{2}\right), \tag{1.1}$$

where $\alpha$ is the fine structure constant, $E$ ($E'$) is the incident (scattered) lepton energy, $\theta$

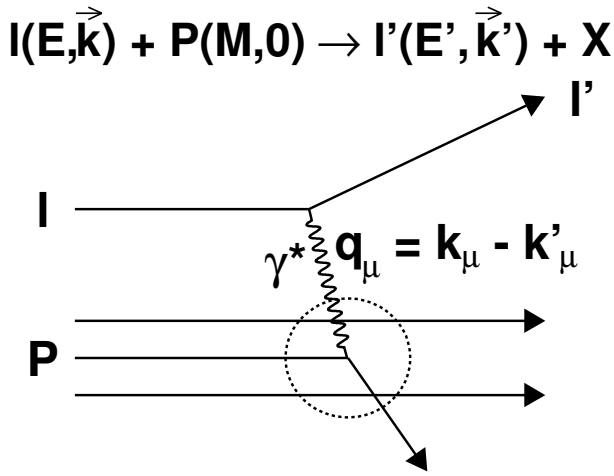


Figure 1.1: Feynman diagram for Deep Inelastic Scattering of a charged lepton beam on a proton target.

is the lepton scattering angle, $Q^2 = -q^2$ is the momentum transfer of the virtual photon, $\nu \equiv E - E'$ is the energy loss of the scattered electron, and $W_1$ and $W_2$ are the proton inelastic structure functions which depend on both $\nu$ and $Q^2$.

In 1969, Bjorken proposed [15] that at large $Q^2$ the inelastic structure function's dependence on $\nu$ and $Q^2$ could be reduced to a single dimensionless scaling variable $x = Q^2/2M\nu$, which has become known as Bjorken-$x$. The structure functions can thus be re-expressed as $F_1(x) = MW_1(\nu, Q^2)$ and $F_2(x) = \nu W_2(\nu, Q^2)$. This simplification of the structure functions, referred to as Bjorken scaling, was confirmed by early DIS measurements in the late 1960s [16, 17].

One implication of Bjorken scaling is that at high $Q^2$, the inelastic scattering process probes very short distance scales, and can therefore resolve point-like constituents inside the proton. Feynman developed a model [18] of these constituent particle interactions in DIS, known as the parton model, which yields the same scaling behavior observed in experiment. In this model, inelastic *ep* scattering at high $Q^2$ can be understood as the incoherent sum of elastic scattering of the electron from the quasi-free, point-like constituent particles of the proton, known as partons.

Bjorken and Paschos [19] later proposed quarks, which had been predicted in 1964 by Gell-Mann [20] and Zweig [21, 22], as candidates for the parton constituents of the proton. In this quark-parton model, the proton is viewed as being composed of three quarks which carry a large fraction of the proton's momentum (called "valence" quarks) and a collection of quark-antiquark pairs (referred to as "sea" quarks) which accounted for the large DIS cross section observed at low Bjorken-$x$. Kuti and Weisskopf [23] developed a more detailed quark-parton model which included gluons as the neutral force carriers that bind together the quarks in the proton, and account for the remainder of the proton's momentum, which was observed to not be carried completely by the quarks and antiquarks. The expected spin-1/2 nature of the quarks, proposed by Gell-Mann and Zweig, was confirmed by experimental tests of the Callan-Gross relation [24], which predicted that $F_2(x) = 2xF_1(x)$ if spin-1/2 quarks were indeed the constituents of the proton.

The quark-parton model was very successful in describing the high $Q^2$ region in DIS, however it requires the quarks within the proton to be weakly interacting over these short distance scales. This appeared to be in contradiction with the concept of strong quark interactions (*i.e.,* confinement) as quarks had not been observed previously in measurements which were sensitive to longer distance scales. The intense experimental and theoretical work surrounding the quark-parton model, and the evidence for partons in DIS at this time set the stage for the formulation of Quantum Chromodynamics (QCD) as the theory describing strong interactions. One of the crucial developments that would establish QCD as the leading theory to describe these interactions was the concept of asymptotic freedom [25, 26], which leads to weak quark interactions over short distance scales (large $Q^2$) as observed in DIS, and strong quark interactions (*i.e.,* confinement) over long distance scales (small $Q^2$) as seen in the observed mesons and baryons.

### 1.1.1 Parton Distribution Functions

The structure functions $F_1(x)$ and $F_2(x)$ discussed in the previous section, which characterize the DIS cross section, can be further decomposed into the individual quark contributions expressed as what are known as parton distribution functions (PDF). A parton distribution function, $q(x)$, is defined as the probability density of finding a parton with flavor $q$ in the proton carrying a momentum fraction $x$. The momentum fraction $x$ here is the Bjorken scaling variable, which in the infinite momentum frame can be thought of as the fraction of the proton's momentum carried by the parton. At large $Q^2$ DIS can be viewed as an incoherent sum of elastic scattering from the point-like constituents of the proton. Therefore, the structure functions must contain some basic information about the probability "finding" a quark of particular flavor with a given momentum fraction, which is represented by the PDFs. The structure functions, written in terms of the quark PDFs, are given by

$$F_2(x) = 2xF_1(x) = \sum_i e_i^2 \; xq_i(x), \tag{1.2}$$

where the sum on $i$ is over the quark flavors, and $e_i$ is the electric charge of that flavor quark. While the structure functions in DIS are not directly sensitive to the gluon distributions, there is additionally a gluon PDF, denoted by $g(x)$. Because each quark or gluon in the proton carries some fraction of the proton's momentum, it is clear that the sum of all the parton momentum fractions must be unity (*i.e.*, $\int dx \; xg(x) + \sum_i \int dx \; xq_i(x) = 1$). Measurements of the structure functions using DIS gave the first constraints on the parton distributions functions, and our first understanding of the momentum distribution of partons within the proton.

Parton distribution functions continue to play a critical role in much of nuclear and high-energy physics. They are essential in predictions of cross sections for processes with hadrons in the initial state at high energy, where perturbative QCD is expected to be valid. To see this, it is useful to introduce another fundamental principal of perturbative QCD, known

as factorization, which allows cross sections for processes involving hadrons to be factorized into two (or more) components. The short range, high $Q^2$ component from the partonic level scattering, such as the scattering of a virtual photon from the quasi-free quark in DIS can typically be computed in perturbative QCD. The long range, non-perturbative component of cross sections calculations is encoded in the parton distribution function which, as stated previously, gives the probability of finding a parton with a particular momentum fraction $x$. Therefore, at hadron colliders, such as the Tevatron, LHC, and RHIC, parton distribution functions are essential input to theoretical predictions for cross sections that can be compared with experimental measurements.

The PDFs also provide insight into the intrinsic properties and internal structure of the proton. Some aspects of proton structure, such as the helicity dependence of the PDFs, and their behaviors at large and small $x$, provide unique tests of non-perturbative QCD. The antiquark content of the proton is also very interesting since antiquarks are absent from the valence quark structure of the quark-parton model. This is discussed in more detail in Sec. 1.1.2.

Due to the inherently non-perturbative nature of the tightly bound partons within the proton bound state, the parton distribution functions cannot be calculated from first principles in perturbative QCD. Calculations in Lattice QCD can be applied to some of the non-perturbative effects of bound states in QCD, but cannot yet provide *ab initio* predictions for the PDFs (see Ref. [27] for a recent review). Therefore, for the foreseeable future, the distribution functions must be extracted from experimental data.

The process of extracting the parton distribution functions of the proton requires a large amount of data from many experiments, and incorporates them into a "global analysis" framework which determines the $x$-dependence of each flavor quark's PDF and the gluon PDF. A more detailed description of this global analysis procedure is discussed in recent PDF extractions by the MSTW [1] and CTEQ [28] groups. The general concept is to start with a reasonable functional form for the expected $x$ dependence of the individual PDFs,

with some adjustable parameters. The experimental data is then compared to perturbative QCD calculations which use the previously established functional form of the PDFs as input. From this one can produce a "global fit" of these input PDFs to the world's data. The extracted PDFs from the MSTW 2008 set, resulting from the optimized values of the fit parameters for the gluons, quarks and antiquarks, are shown in Fig. 1.2. The valence structure of the proton is evident in the rise of the $u$ and $d$ quark PDFs at large $x$, as the valence quarks tend to carry a large fraction of the proton momentum. Conversely, the sea quarks typically carry a very small fraction of the proton's momentum and therefore are found predominantly at low $x$. The heavier $s$, $c$, and $b$ quarks are suppressed with respect to the $u$ and $d$ quarks in the sea due to their larger mass.

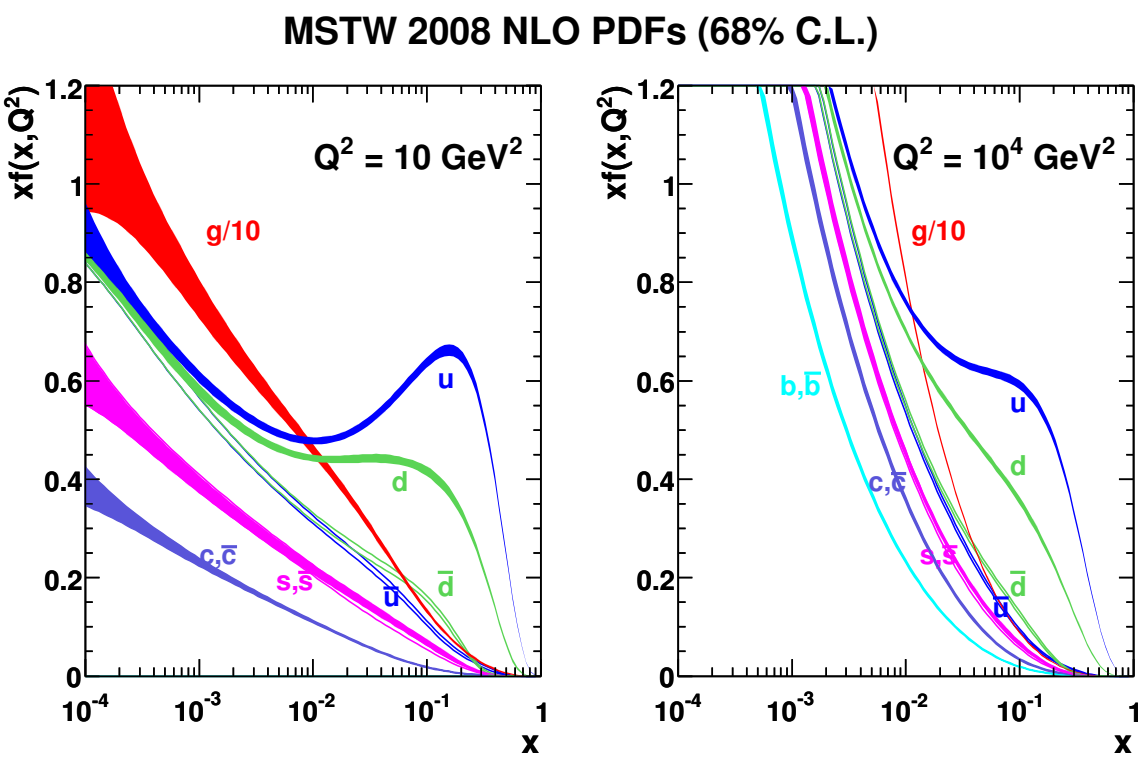


Figure 1.2: Parton distribution functions from the MSTW 2008 [1] set evaluated at $Q^2 = 10$ GeV$^2$ and $10^4$ GeV$^2$.

The data included in the global analyses vary slightly among the groups performing the fits, but in general they use a similar set of processes and measurements, which typically

fall into four categories: 1) fixed target DIS data; 2) fixed target Drell-Yan data; 3) collider DIS data from HERA; and 4) Tevatron data. The first category of fixed target experiments includes charged lepton DIS measurements of the $F_2$ structure function, which is a sum of PDFs, and neutrino-induced DIS using the charged current component of the weak interaction to isolate specific quark flavors. In these processes, the isospin (charge) symmetry of QCD allows one to probe different combinations of the valence quark PDFs by using both proton and neutron targets in DIS.

The fixed target Drell-Yan (lepton pair production) measurements provide unique constraints on the antiquark sea distributions and will be discussed more in Sec. 1.1.2. The HERA measurements of both neutral and charged current electroweak processes provide constraints on the PDFs, though at lower $x$ (due to the higher center-of-mass energies). Higher $\sqrt{s}$ also opens up new channels to study in Semi-Inclusive DIS (SIDIS), such as charm meson and jet production. Finally, the Tevatron $p\bar{p}$ data provide constraints on $u$ and $d$ quark and antiquark distributions through $W$ and $Z/\gamma^*$ production, as well as the most direct constraint on the gluon distributions through inclusive jet cross section measurements.

It is important to note that the data included in the global fits probe a wide variety of partonic sub-processes over a large range of $x$ and $Q^2$. As emphasized earlier, the fact that factorization in perturbative QCD is valid, and the soft (non-perturbative) and hard (perturbative) pieces of the interaction can be separated, means that the PDFs are universal ,*i.e.,* not dependent on the partonic process in the interaction. Because the $Q^2$ of the processes ranges from small values, on the order of a few GeV, to large values of $M_Z^2$, it is also necessary to understand the QCD renormalization group-induced evolution of the PDFs with $Q^2$, which is provided by the DGLAP [29, 30, 31] evolution equations.

### 1.1.2 Sea Quark Flavor Asymmetry

In the early quark-parton models the existence of a "sea" of quark-antiquark pairs was needed in order to reproduce the observed increase in the structure function strength at low $x$. In a simple perturbative QCD picture, the sea quarks are produced in the splitting of gluons to form quark-antiquark pairs. This would result in roughly equal numbers of $u\bar{u}$ and $d\bar{d}$ pairs, while heavier flavors such as strange quarks would be suppressed, as more energy is needed to produce them due to their larger mass. Experimentally, the strange sea quark contribution was indeed found to be rather small compared to the up and down sea quarks when studied in neutrino-induced charm production [32].

This perturbative picture of sea quarks being produced solely by gluon splitting assumes that the flavor content of the proton sea does not depend on the valence structure of the proton, despite its known valence quark flavor asymmetry (*i.e.,* $|p\rangle = |uud\rangle$). From this assumption it follows that the proton and neutron should have identical sea quark content. One method of studying the flavor content of the sea quark distributions would thus be to compare the distributions in the neutron to those in the proton. This was first studied via the Gottfried Sum Rule [33] in the parton model, which is defined as

$$I_g = \int_0^1 dx \ \left[F_2^p(x) - F_2^n(x)\right]/x \ = \ \frac{1}{3} + \frac{2}{3}\int_0^1 dx \ \left[\bar{u}_p(x) - \bar{d}_p(x)\right] \tag{1.3}$$

where $F_2^p$ and $F_2^n$ are the structure functions measured in proton and neutron DIS, respectively, and $\bar{u}_p(x)$ and $\bar{d}_p(x)$ are the antiquark PDFs of the proton sea. Note that Eq. 1.3 relies on the assumption of isospin (charge) symmetry at the partonic level between the proton and neutron, which allows the PDFs of the neutron to be related to those of the proton so that the integral can be expressed in terms of only the proton PDFs.

For a flavor symmetric sea $I_g = 1/3$, however, first measurements of the Gottfried Integral, which used a deuterium target to study the neutron structure function were smaller than the expected value of 1/3, suggesting that the $\bar{u}$ and $\bar{d}$ distributions were indeed differ-

ent. A precision determination of the Gottfried Sum Rule was performed by the New Muon Collaboration (NMC) [34, 35], which yielded a result of $I_g = 0.235 \pm 0.036$, corresponding to an excess of $\bar{d}$ quarks in the sea relative to $\bar{u}$.

Following these developments in DIS, Ellis and Stirling [36] proposed an independent means of studying the flavor composition of the sea quarks using the Drell-Yan process on hydrogen and deuterium targets, which would be sensitive to the ratio of the $\bar{d}$ to $\bar{u}$ distributions. The first result from the NA51 [3] experiment measured di-muon pairs in $pp$ and $pd$ collisions, obtaining a value of $\bar{u}/\bar{d} = 0.51 \pm 0.04(\text{stat}) \pm 0.05(\text{syst})$ at $x = 0.18$. This independent confirmation of the asymmetry of the light antiquark sea was consistent with the previous Gottfried Sum Rule results.

Unlike the Gottfried Sum Rule in DIS, where the sensitivity to the sea quark distributions is integrated over any $x$ dependence, one of the key advantages of using Drell-Yan as a probe of the sea quark distributions is that the $x$ dependence of the flavor asymmetry can be measured directly. This $x$ dependence was first studied by the E866/NuSea collaboration [2] which measured the ratio of the Drell-Yan cross section for a deuterium target to that of a proton target. In the limit where the quark (antiquark) in the process is a constituent of the beam (target) proton, this ratio can be written as

$$\frac{\sigma_{DY}(p+d)}{2\sigma_{DY}(p+p)} \simeq \frac{1}{2}\left(1 + \frac{\bar{d}(x)}{\bar{u}(x)}\right). \tag{1.4}$$

The results from the E866/NuSea [2] and NA51 [3] experiments are shown in Fig. 1.3 as a function of $x$. The $\bar{d}(x)/\bar{u}(x)$ ratio distribution shows an approximately linear rise up to $x \sim 0.2$, and indicate a return to a symmetric sea at higher $x$.

Semi-inclusive DIS has also been utilized by the HERMES experiment to investigate the unpolarized sea quark distributions, by measuring charged pion yields using hydrogen and deuterium targets [37]. The results are again consistent with the measurements from inclusive DIS and Drell-Yan.

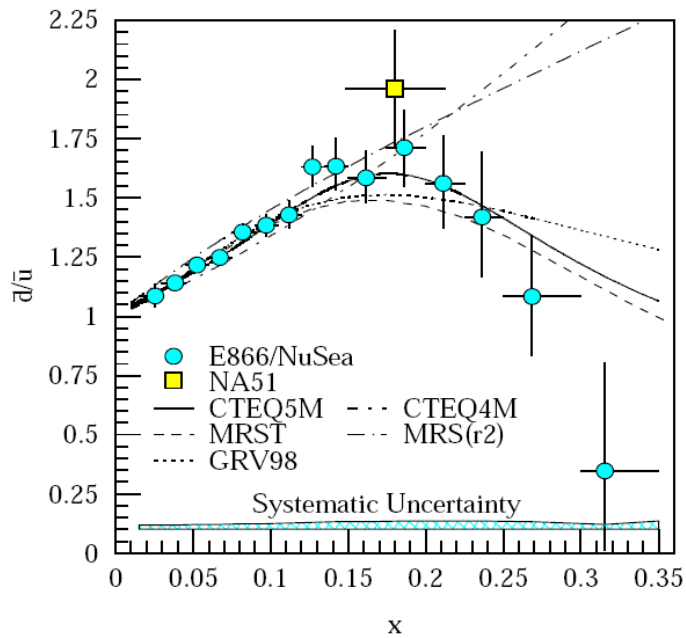


Figure 1.3: The $\bar{d}(x)/\bar{u}(x)$ ratio measured by the E866/NuSea [2] and NA51 [3] collaborations. The curves are parametrizations from a variety parton distributions function sets, see Ref. [4] for details.

Several theoretical models (reviewed in Ref. [4]) have been proposed to explain the observed excess of $\bar{d}$ over $\bar{u}$ quarks over a broad kinematic range. Field and Feynman [38] proposed that gluons splitting to $u\bar{u}$ pairs could be suppressed relative to $d\bar{d}$ by Pauli blocking due to the extra $u$ quark in the valence structure of the proton. Quantitative calculations [39, 40] later showed that the Pauli blocking effects are too small to explain the observed asymmetry due to the large phase space available to $q\bar{q}$ pairs. All of the current models suggest a non-perturbative mechanism is responsible for generating the observed flavor asymmetry of the light quark sea.

The theoretical models which qualitatively reproduce the features of the data can roughly be broken down into four general classes:

1. Meson cloud models [41], where the proton emits virtual pions and its wave function is a linear superposition of a bare proton, pion-nucleon, and pion-delta Fock states. The excess of $\bar{d}$ quarks in the proton is the result of a sizable contribution from the

neutron-$\pi^+$ state, due to the larger nucleon/delta mass difference.

2. Chiral quark models [42, 43], also employ virtual pions; however in this case they couple to the constituent quarks of the proton. Again, more virtual $\pi^+$ exist because the $u \to d\pi^+$ process is more common than $d \to u\pi^-$ due to the valence quark structure of the proton.

3. Instanton models [44], where a quark-instanton interaction flips the helicity of the incoming quark and produces a $q\bar{q}$ pair of a different flavor. Because there are more $u$ than $d$ quarks in the valence structure of the proton, more $d\bar{d}$ pairs are produced than $u\bar{u}$ pairs by the quark-instanton interaction.

4. Statistical models [45], in which the nucleon can be thought of as a gas of massless quarks and gluons in equilibrium. In this approach both $d\bar{d}$ and $u\bar{u}$ pairs are produced from gluon splitting with roughly equal probability, but because there are more $u$ quarks in the valence structure of the proton, the $\bar{u}$ quarks in the sea are more likely to annihilate with a valence quark, and thus an excess of $\bar{d}$ quarks is produced.

While each of the above models can reproduce the general trends of the $\bar{d}/\bar{u}$ data in Fig. 1.3 reasonably well, they tend to overshoot the data at high $x$. To further study the sea quark structure in this region a new experiment E906/SeaQuest [46] is currently in operation to further constrain the high $x$ region. In addition to these further studies of Drell-Yan processes, measurements of $W$ boson production in high energy $pp$ collisions provide an independent technique for investigating the flavor composition of the sea quarks. There are several key advantages to this approach, which are outlined in Sec. 1.2.

Thus far the proton sea quark flavor asymmetry has only been discussed in terms of unpolarized observables accessible in DIS and Drell-Yan. However, one interesting property of the models described above is that while the general trends of their predictions for the unpolarized $\bar{d}/\bar{u}$ ratio are rather similar, their predictions for some spin-dependent observables are quite different. Therefore, studying the spin-flavor structure of the antiquark sea

(discussed in Secs. 1.1.3 and 1.2) may provide new insights to aid in understanding the origin of the flavor asymmetry.

### 1.1.3 Helicity Structure of the Proton

To this point, discussion of the internal structure of the proton has been limited to unpolarized observables. The spin structure, of course, is another fundamental property of the proton which has received much attention in the last twenty years, and understanding this property remains one of the fundamental questions in strong interaction physics. The proton is a spin-1/2 fermion, and is known to be a bound state of quarks and gluons as discussed in Sec. 1.1. The quark-parton model assumed that, just as the electric charge of the proton is a simple sum of the electric charges of the valence quarks, the spin of the proton would simply be the vector sum of the intrinsic spins of the valence quarks. Since, the quark model was successful in reproducing the magnetic moments of baryons, this was thought to be a reasonable assumption.

The first hints of the spin structure of the proton were performed in DIS measurements using polarized beams and targets. Similar to the previously discussed structure functions $F_1$ and $F_2$ that characterize DIS using an unpolarized lepton beam and target, spin-dependent structure functions $g_1$ and $g_2$ can be measured using a longitudinally polarized lepton beam and a polarized target. In the parton model, the $g_1$ structure function is related to the difference in cross sections for DIS when the helicities of the beam and target are aligned and anti-aligned. $g_1$ is proportional to the spin asymmetry $A_1$, written as

$$A_1 \equiv \frac{\sigma^{++} - \sigma^{+-}}{\sigma^{++} + \sigma^{+-}} = \frac{g_1(x)}{F_1(x)} = \frac{\sum_i e_i^2(\Delta q_i(x) + \Delta\bar{q}_i(x))}{\sum_i e_i^2(q_i(x) + \bar{q}_i(x))}, \tag{1.5}$$

where $\sigma^{++}(\sigma^{+-})$ is the cross section for beam and target helicities aligned (anti-aligned), $q(x)$ is the unpolarized quark PDF, and $\Delta q(x)$ is the quark helicity distribution (or polarized PDF). The helicity distribution is defined as

$$\Delta q(x) \equiv q^+(x) - q^-(x), \tag{1.6}$$

where $q^+(x)$ is the PDF for quarks whose spins are aligned with that of the proton's, and $q^-(x)$ is the PDF for quarks with spin anti-aligned with the proton's spin. The helicity distribution is interpreted as the probability density of finding a quark of flavor $q$ with a proton momentum fraction $x$ and its spin preferentially polarized in the same direction as the proton.

The European Muon Collaboration (EMC) [47, 48] measured the spin structure function $g_1(x)$ in inclusive polarized DIS (pDIS) down to $x = 0.01$. The results did not agree with the theoretical predictions of the relativistic quark model proposed by Jaffe and Ellis [49]. The results from the EMC experiment indicated that the quarks carry only a small fraction ($\sim$20%) of the proton's spin, while the relativistic quark model expectation was a significantly larger value of $\sim$60%. This discovery that the quarks do not carry a large fraction of the proton spin is now referred to as the "proton spin crisis," and prompted much theoretical and experimental interest to further our understanding of the origin of the proton's spin.

Jaffe and Monahar [50] showed in 1990 that the proton spin can be rigorously decomposed into contributions from intrinsic quark and gluon polarization, as well as orbital angular momentum contributions. This spin sum rule can be written as

$$\langle S_p \rangle = \frac{1}{2} = \frac{1}{2}\Delta\Sigma + L_q + \Delta G + L_g, \tag{1.7}$$

where

$$\Delta\Sigma \equiv \int dx \ \big(\Delta u(x) + \Delta\bar{u}(x) + \Delta d(x) + \Delta\bar{d}(x) + \Delta s(x) + \Delta\bar{s}(x)\big) \tag{1.8}$$

is the total contribution from the quark and antiquark intrinsic spins (neglecting heavier flavors), $\Delta G = \int dx \ \Delta g(x)$ is the contribution from the gluon intrinsic spin, and $L_q$ and $L_g$ represent the quark and gluon orbital angular momentum contributions, respectively. Inclusive polarized DIS provides strong constraints on $\Delta\Sigma$, however only indirect constraints can be placed on the gluon spin contribution. Therefore, a high-energy polarized $pp$ program was developed at the Relativistic Heavy Ion Collider to directly probe the gluon spin dis-

tributions of the proton [7]. It should also be noted that an alternative sum rule, proposed by Ji [51], decomposes the contributions to the proton spin in a slightly different manner. However, the comparison of these two sum rules is not particularly relevant to this thesis and will therefore not be discussed further here.

While inclusive DIS measurements place the most stringent constraints on the total quark spin contribution, $\Delta\Sigma$, they are only sensitive to the square of the charge of the struck parton and thus cannot separate the quark spin contributions by flavor, or distinguish between quarks and antiquarks. New techniques are therefore required to probe these individual quark and antiquark distributions. One method for studying the individual quark and antiquark helicity distributions is through polarized semi-inclusive DIS. This technique is similar to the studies of the unpolarized antiquark distributions described in the previous section, where charged hadrons are reconstructed in the final state along with the scattered electron, and fragmentation functions allow one to correlate the reconstructed hadron yield with the original parton probed in the hard scattering.

Using both polarized proton and deuterium (neutron) targets allows for the extraction of each of the light quark and anti-quark helicity distributions independently. However, this method is limited by uncertainties in the fragmentation process. Measurements from the Spin Muon Collaboration [52] and the HERMES collaboration [53], that use this method have been included in a recent global analysis [5] of inclusive and semi-inclusive DIS measurements, as well as polarized $pp$ spin asymmetry measurements at RHIC that are sensitive to the gluon helicity distribution. While the helicity distributions for the quarks are fairly well constrained, the anti-quarks have much larger uncertainties. The results for the difference of the $\bar{u}$ and $\bar{d}$ quark helicity distributions are shown in Fig. 1.4.

Recent results from the COMPASS collaboration [6], which have yet to be included in a global fit, are presented in Fig. 1.5. Also shown in Fig. 1.5 are predictions from various non-perturbative models (outlined in Sec. 1.1.2) which illustrates the unique sensitivity of the antiquark helicity distributions in differentiating among models which all reproduce the

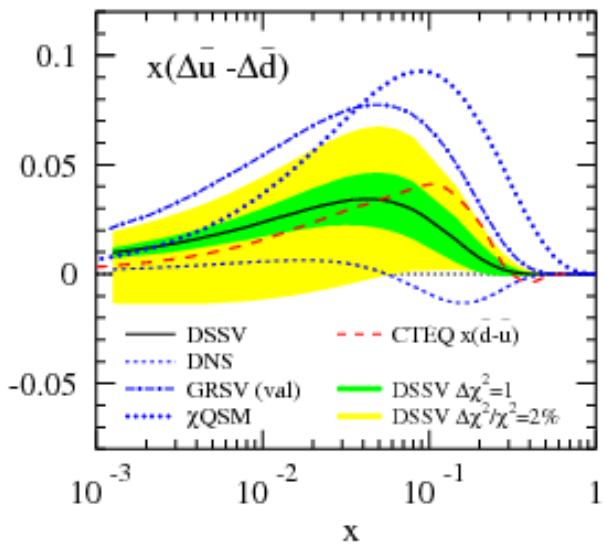


Figure 1.4: The difference between the $\bar{u}$ and $\bar{d}$ helicity distribution at $Q^2 = 10$ GeV$^2$ from the DSSV global analysis [5]. The green (yellow) bands represent the $\Delta\chi^2 = 1$ ($\Delta\chi^2/\chi^2 = 2\%$) uncertainties of the global fit.

unpolarized $\bar{d}/\bar{u}$ flavor asymmetry reasonably well. The meson cloud model (Kumano and Miyama [54]), for example, predicts a small negative value for $x\left(\Delta\bar{u} - \Delta\bar{d}\right)$, while the statistical model (Bourrely, Soffer and Buccella [45]) and chiral quark model (Wakamatsu [55]) predict a large positive value. The data are not yet sufficiently precise to allow one to differentiate among the models.

The production of $W^{\pm}$ bosons in polarized $pp$ collisions is an independent method of probing the spin structure of the light quarks and antiquarks. Unlike polarized SIDIS, $W^{\pm}$ production provides direct sensitivity to the $u$ and $d$ quark and antiquark helicity distributions through the $V - A$ structure of the weak interaction coupling, at much higher $Q^2$, and without the use of fragmentation functions. In the next section we outline some details of the production of $W^{\pm}$ bosons in polarized $pp$ collisions. and discuss the spin asymmetry observable $A_L$ which, at leading order, is directly related to the antiquark helicity distributions of interest.

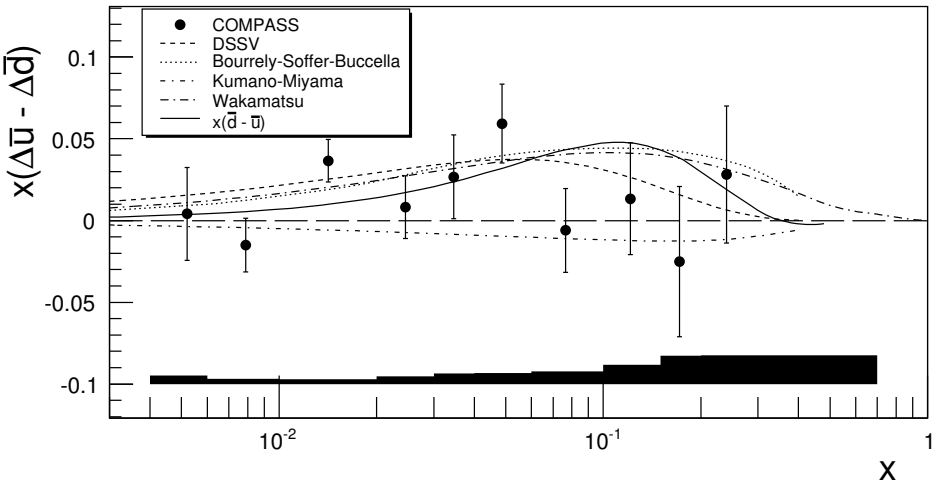


Figure 1.5: The difference between the $\bar{u}$ and $\bar{d}$ quark helicity distributions extracted from SIDIS data at the COMPASS experiment [6]. The model curves are explained further in the text.

## 1.2 $W$ Boson Production in Polarized Proton-Proton Collisions

At leading order in the Standard Model, $W$ bosons are produced in $pp$ collisions by the annihilation of a quark from one proton with an antiquark in the other. A diagram for the process is shown in Fig. 1.6 [7], where $\bar{d} + u \rightarrow W^+$ (the analogous diagram for $\bar{u} + d \rightarrow W^-$ is not shown). There are also small contributions from strange quarks due to quark flavor mixing, but those will be neglected for the purpose of this discussion. This section will focus on the production of $W^\pm$ bosons, which decay via the $W \rightarrow e\nu$ decay channel with a branching ratio of ∼11%. Although the $W \rightarrow e\nu$ decay channel has a smaller branching ratio than the hadronic decay mode, the leptonic decay mode is experimentally much easier to identify than the $W \rightarrow$ jets channel, which is more difficult to separate from the QCD di-jet continuum.

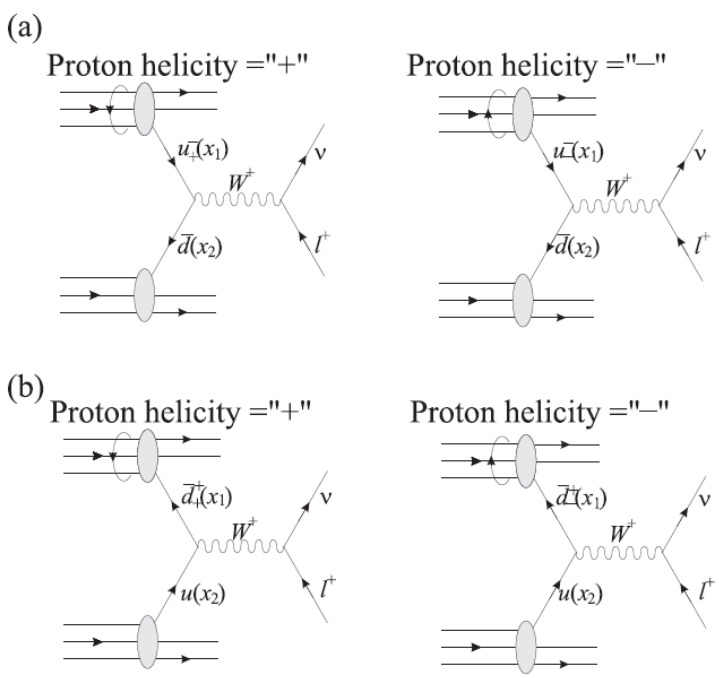


Figure 1.6: Feynman diagrams for $W^+$ boson production in polarized $pp$ collisions [7]. In (a) the polarized proton provides the $u$ quark, while in (b) the $\bar{d}$ quark is a constituent of the polarized proton. The helicity of the proton (quark) is indicated by the subscript (superscript) on the quark coming from the polarized proton.

Due to the $V - A$ structure of the weak interaction in the Standard Model, $W$ bosons only couple to left-handed quarks and right-handed antiquarks. In other words, the maximal violation of parity in $W$ boson production requires that the helicities of the incoming quark and antiquark in the $pp$ collision are fixed. This helicity structure can be seen in the differential cross sections for $W^+$ and $W^-$ production [9]

$$\frac{d\sigma_{W^+}}{d\cos\theta} \propto \bar{d}(x_1)u(x_2)(1+\cos\theta)^2 + u(x_1)\bar{d}(x_2)(1-\cos\theta)^2 \tag{1.9}$$

$$\frac{d\sigma_{W^-}}{d\cos\theta} \propto \bar{u}(x_1)d(x_2)(1-\cos\theta)^2 + d(x_1)\bar{u}(x_2)(1+\cos\theta)^2, \tag{1.10}$$

where $\theta$ is the decay $e^\pm$ scattering angle in the $W$ center-of-mass system, and $u(x), d(x), \bar{u}(x), \bar{d}(x)$ are the up and down quark and antiquark unpolarized PDFs. This $\cos\theta$ dependence of the decay lepton yield is illustrated graphically in Fig. 1.7 [8], where the $W$s tend to be boosted in the direction that the incoming valence quark (higher $x$) was traveling. The helicity structure of the interaction causes the charged lepton to be preferentially emitted parallel (anti-parallel) to the $W^-$ ($W^+$) direction due to the handedness of the neutrino produced in the final state.

Figure 1.7: Diagrams illustrating the helicity configurations of $W^-$ (left) and $W^+$ (right) production [8]. The single arrows ($\rightarrow$) indicate the particle direction of motion, while the double arrows ($\Rightarrow$) indicate the spin direction. The incoming quark and antiquark with fixed helicity are shown above the $z$ axis, while the outgoing $e^\pm$ and neutrino are shown below it.

As discussed in Sec. 1.1.3, $W^\pm$ boson production in polarized $pp$ collisions provides a new means of studying the light quark and antiquark helicity distributions. The observable of

interest is the parity-violating, longitudinal single-spin asymmetry defined as

$$A_L = \frac{\sigma^+ - \sigma^-}{\sigma^+ + \sigma^-}, \tag{1.11}$$

where $\sigma^{+(-)}$ is the cross section for producing a $W$ when the helicity of the longitudinally polarized proton beam is positive (negative). In order to understand how this asymmetry is related to the unpolarized and polarized parton distributions, it is useful to work through the simple example illustrated in Fig. 1.6. In the production of the $W^+$ boson, the $u$ ($\bar{d}$) quark is required to have negative (positive) helicity, as indicated by the superscripts in the diagrams. Therefore, if the polarized proton provides the $u$ quark for the interaction, then the difference between the left and right diagrams of Fig. 1.6 (a) yields a single spin asymmetry of

$$A_L^{W^+} = \frac{u_+^-(x_1)\bar{d}(x_2) - u_-^-(x_1)\bar{d}(x_2)}{u_-^-(x_1)\bar{d}(x_2) + u_-^-(x_1)\bar{d}(x_2)} = -\frac{\Delta u(x_1)}{u(x_1)}, \tag{1.12}$$

where the helicity of the proton (quark) is indicated by the subscript (superscript) on the $u$ quark coming from the polarized proton similar to Fig. 1.6 (a). One can see that the quantity on the right of Eq. 1.12 is exactly the definition of the polarized parton distribution in Eq. 1.6. For the case where the polarized proton in the interaction provides the antiquark, seen in the Fig. 1.6 (b), an analogous expression can be written as

$$A_L^{W^+} = \frac{\bar{d}_+^+(x_1)u(x_2) - \bar{d}_-^+(x_1)u(x_2)}{\bar{d}_+^+(x_1)u(x_2) + \bar{d}_-^+(x_1)u(x_2)} = \frac{\Delta\bar{d}(x_1)}{\bar{d}(x_1)}. \tag{1.13}$$

Experimentally however, one does not know whether the quark or antiquark was a constituent of the polarized proton, the general expression for the measured asymmetry is a superposition of Fig. 1.6 (a) and (b), given by

$$A_L^{W^+} = \frac{\Delta\bar{d}(x_1)u(x_2) - \Delta u(x_1)\bar{d}(x_2)}{\bar{d}(x_1)u(x_2) + u(x_1)\bar{d}(x_2)}. \tag{1.14}$$

The analogous expression for $A_L^{W^-}$ is obtained by switching $u$ and $d$ in Eq. 1.14.

Although the measured asymmetry $A_L^W$ will depend on the helicity distributions of both the quark and antiquark, the relative contribution of each will vary with the decay kinematics. To see this, note that the Bjorken-$x$ values of the incoming quark and antiquark are given by the simple kinematic relations

$$\sqrt{x_1 x_2} = \frac{M_W}{\sqrt{s}} \quad \text{and} \quad p_{L,W} = \frac{\sqrt{s}}{2}\left(x_1 - x_2\right), \tag{1.15}$$

where $M_W$ is the mass of the $W$ boson, $\sqrt{s}$ is the center-of-mass energy of the colliding protons, and $p_{L,W}$ is the $W$ longitudinal momentum along the $z$-axis. At the center-of-mass energies accessible at RHIC, the quark is very likely to come from the valence region, and carry a significantly larger momentum fraction of its parent proton than the antiquark. Therefore, if $p_{L,W}$ is reconstructed, one can preferentially select events where the polarized proton provided the quark or antiquark in the interaction using the direction of the $W$ boost. One can increase sensitivity to the quark or antiquark helicity distributions separately by selecting asymmetric collisions (*i.e.,* large $p_{L,W}$), where the higher (lower) $x$ parton in the collision is very likely the quark (antiquark). Because only the charged lepton is reconstructed in the final state, the $W$ four momentum cannot be measured directly. However, the decay $e^{\pm}$ kinematics are well measured, and can be related to the $W$ boost direction.

The $e^{\pm}$ decay kinematics in the lab frame are related to the $W$ boost by

$$p_{L,e}^{lab} = \frac{1}{\gamma} p_{L,e}^{*} + \beta E_e^{lab}, \tag{1.16}$$

where the lab-frame $e^{\pm}$ longitudinal momentum ($p_{L,e}^{lab}$) and energy ($E_e^{lab}$) are well measured, and the $e^{\pm}$ longitudinal momentum in the $W$ rest frame is given by $p_{L,e}^{*} = \cos\theta \cdot M_W/2$. Only the magnitude of $\cos\theta$ can be determined from the reconstructed $e^{\pm}$ transverse momentum ($p_T^e = \sin\theta \cdot M_W/2$), which gives two possible solutions for the $W$ boost direction for a given electron four-momentum in the lab frame. Some simplification is possible for large $p_{L,e}^{lab}$, where $|y_e^{lab}|$ is large, and the correct solution can be statistically chosen, increasing

sensitivity to the antiquark or quark distributions separately as illustrated in Fig. 1.8 and the discussion below.

The strategy that we have adopted is to measure the longitudinal single-spin asymmetry as a function of the decay $e^{\pm}$ pseudorapidity, $\eta_e$. A theoretical framework [9, 56] has been developed to describe these asymmetries in terms of inclusive charged lepton production, which accounts for the $W$ decay width and the transverse momentum, $q_T$, of the $W$ neglected in relating the $W$ and $e^{\pm}$ rapidities above, where a collinear geometry was assumed. Figure 1.8 shows predictions for the single-spin asymmetry $A_L$ for $W^+$ and $W^-$ using a variety of helicity distribution sets outlined in Ref. [9]. The spread in the predictions gives a qualitative feel for the uncertainty in the theoretical predictions, due largely to the uncertainties in the helicity distributions. Because the antiquark helicity distributions are much more poorly known than those for the quarks, the larger dispersion in the curves appears in regions of $\eta_e$ that are most sensitive to the antiquark polarizations. One can see from Fig. 1.8 that $A_L^{W^-}$ is most sensitive to $\Delta\bar{u}$ at large negative $\eta_e$, and $A_L^{W^+}$ is most sensitive to $\Delta\bar{d}$ at large positive $\eta_e$.

While studies of $W$ production in polarized $pp$ collisions are a unique capability of the RHIC accelerator complex, the production of $W$ and $Z/\gamma^*$ bosons in unpolarized hadronic interactions have long been used to test the Standard Model of particle physics and to further our understanding of unpolarized proton structure. First observations of $W$ production were made by the UA1 [57, 58] and UA2 [59, 60] collaborations in proton-antiproton collisions at $\sqrt{s} = 630$ GeV at the CERN Sp$\bar{p}$S facility. This was followed by extensive studies by the CDF [61, 62] and D0 [63, 64] collaborations, using $p\bar{p}$ collisions at the Fermilab Tevatron at $\sqrt{s} = 1.8$ and 1.96 TeV, where precise measurements of the $W$ production cross sections and mass [65, 66] were obtained. Only in recent years have there been $pp$ collisions at sufficiently high center-of-mass energies for comparable studies at $\sqrt{s} = 500$ GeV by the STAR [67, 68] and PHENIX [69] collaborations at RHIC, and recently by the LHC experiments ATLAS [70] and CMS [71, 72] at $\sqrt{s} = 7$ TeV.

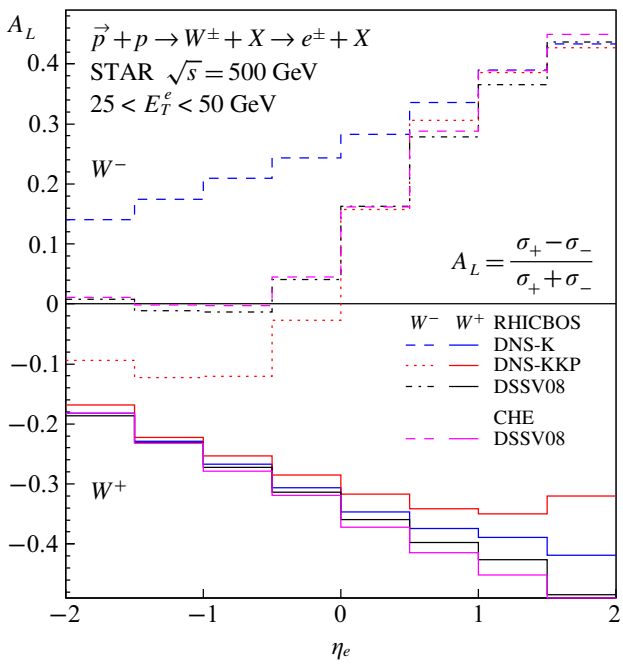


Figure 1.8: Predictions for the longitudinal single-spin asymmetry $A_L$ for $W^{\pm}$ production at $\sqrt{s}$ = 500 GeV, as a function of the decay $e^{\pm}$ pseudorapidity. The curves from different helicity distributions are discussed in Ref. [9].

The new generation of high-energy $pp$ collider data also provides an alternate technique for studying the unpolarized sea quark $\bar{d}/\bar{u}$ flavor asymmetry, as discussed in Sec. 1.1.2. In $p\bar{p}$ collisions, the production of $W$s mostly probes the valence quark (antiquark) distributions of the proton (antiproton), such that the cross sections for $W^+$ and $W^-$ production are approximately the same. In $pp$ collisions, at RHIC energies, the cross sections probe primarily the valence structure of the quarks and the sea structure of the antiquarks. This results in different cross sections for $W^+$ and $W^-$ due to the $uud$ valence structure of the proton, as well as the $\bar{d}/\bar{u}$ asymmetry in the sea structure. The ratio of the $W^+$ to $W^-$ cross section, $R_W = \sigma_{W^+}/\sigma_{W^-}$, is the observable of interest for the $\bar{d}/\bar{u}$ flavor asymmetry, as it can be expressed purely in terms of the up and down quark and antiquark distributions (when small contributions from strange quarks are neglected) [73]

$$R_W = \frac{\sigma_{W^+}}{\sigma_{W^-}} = \frac{u(x_1)\bar{d}(x_2) + \bar{d}(x_1)u(x_2)}{\bar{u}(x_1)d(x_2) + d(x_1)\bar{u}(x_2)}. \tag{1.17}$$

In the Bjorken-$x$ range probed at RHIC, $0.1 \lesssim x \lesssim 0.3$, measurements of the $W^+/W^-$ cross section ratio can provide independent constraints on the same $\bar{d}/\bar{u}$ flavor asymmetry proved in the Drell-Yan measurements discussed in Sec. 1.1.2.

Previous measurements of $\bar{d}/\bar{u}$ using hydrogen and deuterium targets to compare the proton and neutron sea quark distributions, required the assumption of charge symmetry in order to relate the $p/n$ sea asymmetries to the $\bar{d}/\bar{u}$ asymmetry of the *proton* sea. The assumption of charge symmetry is not required in the $W$ cross section ratio method since only the sea quarks of the proton are being probed. The $W$ cross section ratio has the additional advantage of being sensitive to the $\bar{d}/\bar{u}$ asymmetry at $Q^2 = M_W^2$, which is well above the $Q^2$ probed by Drell-Yan and the Gottfried Sum Rule measurements. It should be pointed out that measurements of the lepton charge asymmetry at the LHC [74, 75] also provide constraints on the light quark and antiquark distributions, in an $x$ range lower than that probed at RHIC, due to the much higher energy collisions.

## 1.3 Structure of This Thesis

In the previous sections of this introduction, the status of our current knowledge of the internal structure of the nucleon, through measurements of the PDFs, has been described. Studies of the unpolarized antiquark flavor asymmetry and antiquark helicity distributions provide new insight into the origin of the light sea quarks within the proton and the advantages of utilizing $W^{\pm}$ boson production in polarized $pp$ collisions to further constrain these antiquark distributions have been demonstrated. This thesis describes the first measurement of the $W^{\pm}$ parity-violating single-spin asymmetries and the production cross sections for $W^{\pm}$ and $Z/\gamma^*$ bosons at $\sqrt{s} = 500$ GeV by the STAR collaboration at RHIC, and the first measurement of the $W^+/W^-$ cross section ratio at $\sqrt{s} = 500$ GeV. The results are based on 13.2 pb$^{-1}$ of data collected in 2009 and have been described in two STAR collaboration publications [67, 68].

The organization of this thesis is as follows. Chapter 2 provides a brief overview of the RHIC accelerator complex and the STAR detector focusing on the subsystems relevant to this analysis. In Ch. 3 we describe the data recorded in 2009 (including the measurement of the integrated luminosity) along with a brief description of the simulation samples that were generated for this work. The reconstruction algorithms used to extract the $W$ and $Z/\gamma^*$ signal and reduce the dominant QCD background, are summarized in Ch. 4, while Ch. 5 describes the procedure used to estimate the background contamination of the $W$ and $Z/\gamma^*$ signal yields. Finally, the calculation of the cross sections and spin asymmetries are discussed in Ch. 6 and 7, respectively, and the results are compared to theoretical predictions. Ch. 8 provides a brief summary of the main results and conclusions drawn from this work.

# Chapter 2

# Experimental Setup

## 2.1 Polarized Protons at RHIC

The Relativistic Heavy Ion Collider (RHIC) at Brookhaven National Laboratory (BNL) is the the world's only polarized proton collider, capable of producing $\vec{p}\vec{p}$ collisions with center of mass energies up to $\sqrt{s} = 500$ GeV. Furthermore, RHIC is a very versatile accelerator, with the capability to also collide a variety of heavy ion species at varying energies from $\sqrt{s_{NN}} = 7.7$ GeV up to 200 GeV. A diagram of the RHIC accelerator complex layout is shown in Fig. 2.1, emphasizing the components critical to its operation as a polarized proton accelerator, which will be described briefly in this section. A full overview of the capabilities of RHIC as a polarized proton collider is available in Ref. [76].

### 2.1.1 Accelerator Complex

The RHIC accelerator chain starts with an optically-pumped polarized $H^-$ ion source (OPPIS) [77], which was constructed from the OPPIS source previously used at KEK. Polarized $H^-$ ions are produced in a 400 $\mu$s pulse with a current of 0.5-1 mA, yielding $\sim 9\times10^{11}$ $H^-$ ions in each pulse with 80-85% polarization. The pulse of $H^-$ ions leaves the source with an energy of 35 keV, and is then accelerated to 200 MeV with a radio-frequency quadrupole and a 200 MeV LINAC. This process is $\sim$ 60% efficient and results in the 400 $\mu$s pulse of $H^-$ ions being strip-injected into the Booster as a single bunch of $\sim 4\times10^{11}$ polarized protons. The bunch is then accelerated to 2.4 GeV in the Booster and transferred to the Alternating Gradient Synchrotron (AGS), where it is further accelerated to $\sim$ 25 GeV before injection into RHIC. Here the beams are accelerated to and stored at the desired energy; in the case of this work, $E_{beam}$ 250 GeV.

Each time the RHIC rings (known as "blue" and "yellow") are injected with proton bunches from the AGS, is denoted as the start of a new "fill." A "fill" lasts from the time of ring injection and ramping until the beams are dumped after the collision rate goes below some nominal threshold. The RHIC rings can accommodate 120 proton bunches (limited by the number of RF buckets and the required spacing between bunches), however only $\sim$109 of them are filled in each ring. The $\sim$11 missing bunches in each ring (known as the abort gaps) are required to safely dump the beams at the end of the fill.

#### Spin Dynamics and Siberian Snakes

One of the major challenges of a high-energy polarized proton-proton collider is to maintain the beam polarization through acceleration to the high energies at which the beams are stored. Therefore, it is useful to first give a brief overview of the spin dynamics of a polarized particle in a synchrotron to better understand the tools used at RHIC to maintain high beam polarization at high energies.

The Lorentz force equation of motion for a particle in a synchrotron with an external

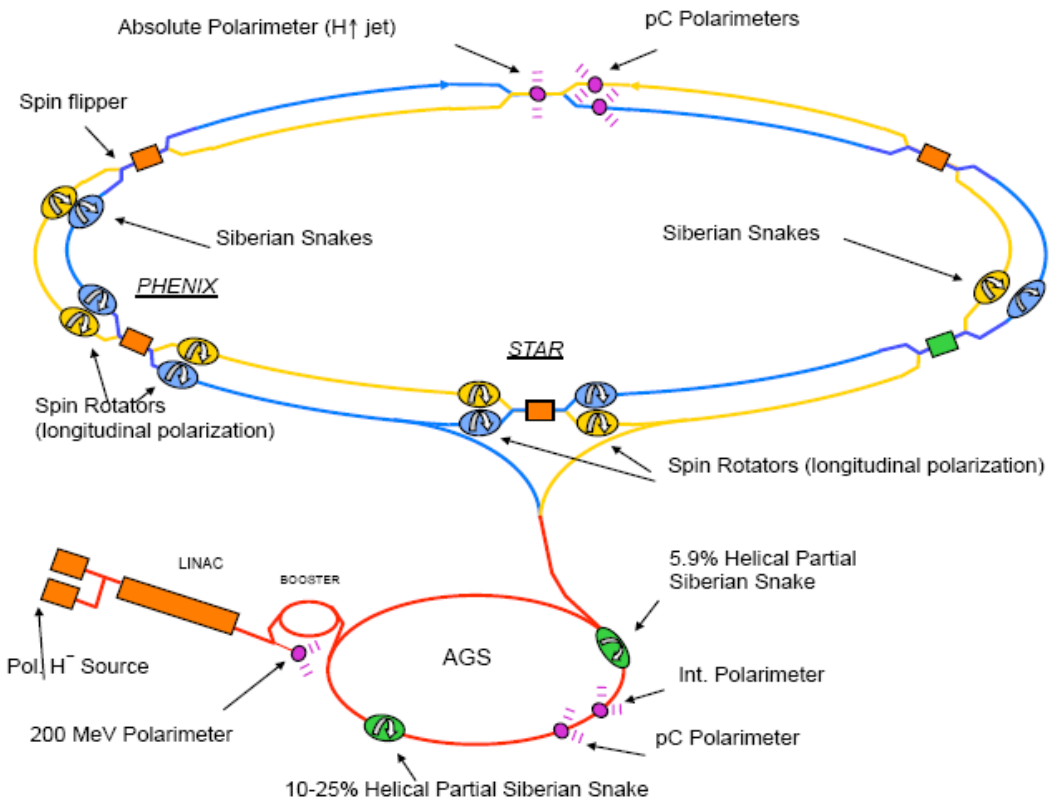


Figure 2.1: Diagram of the Relativistic Heavy Ion Collider complex.

magnetic field is given by

$$\frac{d\vec{v}}{dt} = \frac{e}{\gamma m}\vec{v} \times \vec{B}_{\perp}, \tag{2.1}$$

where $\gamma = E/m$ is the Lorentz factor, $\vec{B}_{\perp}$ is the guiding magnetic field perpendicular to the direction of motion, and $e$ ($m$) is the particle's charge (mass). A similar expression for the precession of a particle's spin vector in an external magnetic field is described by the Thomas-BMT equation [78][79]

$$\frac{d\vec{S}}{dt} = \frac{e}{\gamma m}\vec{S} \times \left(G\gamma\vec{B}_{\perp} + (1+G)\vec{B}_{\parallel}\right), \tag{2.2}$$

where $\vec{S}$ is the spin vector in the particle's rest frame, $G$ is the anomalous magnetic moment ($G$=1.7928 for the proton), and $\vec{B}_{\perp(\parallel)}$ is the magnetic field perpendicular (parallel) to the direction of motion. In the ideal case of a circular synchrotron with only a vertical guiding magnetic field perpendicular to the particle's motion, the $\vec{B}_{\parallel}$ term in Eq. 2.2 disappears. Therefore, comparing Eqs. 2.2 and 2.1 one finds that they differ only by a factor $G\gamma$. This factor, known as the spin tune ($\nu_{sp} \equiv G\gamma$), indicates the number of full spin precessions the particle makes in the synchrotron in each orbital revolution.

In a real synchrotron, however, the accelerating beams encounter horizontal magnetic fields, which can induce depolarizing resonances. These horizontal fields produce small perturbations of the vertical spin vector from its regular precession. The perturbations tend to average out as long as they occur at different points in the spin vector's precession for each revolution. However, if the frequency of these perturbations is equal to the spin precession frequency, the perturbing effects add coherently and a depolarizing resonance occurs, causing polarization loss.

There are two main types of depolarizing resonances: imperfection resonances and intrinsic resonances. Imperfection resonances are due to magnet errors or mis-alignments, and have resonances at integer values of $G\gamma$. Intrinsic resonances, however, are produced by the focusing magnets and create resonances at frequencies $G\gamma = kP \pm \nu_y$, where $P$ is the super-

periodicity, and $\nu_y$ is the vertical betatron tune. To reduce the effects of these depolarizing resonances, a new technique using "Siberian Snakes" [80] has been developed for RHIC.

A snake consists of a series of helical dipole magnets which adiabatically rotates the spin vector by 180° about a horizontal axis each time the beam passes through. There are two snakes on opposite sides of both RHIC rings, which produce rotations about two perpendicular horizontal axes without disturbing the stable spin vector direction. This is equivalent to a 180° precession of the spin vector around the vertical axis during each revolution. The depolarizing resonances are thereby effectively canceled out while maintaining a stable vertical polarization vector. Alternatively, one could describe the effects of the two snakes as fixing the spin tune to be a half-integer independent of energy which, assuming the betatron tune is not half-integer, ensures that the conditions necessary for depolarizing resonances as discussed here are never satisfied.

**Spin Rotators**

As stated previously, the stable polarization vector during acceleration and storage in RHIC is in the vertical direction, transverse to the proton's direction of motion. However, as described in Sec 1.1.3, the observable of greatest interest for $W$ production in polarized $pp$ collisions is a longitudinal single-spin asymmetry, which requires that the beams be polarized in the longitudinal direction. To produce the desired longitudinal polarization of the two beams at the interaction regions, another set of helical dipole magnets called spin rotators [81] are used. There are four spin rotators for each interaction region, two for each beam. For each beam, one magnet rotates the spin vector 90° from transverse to longitudinal polarization before it enters the interaction region, and the second magnet rotates the spin vector back to transverse polarization after leaving the interaction region. Both the STAR and PHENIX interaction regions have spin rotators, so the two experiments can independently choose to have either longitudinally or transversely polarized collisions.

### 2.1.2 Polarimeters

The measurement of the beam polarizations is obviously a critical component of the RHIC spin physics program, both for feedback to the accelerator group about polarization performance and for spin asymmetry measurements at the experiments. There are two different polarimeters used in RHIC, the proton-carbon (pC) polarimeter [82, 10] and hydrogen gas jet (H-Jet) polarimeter [83, 84], which provide complementary information on the beam polarizations and are combined to yield a single polarization value for each beam for each RHIC fill.

The pC polarimeters utilize a thin carbon ribbon target which is moved across the beams to measure a left-right asymmetry (with respect to the polarization vector) in the elastic scattering of the beam protons from the carbon nuclei in the target. The protons are scattered at very forward angles, and so the carbon nuclei recoil approximately perpendicular to the beam direction. A diagram of the detector configuration with six individual silicon strip detectors located inside the beampipe is shown in Fig. 2.2. In 2009 there were two pC polarimeters in use for both beams, providing a useful cross check of the polarization measurements.

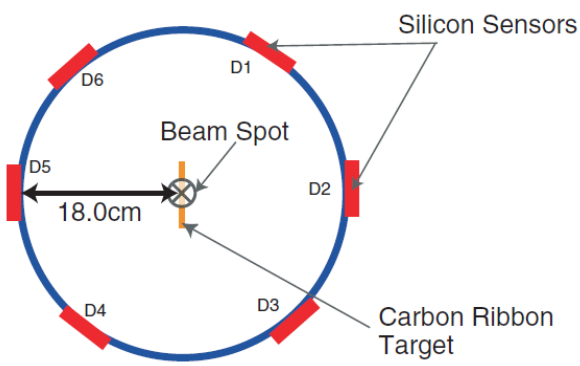


Figure 2.2: A cross section view of the pC polarimeter with six silicon detectors inside the beam pipe.

The left-right asymmetry in the p+C elastic scattering at the momentum transfers of interest is due mainly to the interference of electromagnetic and hadronic scattering ampli-

tudes in the so called Coulomb-Nuclear Interference (CNI) region (see [85] and references therein). One advantage of this process is that the cross section is large enough to give a high statistics measurement of the asymmetry in a short time period (< 1 minute), allowing for several measurements during each RHIC fill. The polarization measured by the pC polarimeters can be written as

$$P_{beam} = \frac{1}{A_N^{pC}} \frac{N_L - N_R}{N_L + N_R} = \frac{\epsilon_N}{A_N^{pC}}, \tag{2.3}$$

where $A_N^{pC}$ is the effective p+C analyzing power, $N_{L(R)}$ is the number of recoil carbons to the left(right) of the beam polarization direction, and $\epsilon_N$ is the raw left-right asymmetry. Unfortunately, the absolute analyzing power $A_N^{pC}$ is not well known at RHIC energies, and therefore the pC polarimeter is not used to provide an absolute polarization measurement.

Although the pC polarimeters do not provide an absolute polarization measurement, they do provide critical relative polarization measurements among different fills. Also, because they can be completed several times in a given fill, the pC measurements are used to track any polarization losses over the course of a fill. Finally, the pC measurements provide a measurement of the polarization profile, which is the polarization change across the beam's transverse dimension. This is done by scanning the carbon targets across the beam to measure the polarization at different points in the beam's transverse profile.

The relative polarizations measured by the pC polarimeters require a measurement of the absolute polarization for normalization. This is provided by the other polarimeter at RHIC, the H-Jet polarimeter. The H-jet polarimeter uses a jet of polarized hydrogen gas as the target, and the left-right asymmetry of the recoil protons from *pp* scattering in the the H-Jet target is again measured using an array of silicon strip detectors (see Fig. 2.3). Since for the H-Jet polarimeter both the beam and target are polarized protons, the analyzing

power, $A_N^{pp}$, is the same for both the target and beam protons, and can be expressed as

$$A_N^{pp} = \frac{\epsilon_N^{beam}}{P_{beam}} = \frac{\epsilon_N^{target}}{P_{target}}. \tag{2.4}$$

The absolute beam polarization, $P_{beam}$, can thus be expressed in terms of the target polarization, $P_{target}$, and the raw asymmetries measured for the beam and target. The target spin states are varied in time so the raw target asymmetry, $\epsilon_N^{target}$, can be measured by averaging over the spin states of the beam. Similarly, the beam asymmetry, $\epsilon_N^{beam}$, is measured by averaging over the spin states of the target. Finally, the polarization of the H-Jet target, $P_{target}$, is measured by a Breit-Rabi polarimeter with an absolute accuracy of better than 2%, which provides the last element needed to yield a measurement of the absolute beam polarization via

$$P_{beam} = \frac{\epsilon_N^{beam}}{\epsilon_N^{target}} P_{target}. \tag{2.5}$$

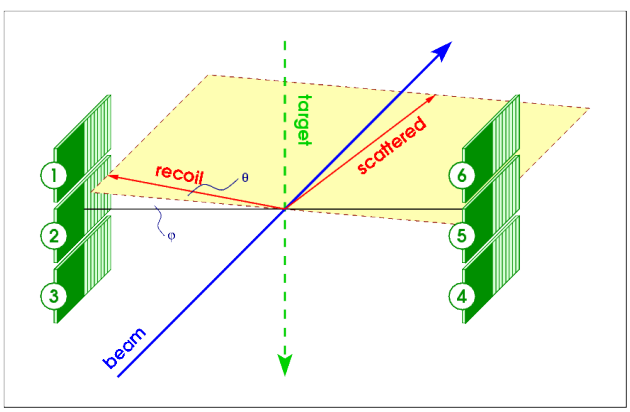


Figure 2.3: Diagram of H-Jet polarimeter.

The H-Jet polarimeter is an extremely powerful tool for measuring the absolute beam polarization. However, the cross section for this elastic $pp$ scattering process is rather small, with the result that the measurements must be integrated over a much longer time interval than the pC measurements. Using the ratio of the polarization measured by the pC and H-Jet polarimeters over all of the $\sqrt{s} = 500$ GeV data in 2009, an overall normalization was

obtained for each of the pC polarimeters, resulting in a polarization value for each beam for each fill, as reported in Ref. [10].

## 2.2 Solenoidal Tracker at RHIC (STAR)

Two general-purpose detectors, STAR [86] and PHENIX [87], were developed for the RHIC physics program. They are both large experiments with more than 500 collaborators each, and different aspects of the two detector designs were optimized to provide some unique capabilities and measurements, but also maintain some overlap as well. The measurement and analysis described in this thesis were performed using the STAR detector.

The STAR detector is a large acceptance collider detector consisting of many separate subsystems designed for specific purposes. A schematic of the STAR detector is shown in Fig. 2.4 with an embedded $W \to e\nu$ candidate event. The main STAR subsystems utilized for this analysis - the Time Projection Chamber, Barrel Electromagnetic Calorimeter, and the Endcap Electromagnetic Calorimeter - are indicated in Fig. 2.4 and described in the sections below.

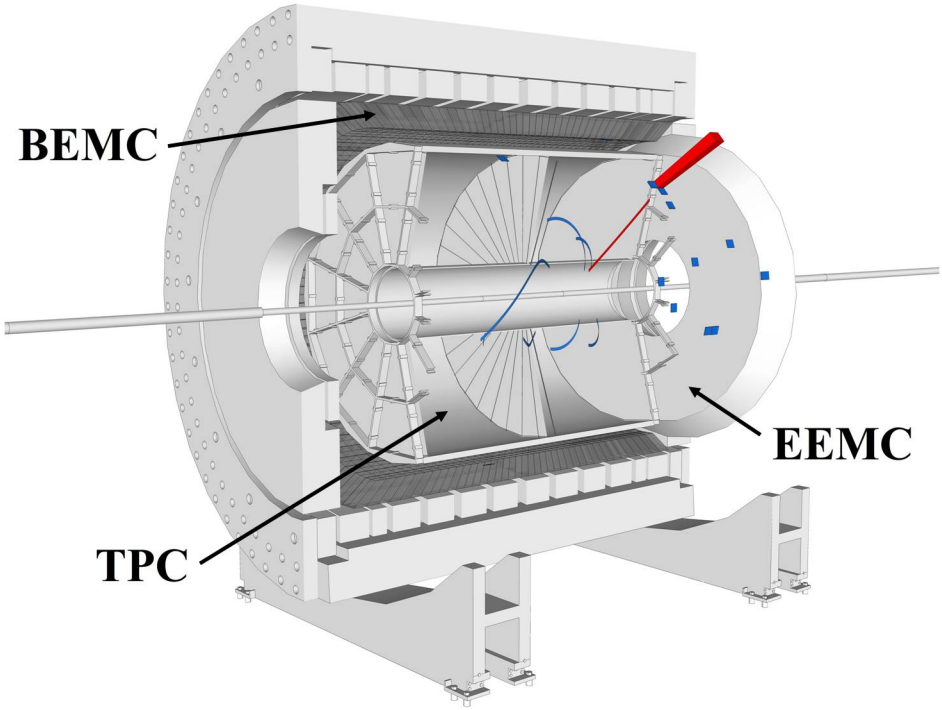


Figure 2.4: $W$ candidate event display embedded in a schematic of the STAR detector. Descriptions of the subsystems relevant for this analysis are given in Sec. 2.2

### 2.2.1 Time Projection Chamber

The main subsystem used for charged-particle track reconstruction in STAR is the Time Projection Chamber (TPC) [88]. The TPC consists of a 4.2 m long drift volume, with an inner radius of 50 cm and an outer radius of 200 cm which covers the full azimuthal angle around the beamline. The drift volume is filled with a gas mixture (P10) of 90% argon and 10% methane. Charged particles produced in collisions at the center of the STAR detector traverse the drift volume and ionize the P10 gas, producing a trail of ionization electrons along the particle's trajectory. A uniform electric field of 135 V/cm is applied parallel to the beam direction by holding the endcaps of the TPC at ground potential and the central membrane cathode at +28 kV. The ionization electrons drift toward the endcaps of the TPC where Multi-Wire Proportional Chambers (MWPCs) induce an avalanche of charge, and precision transverse position measurements of the ionization electrons are made using an array of readout pads. The drift time for the ionization electrons is measured as well to provide a track $z$ position when combined with the drift velocity, which is precisely measured and monitored using a dedicated laser system [89]. With both the position of the ionization electrons in $x - y$ space measured at the endcaps and the extracted drift time, it is possible to reconstruct the full three-dimensional trajectory of all charged particles produced in a given collision.

The TPC is also situated in a highly uniform, 0.5 T solenoidal magnetic field [90] that is parallel to the electric field direction. The trajectories of the charged particles traversing the TPC are bent into helical trajectories in the magnetic field, with a radius that is proportional to the particle's transverse momentum, $p_T$. By precisely measuring the transverse position of the ionization electrons which drift to the TPC endcaps (and thus the radius of curvature of the track), momentum measurements can be made over the pseudorapidity, $\eta = -\ln[\tan(\theta/2)]$, range $|\eta| < 1.3$ covered by the TPC. Because STAR was originally envisioned as a detector for heavy ion physics, the TPC was designed primarily to reconstruct the high multiplicity of low momentum tracks typical of heavy ion collisions. The bending

of these low momentum tracks in the magnetic field is large, which allows for precision momentum determinations. However, for the $W \to e\nu$ events of interest in this work, the decay electrons and positrons have large $p_T$, peaked at $\sim$40 GeV/$c$. For these high $p_T$ particles, the momentum measurements are less precise due to the larger radius of curvature in the magnetic field. Fortunately, the spatial resolution of the high $p_T$ tracks remains accurate down to $\sim$1-2 mm in Cartesian space, which allows for the clean separation of positive and negatively charged particles, bent in opposite directions by the magnetic field (see Sec. 4.3.3).

The TPC also measures another very useful charged-particle property: the ionization energy loss ($dE/dx$) of the particle as it traverses the gas. Because different particle species undergo different ionization energy loss as a function of momentum, the TPC provides charged particle identification for $p_T \lesssim 1$ GeV. This is very useful for many analyses, but for the separation of $e^{\pm}$ from hadronic background contamination (*e.g.,* $\pi^{\pm}$) at the scales of interest for $W \to e\nu$ events, $dE/dx$ is not very effective, and therefore has not been used in this analysis. However, the TPC was used in several other key elements of this work, including identifying high-$p_T$ $e^{\pm}$ candidates, determining the candidate charge sign, reducing contamination from QCD background, and reconstructing the $pp$ interaction vertex for the events of interest.

### 2.2.2 Barrel Electromagnetic Calorimeter

The Barrel Electromagnetic Calorimeter (BEMC) [91] is a large acceptance sampling calorimeter located in the space between the TPC and the magnet coil, and is designed to measure energy deposits from energetic electrons and photons over the pseudorapidity range $|\eta| < 1$ and over the full $2\pi$ in azimuth. It is a segmented sampling calorimeter consisting of alternating layers of lead and scintillator. The calorimeter stack contains 20 layers of 5 mm thick lead, 19 layers of 5 mm thick scintillator, and 2 layers of 6 mm thick scintillator, resulting in a total depth of $\sim$20 $X_0$ radiation lengths at $\eta = 0$, and increasing in depth with larger $|\eta|$ due to the projective geometry. The thicker scintillators form the first two layers closest to the beamline, which are used in the preshower portion of the BEMC and will not be discussed here. One of the original performance requirements of the BEMC was to contain the electromagnetic shower of an $E_T = 60$ GeV $e^{\pm}$, which was driven mostly by the requirements of the $W$ program. The depth of $\sim$20 $X_0$ radiation lengths satisfies this requirement.

The BEMC is segmented into 4800 projective towers, each of which subtends 0.05 units in pseudorapidity ($\Delta\eta$) and 0.05 radians in azimuth ($\Delta\phi$). The light produced in the 21 layers of scintillator for each tower is collected in wavelength shifting fibers, which carry the scintillation light to a single photomultiplier tube for each tower. Also, at a depth of $\sim$5.6 radiation lengths in the BEMC, there is a shower maximum detector (SMD) which provides fine grain transverse spatial resolution for electromagnetic showers. The SMD was not used in the analysis described in this thesis and will not be described in detail here.

As mentioned in the previous section, the $p_T$ resolution of TPC tracks is not ideal for the high-energy electrons and positrons that result from $W$ boson decay. However, the nominal energy resolution of the BEMC towers has been determined from cosmic ray and test beam data to be $\delta E/E = 14\%/\sqrt{E(\mathrm{GeV})} \oplus 1.5\%$ [91] which, in contrast to the TPC, improves fractionally with increased energy. Therefore, in this analysis the BEMC towers were used to reconstruct the $e^{\pm}$ energy, and only very weak requirements were placed on the TPC track $p_T$. In addition to the $e^{\pm}$ energy reconstruction, the BEMC was also used

to identify $W \to e\nu$ candidate events, both online in the trigger (by selecting events with a large, isolated electromagnetic energy deposition, see Sec. 3.1) and at the analysis stage, in reducing contamination from QCD background events by vetoing on substantial away-side energy (see Ch. 4).

### 2.2.3 Endcap Electromagnetic Calorimeter

The other large-acceptance sampling calorimeter at STAR is the Endcap Electromagnetic Calorimeter (EEMC) [92], which is located at the west end of the TPC and covers the pseudorapidity range $1.086 < \eta < 2.0$ over the full azimuthal angle. Similar to the BEMC, the EEMC is also composed of longitudinally alternating layers of lead and scintillator, and is finely segmented transversely into 720 projective towers. Each tower subtends a slightly larger area in $\eta - \phi$ space than the towers in the BEMC, covering $\Delta\phi = 0.1$ radians in azimuth and $\Delta\eta$ ranging from 0.057 to 0.099 with increasing size in $\Delta\eta$ at more forward pseudorapidity. The EEMC also contains other sub-detectors (preshower, postshower, and SMD planes) which were not used in this analysis, and thus are not discussed here.

The EEMC is also required to contain the full electromagnetic shower of the high-$p_T$ $e^{\pm}$ from $W$ decay; however, due to its more forward position, the EEMC must be deeper than the BEMC in order to contain the higher *energy* showers for a given $E_T$. Therefore in the projective geometry the EEMC is $\sim$22 $X_0$ radiation lengths deep near $\eta = 2$, and increasing to $\sim$28 $X_0$ near $\eta = 1$. While the EEMC is planned to be used in future $W$ measurements at STAR to reconstruct high-$p_T$ $e^{\pm}$ from $W$ decay, during the data taking in 2009 the charged-particle tracking capabilities at STAR were limited to the TPC, which loses tracking efficiency at $\eta \sim 1.3$. Charged-particle tracking is necessary both for reconstruction of $e^{\pm}$ candidates and for reduction of QCD background; but most importantly, it is needed to separate positive and negative charged tracks, so the $W^+$ and $W^-$ spin asymmetries can be measured independently. Therefore, a new tracker in the rapidity region covered by the EEMC, the Forward GEM Tracker [93], has been developed and was partially installed for data taking in 2012. For the analysis presented in this thesis, however, the EEMC was only used for background reduction, as described in Ch. 4.

# Chapter 3

# Data and Simulation Samples

The data analyzed in this work were collected at RHIC in 2009, using polarized proton collisions with a center-of-mass energy of $\sqrt{s}$=500 GeV. Despite the fact that this was the first time the RHIC collider had operated at this energy, an average instantaneous luminosity of $55 \times 10^{30}$ cm$^{-2}s^{-1}$ was still achieved. The average polarization of the proton beams, discussed in detail in Sec. 7.2, was ∼40% for the fills used in this analysis. In this chapter we discuss the trigger used in selecting candidate events, the integrated luminosity measurement, and finally the simulation samples generated for comparison with the data.

The data sample is subdivided into STAR "runs" or data-taking periods, which are each assigned a unique number. The list of 584 run numbers utilized in this work is given in Appendix C. Some of the data recorded early in 2009 did not have good spin information, and thus only 516 runs were used in the spin asymmetry analysis, but all runs were used in the cross section analyses where knowledge of the beam polarizations is not required.

## 3.1 Trigger Selection

Electrons and positrons from $W \rightarrow e\nu$ and $Z \rightarrow e^+e^-$ decay are characterized at mid-rapidity by a large transverse energy, $E_T$, peaked at $\sim M_W/2$ [94], known as the "Jacobian peak." Therefore, events in this analysis were selected online using a trigger that involved a two-stage localized energy requirement in the BEMC towers. The first stage required that a single BEMC tower contain a deposited energy above a threshold of $E_T = 7.3$ GeV. This decision is made at the hardware level in the trigger electronics, and is labeled the Barrel high-tower 3 (BHT3) trigger in the level-0 STAR trigger system. Additionally, a subsequent level-2 software algorithm searches for a seed tower with $E_T > 5$ GeV, and requires that the highest energy $2\times2$ tower cluster that includes that seed have an $E_T$ sum larger than 13 GeV. The events satisfying these trigger conditions were written to a separate stream of data files that contained only these events. This separate data stream allowed for rapid turnaround in analysis because of the small number of events to process. In total there were $1.2 \times 10^6$ events recorded that satisfied these conditions.

## 3.2 Integrated Luminosity Measurement

The instantaneous luminosity at the interaction region of a collider, under the assumption of beams with Gaussian transverse profiles, can be written as

$$\mathcal{L} = \frac{f_{rev} K}{2\pi\sigma_x\sigma_y}, \tag{3.1}$$

where $f_{rev}$ is the revolution frequency, $\sigma_x$ and $\sigma_y$ are the transverse widths of the beam overlap region, and $K \equiv \sum_i N_i^a N_i^b$ is the product of the bunch intensities ($N_i$) of the two beams ($a$,$b$) summed over all bunches. The intensity of each bunch is determined during a scan by the Wall Current Monitors (WCM) [95]. The transverse widths of the beam overlap region are measured using the vernier scan technique [96], which effectively determines the instantaneous luminosity. A brief description of the method is given here; a much more detailed analysis is presented in Refs. [97, 98].

A vernier scan intentionally offsets the two colliding beams from each other during a dedicated run. The position of one beam is scanned in both the $x$ and $y$ directions, independently, during the run while keeping the other beam's position fixed. Figure 3.1 shows the trigger rate (see below) as a function of the distance one beam was displaced in the $x$ or $y$ direction. The widths of the overlap region can be determined by fitting these distributions with an overlap integral of the two (Gaussian) beams

$$R(\Delta x, \Delta y) = R_{ver}^{max} e^{-\Delta x^2/2\sigma_x^2} e^{-\Delta y^2/2\sigma_y^2} + C. \tag{3.2}$$

The fit parameters are the beam overlap widths ($\sigma_x$ and $\sigma_y$), a constant term for non-collision background, and the amplitude of the distribution given by the maximum trigger rate while the beams are fully overlapping, denoted by $R_{ver}^{max}$. The dedicated trigger used for the vernier scan, and also to monitor the luminosity in this analysis, was the BHT3 level-0 trigger described in the previous section, with an additional coincident away-side $E_T$

requirement imposed offline to help reduce non-collision background. The cross section for this trigger can be written as

$$\sigma_{ver} = \frac{R_{ver}^{max}}{\mathcal{L}} \tag{3.3}$$

and can be found directly from the parameters determined by the fit in Fig. 3.1, once $K$ has been determined (see Eq. 3.1).

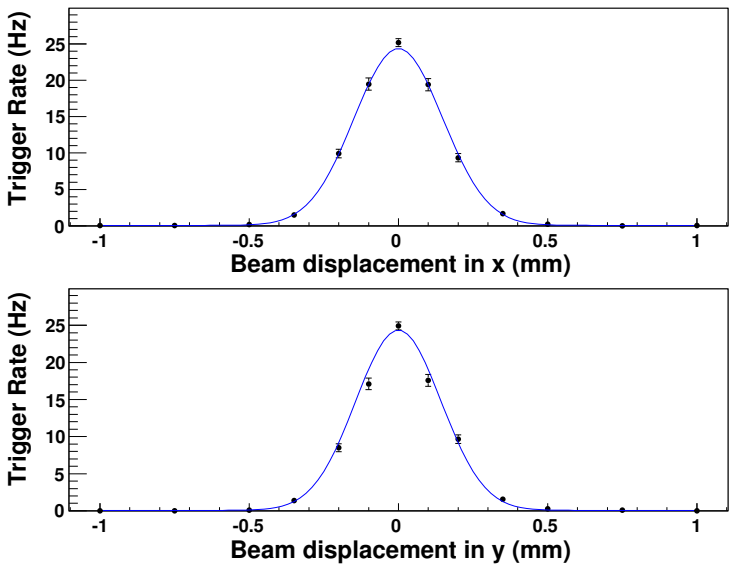


Figure 3.1: Trigger rate as a function of vernier scan beam displacement in the $x$ and $y$ directions. The transverse beam widths ($\sigma_x$ and $\sigma_y$) and maximum trigger rate ($R_{ver}^{max}$) were extracted from the fit, which is superimposed.

Two usable vernier scans were performed during the $\sqrt{s}$=500 GeV portion of the data taking in 2009. Each was analyzed separately then the results were averaged to obtain an effective cross section of $\sigma_{ver} = 434 \pm 8$ (stat) $\pm 13\%$ (syst) nb. The largest contribution to the $\sigma_{\rm ver}$ systematic uncertainty was attributed to possible non-Gaussian components of the beam profile (10%), with smaller contributions coming from possible BEMC gain drift (5%) and uncertainties in the bunch intensity measurements (4%). This value for $\sigma_{\rm ver}$ was used to normalize the total number of events which satisfied the BHT3 and awayside $E_T$ coincidence trigger conditions, resulting in an integrated luminosity for the 584 runs in the data sample of $L = \int \mathcal{L}\, dt = 13.2 \pm 0.2$(stat) $\pm$ 1.7(syst) pb$^{-1}$.

## 3.3 Simulation Samples

Monte-Carlo (MC) simulation samples were generated for this analysis in order to determine detector efficiencies, estimate background contributions from electroweak processes, and compare various predicted quantities to data. Signal samples for both the $W \to e\nu$ and $Z/\gamma^* \to e^+e^-$ channels were generated, along with a $W \to \tau\nu$ sample which is an expected background in the $W$ analysis due to the $\tau$'s leptonic decay. All of the samples were produced using the PYTHIA 6.422 (Pro-$p_T$ 0 Tune) [99] event generator and a GEANT [100] model of the STAR detector response. The same reconstruction and analysis algorithms were used for both the data and MC samples. A summary of each sample is given in Table 3.1. Unless otherwise stated, each sample was normalized to the integrated luminosity of the data.

| Samples | PYTHIA Cross Section (pb) | Integrated Luminosity (pb$^{-1}$) |
|---|---|---|
| $W^+ \to e^+ + \nu$ | 98.7 | 128.6 |
| $W^- \to e^- + \nu$ | 32.9 | 385.0 |
| $W \to \tau + \nu$ | 131.6 | 96.2 |
| $Z/\gamma^* \to e^+ + e^-$ | 23.5 | 531.9 |
| $Z \to Any$ | 240.0 | 53.1 |

Table 3.1: Summary of embedded Monte-Carlo samples.

### 3.3.1 Pile-up Effects

Due to the high luminosity of the $pp$ collision environment at $\sqrt{s} = 500$ GeV at STAR, many pile-up tracks are present in the TPC at any given time. Pile-up tracks refer to those tracks which are not associated with the triggered collision. They are produced in either another collision from the same bunch crossing as the triggered event or a collision that occurred in an earlier or later bunch crossing. Note that the bunch crossing period at RHIC is about 107 ns, while it can take up to $\sim$38 $\mu$s for track ionization to drift through the TPC. In the simulations, these pile-up tracks were accounted for by embedding the full GEANT detector response of the simulated event into a zero-bias triggered event prior to track reconstruction. The zero-bias events were selected randomly during nominal beam crossings at a rate of

$\lesssim$ 1Hz with no detector requirements, an thus yielded a good representation of the pile-up contained in the TPC for BEMC-triggered collision events. An example of the density of tracks reconstructed in a typical event is shown in Fig. 3.2, where the majority of the tracks shown are the result of pile-up. Recall that for a real $W \to e\nu$ event, there may be only one true (*i.e.,* non-pile-up) primary track from the collision, which is the decay $e^{\pm}$ track.

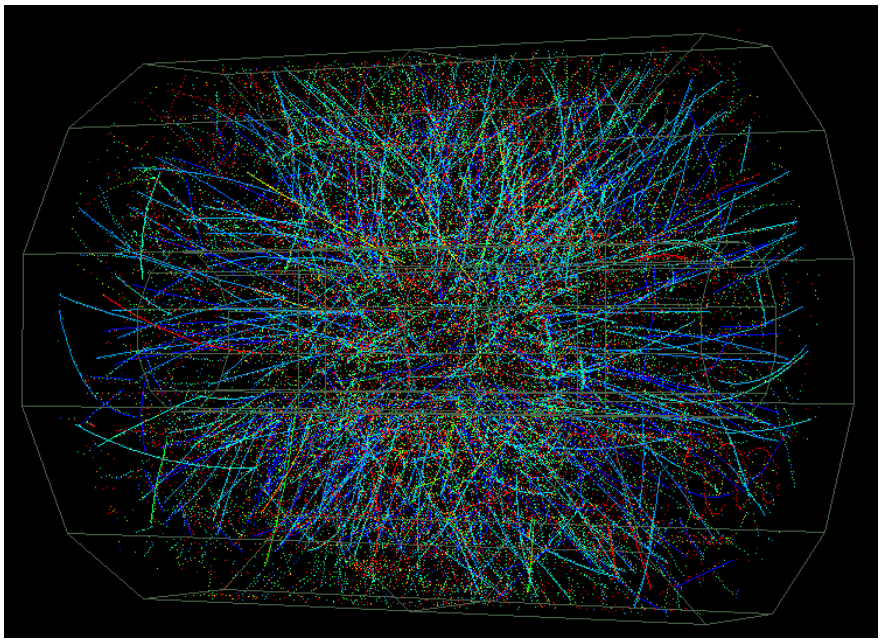

Figure 3.2: Event display of all TPC tracks recorded in a typical $pp$ event at $\sqrt{s}$=500 GeV in 2009. The vast majority of tracks are not from the triggered collision, but are instead due to pile-up as described in the text.

The density of pile-up tracks in the TPC scales approximately linearly with instantaneous luminosity. Therefore, it is important to ensure that the zero-bias events used in the embedded simulations contain events taken with the same instantaneous luminosity (and thus pile-up) as the real data in order to accurately reproduce the effects of pile-up in the embedded simulations. To do this one must correct for two effects:

1. During the startup process at the beginning of the 2009 data-taking, the zero-bias events were not recorded as a part of the standard trigger configuration. Thus, there are not enough zero-bias events from the early data-taking period relative to the $W$

triggered data (see the upper left panel of Fig. 3.3, showing no zero-bias events in the first ∼150 runs).

2. Also, the zero-bias trigger accumulates events at an approximately constant (and hence luminosity independent) rate, whereas the trigger used for this analysis (described in Sec. 3.1) increases in rate with luminosity, so there are not enough zero-bias events at the highest luminosities compared to the $W$ triggered data. This can be seen in the lower right plot of Fig. 3.3 where the ratio of zero-bias events to integrated luminosity is seen to decrease with ZDC coincidence rate.

The ZDCs (Zero Degree Calorimeter [101]) are two very far forward calorimeters, which can detect a coincidence between hits on each side of the interaction region within a short time window, consistent with a hard collision in a particular bunch crossing. The rate of these ZDC coincidences is proportional to the instantaneous luminosity, and was therefore used to study luminosity-dependent effects in this analysis.

To compensate for the two effects described above, some zero-bias events were used multiple times, with different simulated PYTHIA events, so that the zero-bias events accurately represented the pile-up environment seen in the $W$ triggered dataset. The resulting distribution of luminosity and zero-bias events as a function of ZDC rate, after some zero-bias events were used multiple times, are shown in Fig. 3.4. It is also important to note that zero-bias events from the bunch crossings in the abort gaps have been removed from the simulation samples, since there are no colliding bunches in these crossings in the data.

Finally, the PYTHIA events in the simulation samples were generated assuming a Gaussian $z_{\text{vertex}}$ distribution with a width of 42.2 cm, which roughly matches the data distribution. However, the $z_{\text{vertex}}$ distribution from the data has slightly longer tails, at large $|z_{\text{vertex}}|$, than the generated simulation distribution. To account for this, the events were re-weighted to yield the same $z_{\text{vertex}}$ distribution for the embedded simulation samples as the data (shown in Fig. 3.5).

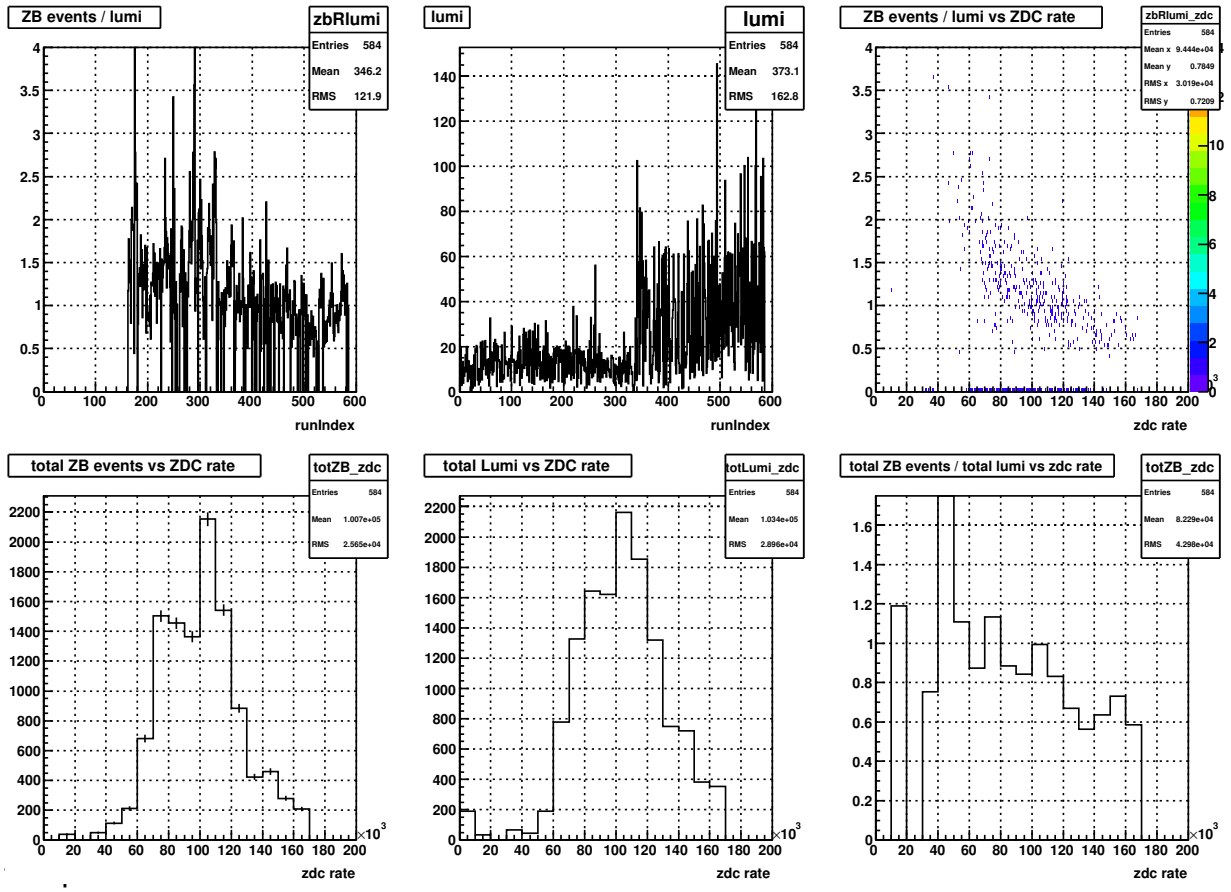


Figure 3.3: Raw distributions of zero-bias events and integrated luminosity using each zero-bias event once.
Top row (L to R): (# zero-bias events)/(Integ. Lumi.) vs RunID; Integ. Lumi. vs RunID; (# zero-bias events)/(Integ. Lumi.) vs. ZDC coin. rate.
Bottom row (L to R) Total # zero-bias events vs ZDC coin. rate; Total Integ. Lumi. vs ZDC coin. rate; Total (# zero-bias events)/(Integ. Lumi.) vs ZDC coin. rate.

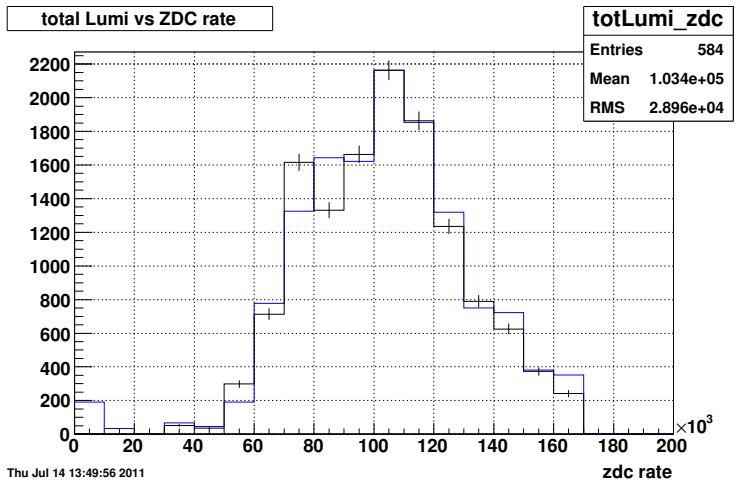


Figure 3.4: Total integrated luminosity as a function of ZDC coincidence rate (blue) and normalized number of zero-bias events as a function of ZDC coincidence rate.

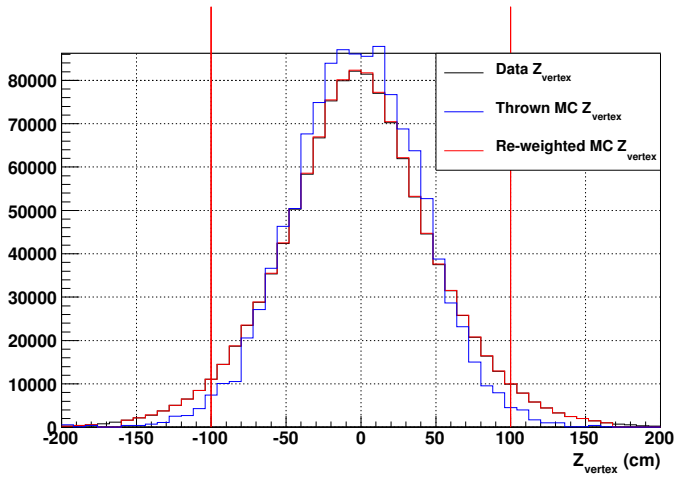


Figure 3.5: $z_{\text{vertex}}$ distributions of data (black), generated embedding (blue), and re-weighted embedding (red).

# Chapter 4

# $W$ and $Z$ Signal Reconstruction

This chapter details the identification and reconstruction of $W$ and $Z$ candidate events, as well as the reduction of the large QCD background. This reduction is achieved through cuts designed to take advantage of the kinematical and topological differences between the electroweak processes of interest and QCD processes. The following sections describe the steps involved in identifying isolated candidate electrons and positrons, and then selecting $W$ and $Z$ candidate events.

The process of selecting $W$ and $Z$ candidate events begins at the trigger level, as discussed in Sec. 3.1. Events satisfying these trigger conditions were written to a dedicated event "stream" of data files to allow for fast processing through the STAR offline event reconstruction framework. This offline event reconstruction includes, among other things, reconstructing charged particle tracks in the TPC and reconstructing the collision vertex of the triggered event, which is the subject of the following section.

## 4.1 Primary Vertex Finder

In Sec. 3.3.1 the effects of multiple event pile-up were discussed in terms of the high multiplicity of tracks in the TPC that are not associated with the triggered collision. To reconstruct the triggered collision vertex, also known as the primary vertex, from the multitude of vertices produced by the large number of pile-up tracks in this environment, a dedicated vertex reconstruction package was developed, known as the Pile-up Proof Vertex finder (PPV) [102]. It was designed to determine the primary vertex location along the beam axis for low multiplicity events (*e.g.,* $W \to e\nu$ decays) which are embedded in pile-up that is two orders of magnitude larger.

All tracks reconstructed in the TPC are denoted as global tracks in the STAR framework. PPV uses all the global tracks to reconstruct all possible vertices in the event. During this process, two criteria are used to help separate pile-up tracks from tracks associated with the triggered collision vertex. First, each track is extrapolated to the barrel or endcap calorimeter towers outside the TPC volume, to determine whether it matches with an energy deposition in the tower pointed to by the track. Tracks are also checked to see if TPC hits from both sides of the TPC central membrane were used in the track reconstruction. Tracks satisfying either of these two conditions are likely to be from the triggered bunch crossing, and therefore the vertex to which they belong is very likely the primary vertex. Therefore, weighting these tracks more heavily in the vertex reconstruction strongly reduces the contamination from pile-up.

PPV finds the position of the primary vertex along the $z$-axis (*i.e.,* the beam direction) from the center of the STAR interaction region, which is referred to as the $z_{\text{vertex}}$ of the collision. This $z_{\text{vertex}}$ is the weighted mean of all global tracks approaching within 3 cm of the beamline, with track weights depending on the number and distribution of TPC hits used to reconstruct the track, and a weighted multiplier based on the calorimeter and central membrane matching described above. For a valid primary vertex, PPV requires either at least two high quality, matched track candidates originating from the same $z_{\text{vertex}}$ location,

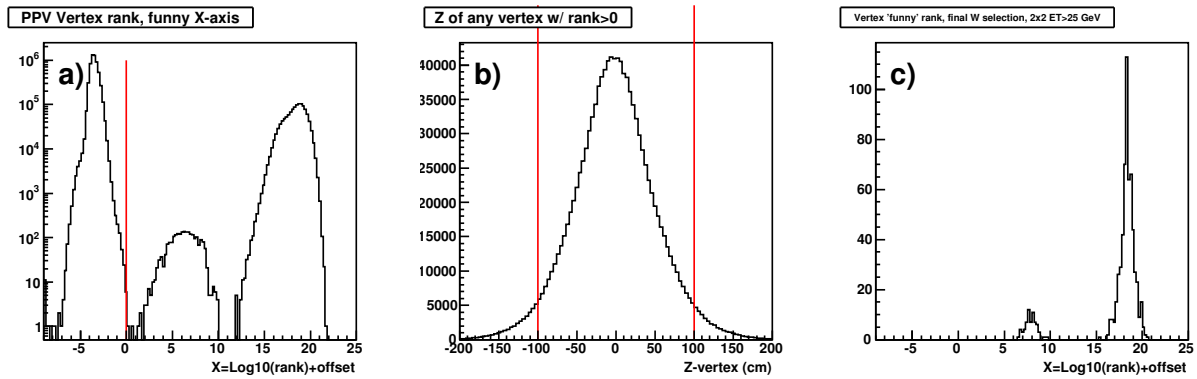


Figure 4.1: Properties of primary vertices reconstructed by PPV: a) rank of all vertices, b) $z_{\text{vertex}}$ distribution for vertices with rank $>$ 0, and c) rank of vertices for reconstructed $W$ candidates (described in Sec. 4.3).

or a single track with $p_T > 10$ GeV/$c$ matched to an energy deposit in a calorimeter tower. Several vertices in each event are typically reconstructed by PPV that satisfy these conditions. They are classified by what is known as the "rank," which is loosely correlated with the likelihood of a given vertex being matched to the triggered collision vertex. Figure 4.1 (a) shows three groups of vertices found in the data:

- Vertices having negative rank are rejected from the analysis; these are overwhelmingly due to pile-up
- Single high-$p_T$ track vertices are in the middle peak;
- Two or more track vertices form the peak on the right.

The $z_{\text{vertex}}$ distribution of primary vertices with rank $>$ 0 is approximately Gaussian with an RMS width of 52 cm, as seen in Fig. 4.1 (b). Figure 4.1 (c) shows the rank distribution for good $W$ candidate events. A significant fraction of these belong to single track vertices (note the logarithmic and linear scale, for Fig. 4.1 (a) and (c), respectively). To maximize the efficiency of the reconstruction algorithm, all vertices with $|z_{\text{vertex}}| < 100$ cm and rank $>$ 0 are included in this analysis.

## 4.2 Identification of High-$E_T$ Isolated $e^{\pm}$ Candidates

### 4.2.1 Track Quality Requirements

The reconstructed tracks associated with the primary vertices satisfying the requirements described in the previous section are known as primary tracks, and they form the sample of tracks which are considered as possible electron or positron candidates. Some additional track quality requirements are imposed to ensure that the track and its charge sign are well reconstructed, as well as to reject pile-up tracks which may be incorrectly associated with a primary vertex. An $e^{\pm}$ candidate track is required to have:

- a minimum of 15 TPC points used in reconstruction;
- more than 51% of the maximum number of TPC points allowed used in reconstruction;
- the radius of the track hit nearest to the beamline $< 90$ cm;
- the radius of the track hit farthest from the beamline $> 160$ cm.

Figure 4.2 shows where these cuts are placed on the data in order to select quality tracks. In the data set used in this analysis, there were some TPC sectors with dead regions due to electronics problems. The requirements on the radius of the track hit nearest and farthest from the beamline in these sectors were relaxed to increase efficiency during the periods when these regions were dead.

The final track candidate cut required that a candidate's primary track have $p_T > 10$ GeV/$c$. This is a rather low threshold, as the majority of the $W \to e\nu$ candidates at mid-rapidity are expected to have an $e^{\pm}$ with $E_T \sim 40$ GeV. However, the momentum resolution of the TPC deteriorates at high $p_T$, so to avoid efficiency losses an $e^{\pm}$ candidate is only required to have a primary track $p_T > 10$ GeV/$c$. No further restrictions are placed on the candidate tracks.

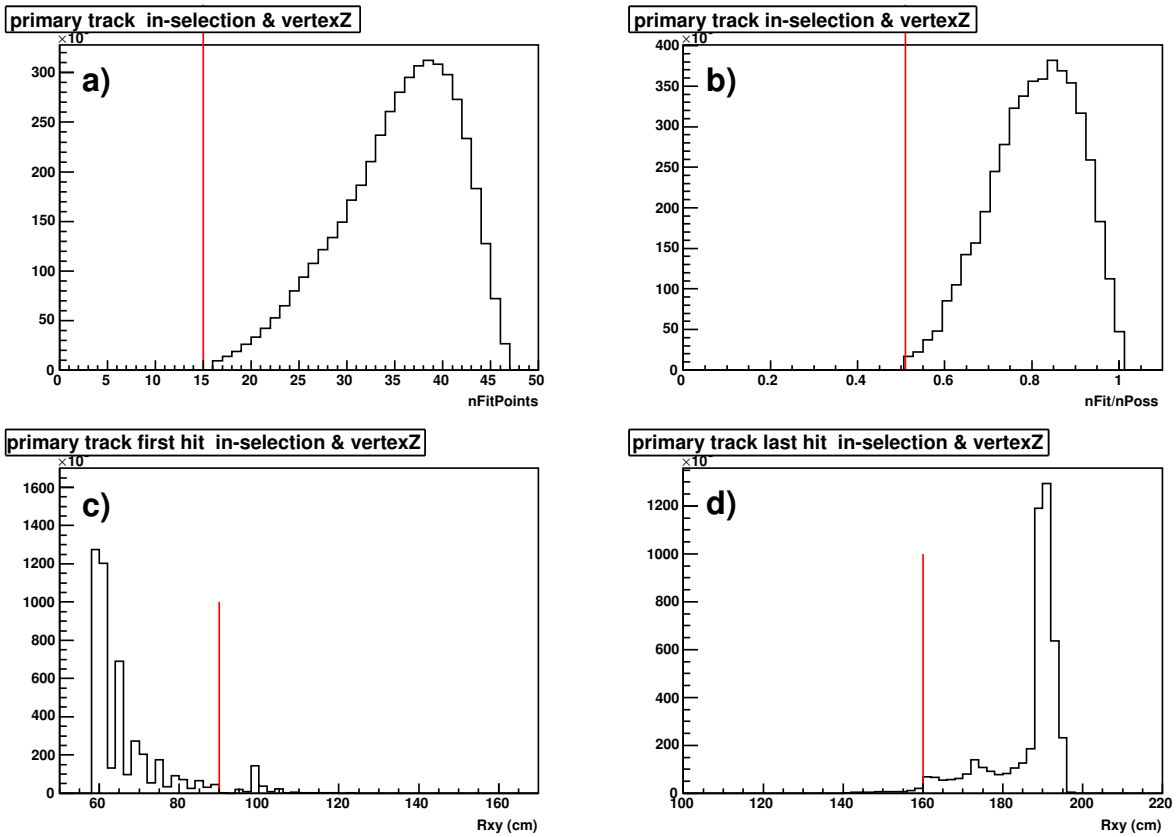


Figure 4.2: Track quality variables, where the values of the quality requirements are shown in red: a) Number of TPC points used in track reconstruction, b) Fraction of the maximum number of TPC points allowed used in track reconstruction, c) Radius of the track hit nearest to the beamline, and d) Radius of the track hit farthest from the beamline.

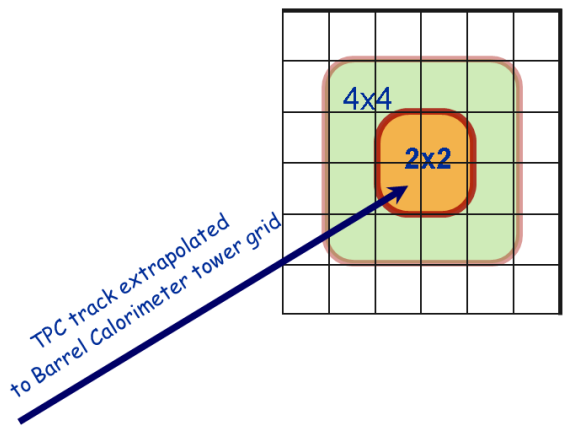


Figure 4.3: Diagram of extrapolating the candidate $e^{\pm}$ track to the front of the BEMC tower grid and reconstruction of the highest $E_T$ 2×2 tower cluster pointed to by the track, as well as the 4×4 tower cluster used in the isolation requirement described in Sec. 4.2.3.

### 4.2.2 Track and Cluster Matching

The electron and positron candidate tracks satisfying all the requirements discussed in the previous section are extrapolated to the BEMC, as shown by the diagram in Fig. 4.3. The extrapolated track is then used to determine which BEMC tower the candidate was pointed towards. There are four possible combinations of 2×2 BEMC tower clusters which contain the tower pointed to by the candidate track, and the $E_T$ sum of each of these four clusters is computed. The 2×2 cluster with the largest summed $E_T$ is assigned to the $e^{\pm}$ candidate, and this sum is the measure of the candidate's transverse energy, denoted as $E_T^e$.

Two conditions were required for BEMC tower cluster associated with the $e^{\pm}$ candidate. The first requirement is that the cluster $E_T^e > 15$ GeV, which assures that the transverse energy is well above the trigger threshold, which was set at 13 GeV for the 2×2 cluster. The other cluster requirement is that the magnitude of the two-dimensional distance between the energy log-weighted centroid of the tower cluster and the extrapolated TPC track position, $|\Delta\vec{r}|$, be less than 7 cm. By matching the position of the BEMC tower cluster to the extrapolated TPC track, we reject candidates where the energy deposited in the BEMC cluster may not have originated from the particle which produced the TPC track. These

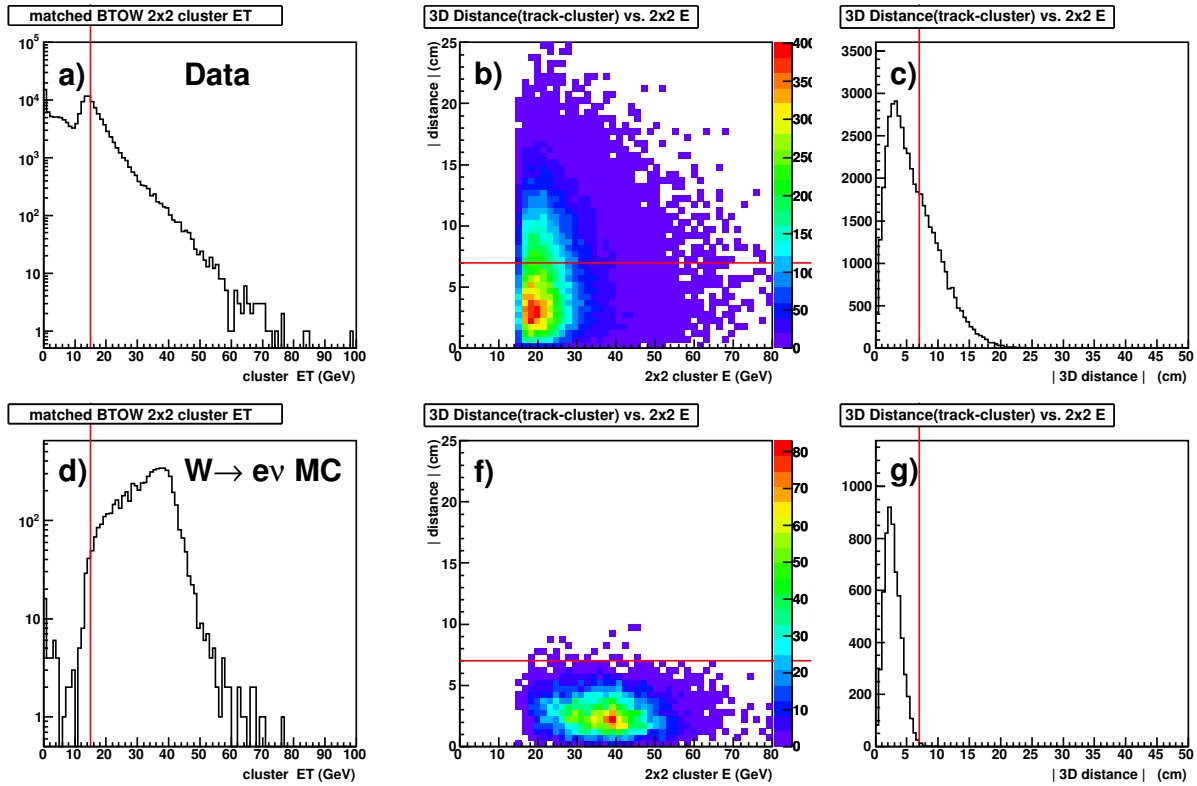


Figure 4.4: Distributions for matching candidate track and BEMC tower clusters for data and $W \to e\nu$ MC: (a) and (d) 2×2 cluster $E_T$, (b) and (e) 2D distance between extrapolated track and centroid of tower cluster vs. $E_T^e$, (c) and (f) 2D distance between extrapolated track and centroid of tower cluster.

two cluster cuts are shown by the red lines in Fig. 4.4 for the data and for the $W \to e\nu$ MC simulations.

### 4.2.3 Isolation Requirements

Electrons and positrons from $W$ and $Z$ decay should be well isolated from other particles in $\eta - \phi$ space; thus, the next step in the candidate reconstruction process is to require that the $e^{\pm}$ candidates satisfy two isolation conditions. The first isolation cut requires that the ratio of $E_T^e$ to the $E_T$ sum of the 4×4 BEMC tower cluster surrounding the candidate, $E_T^e/E_T^{4\times4}$, be greater than 95% (see diagram in Fig. 4.5). Because the $e^{\pm}$ from $W$ and $Z$ decay should deposit essentially all their energy in the candidate 2×2 BEMC tower cluster, this initial isolation requirement is fairly tight in order to reduce a significant amount of background,

yet still retain essentially all the signal, as seen in Fig. 4.5 (a) and (c).

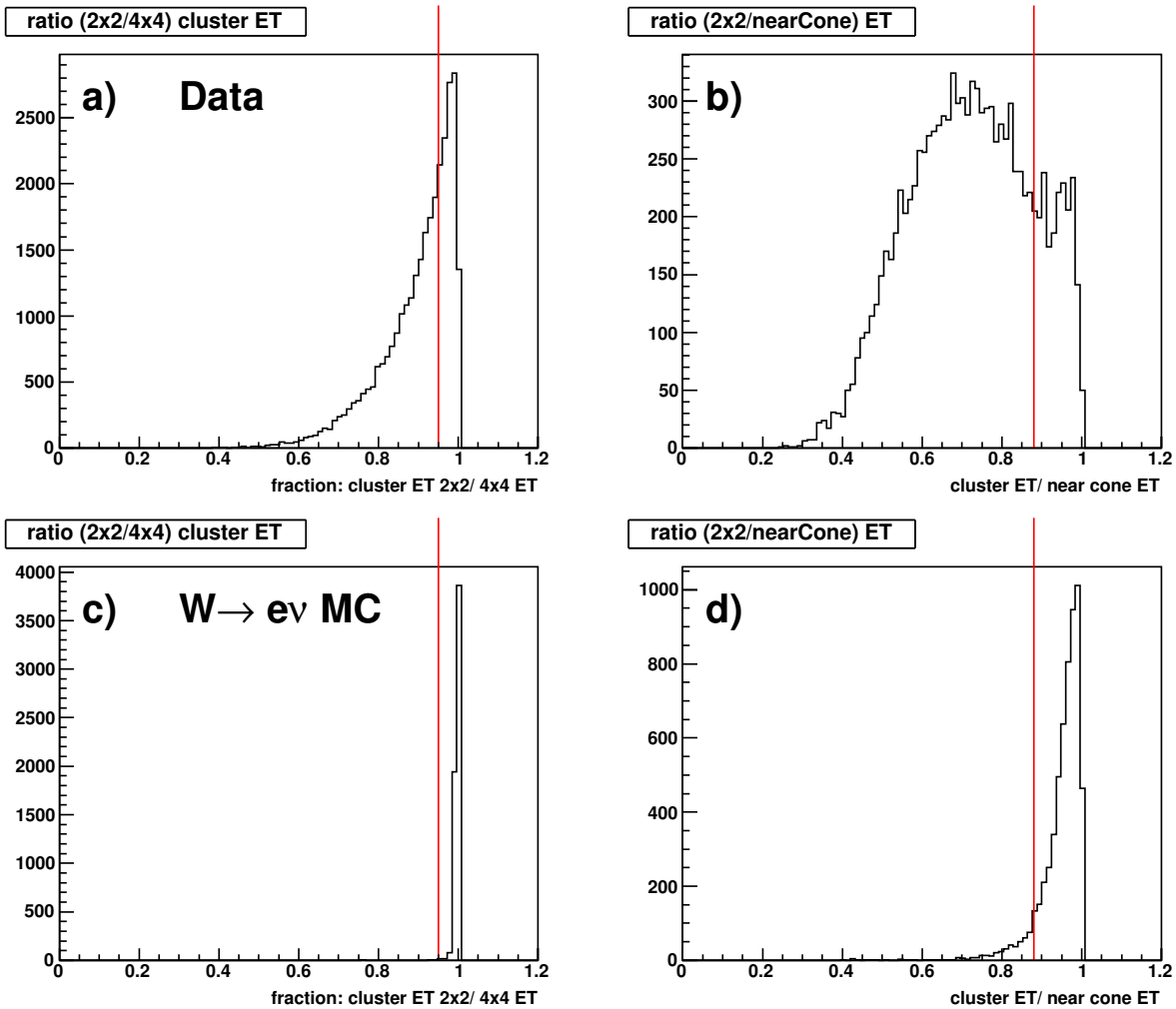


Figure 4.5: $e^{\pm}$ candidate isolation cut ratio distributions for data and $W \to e\nu$ MC: (a) and (c) Cluster isolation ratio $E_T^e/E_T^{4\times4}$; (b) and (d) Near-side cone sum ratio $E_T^e/E_T^{\Delta R<0.7}$.

The other isolation requirement is imposed to reduce jet-like events, and uses a larger area than the previous 4×4 cluster isolation condition. The sum of transverse energies over this larger area, $E_T^{\Delta R<0.7}$, is defined as the sum of all BEMC and EEMC tower $E_T$ and TPC track $p_T$ within a cone radius of $\Delta R \equiv \sqrt{\Delta\eta^2 + \Delta\phi^2} < 0.7$ around the candidate track. The $e^{\pm}$ candidate track is excluded from the sum of TPC track $p_T$ to avoid double-counting the candidate's energy in the $E_T^{\Delta R<0.7}$ sum. Figure 4.6 shows a diagram of the $e^{\pm}$ candidate and the region that is summed in this cone around the $e^{\pm}$. This quantity $E_T^{\Delta R<0.7}$, known

as the "near-side cone sum," is used to form the ratio $E_T^e/E_T^{\Delta R<0.7}$ which is required to be greater than 0.88. The distribution of this isolation ratio is shown in Fig 4.5 (b) and (d) for the data and $W \to e\nu$ MC, respectively. To maintain a high efficiency, use of this larger area necessitates using a slightly looser condition on this isolation ratio than the tight condition on the $E_T^e/E_T^{4\times4}$ ratio However, even with this lower value for the ratio condition, a large fraction of the jet-like background events are removed by this requirement.

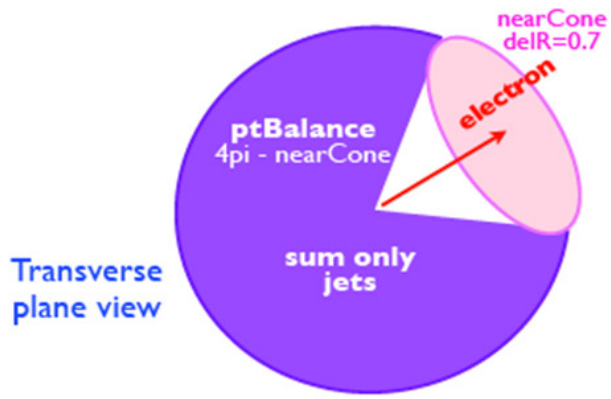


Figure 4.6: Diagram of an $e^{\pm}$ candidate (red) in the transverse plane, surrounded by a "near-side cone" (pink) in which the BEMC and EEMC tower $E_T$ and TPC track $p_T$ are summed to determine $E_T^{\Delta R<0.7}$. The purple region is where the transverse components of the reconstructed jet momenta are summed to construct the $p_T$-balance vector for $W$ event selection as described in Sec. 4.3.

## 4.3 $W$ Candidate Event Selection

All events with an isolated $e^{\pm}$ candidate that satisfied the conditions described in Sec. 4.2, were considered for $W \to e\nu$ candidate event selection. The selection of $W \to e\nu$ candidate events is based on differences in the event topology between leptonic $W$ decays and the QCD background or $Z \to e^+e^-$ events. $W \to e\nu$ events contain a nearly isolated $e^{\pm}$ with a neutrino close to opposite in azimuth. Electrons and positrons emitted near mid-rapidity from $W$ decay are characterized by a large $E_T^e$ that peaks near half the $W$ mass ($\sim$40 GeV) with a distribution referred to as a Jacobian peak. There is also a large "missing" transverse energy in $W \to e\nu$ events that is opposite in azimuth to the $e^{\pm}$, due to the undetected neutrino. As a result, there is a large imbalance in the vector $p_T$ sum of all reconstructed final-state objects for $W$ events. In contrast, $Z \to e^+e^-$ events and QCD hard-scattering events, such as di-jets, are characterized by a small magnitude of this vector $p_T$ sum imbalance. The following section describes a new variable developed in our analysis to take advantage of this difference in event topologies between the $W \to e\nu$ signal and its backgrounds.

### 4.3.1 Signed $P_T$-Balance Requirement

The final requirement for $W$ candidate events demands a large missing transverse energy opposite in $\phi$ to the $e^{\pm}$ candidate discussed above. The implementation of this missing transverse energy requirement is done by first constructing a $p_T$ balance vector, $\vec{p}_T^{\,bal}$, which is a vector sum of the $e^{\pm}$ candidate's $p_T$ vector and the $p_T$ vectors of all reconstructed jets whose thrust axes are *outside* the near-side cone described in Sec. 4.2.3:

$$\vec{p}_T^{\,bal} = \vec{p}_T^{\,e} + \sum_{\Delta R > 0.7} \vec{p}_T^{\,jets}. \tag{4.1}$$

The $e^{\pm}$ candidate $p_T$ vector, $\vec{p}_T^{\,e}$, is composed of a momentum direction defined by the candidate TPC track and a magnitude determined by the BEMC tower cluster energy, $E_T^e$. The $\vec{p}_T^{\,jets}$ vectors summed in the second term on the right side of Eq. 4.1 are for

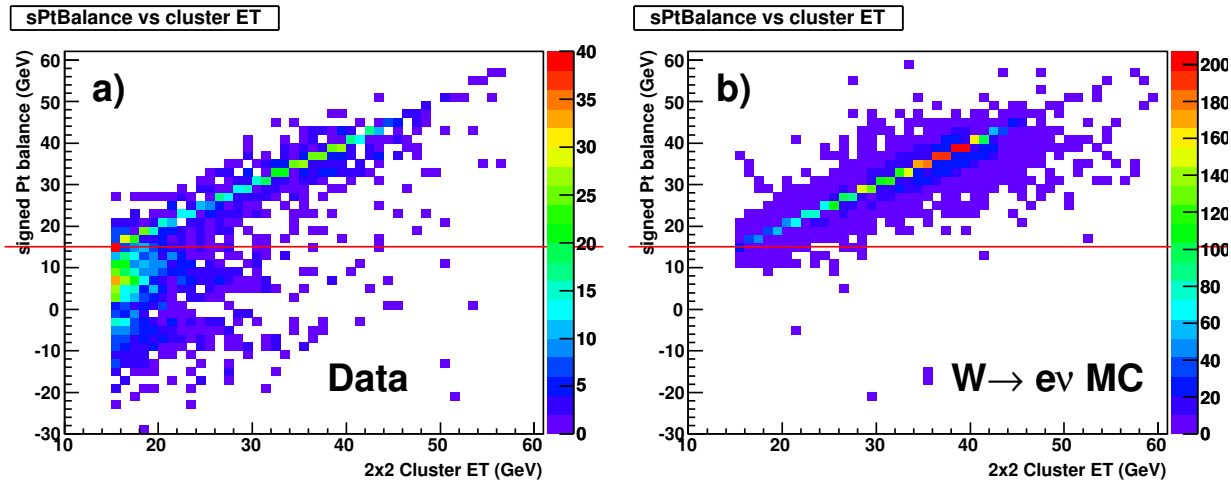


Figure 4.7: Signed $p_T$-balance vs. $E_T^e$ for data (a) and $W \to e\nu$ MC (b).

jets reconstructed using a standard mid-point cone algorithm described in previous STAR publications [103]. Jets are reconstructed based on tracks from the TPC and tower energies from the BEMC and EEMC. A list of the relevant algorithm parameters from the STAR jet-finder software [104] is given in Appendix A.

A scalar "signed $P_T$-balance" variable is then defined as the magnitude of the $p_T$ balance vector, with the sign given by the dot product of the $p_T$ balance vector and the $e^{\pm}$ candidate $p_T$ vector,

$$\text{signed } P_T\text{-balance} = \text{sign}\left(\vec{p}_T^{\,e} \cdot \vec{p}_T^{\,bal}\right) \left|\vec{p}_T^{\,bal}\right| . \tag{4.2}$$

This quantity is required to be larger than 15 GeV/$c$ as indicated by the red dashed line in Fig. 4.7, which shows the signed $P_T$-balance variable as a function of $E_T^e$. For $W$ decay events, these two variables are highly correlated because the energy in reconstructed jets whose thrust axes are outside the near-side cone is very small. This can be seen clearly in Fig. 4.7 b) which shows the correlation for the $W \to e\nu$ MC simulation. The data show a similar correlation at high $E_T^e$, where the sample is dominated by signal, showing the validity and critical importance of this condition. At low $E_T^e$, where contributions from QCD background events are larger, most events have a small value for the signed $P_T$-balance variable, as expected.

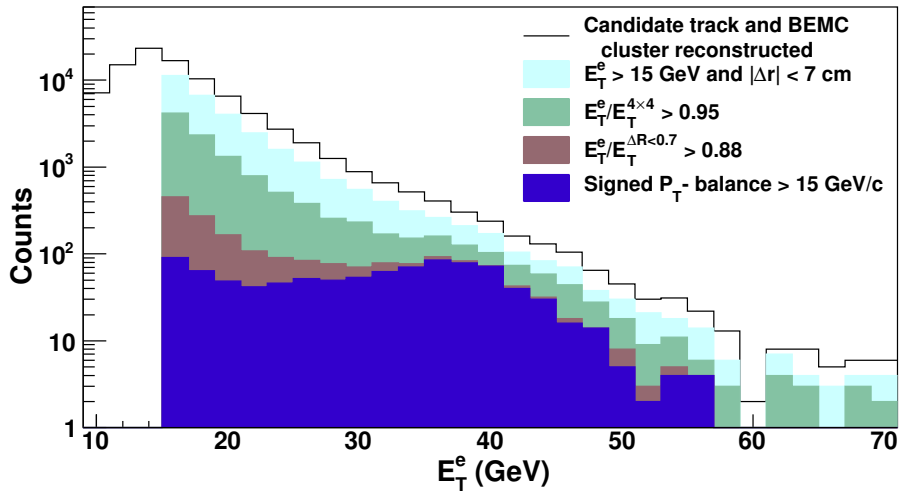


Figure 4.8: Candidate $E_T^e$ distribution from the data after various cuts described above.

### 4.3.2 Reduction of Background by Cuts

The reduction of the $W$ candidate yield after each of the $W$ candidate event selection criteria can be seen in Fig. 4.8. Shown as a function of $E_T^e$, the $W$ candidate yield begins initially with only the requirement of a candidate TPC track and BEMC tower cluster being reconstructed. This distribution (solid line) is dominated by QCD background, which falls exponentially with $E_T^e$, and there is no evidence of the Jacobian peak. The $E_T^e$ distribution is shown again after each of the $W$ candidate event selection requirements (as detailed in this chapter) have been imposed reducing the dominant QCD background by several orders of magnitude. The final $W$ candidate yield after all the cuts have been applied (dark blue filled) shows a clear signal above the steeply falling QCD background at $E_T^e \sim M_W/2$.

### 4.3.3 Charge Sign Reconstruction

The curvature of tracks reconstructed in the TPC contains two vital pieces of information for this analysis. The magnitude of the track curvature provides a measure of $1/p_T$ for the track which in this analysis is used in a very limited way due to the poor momentum resolution at high $p_T$. The sign of the curvature (bending left or right in the magnetic field), however is

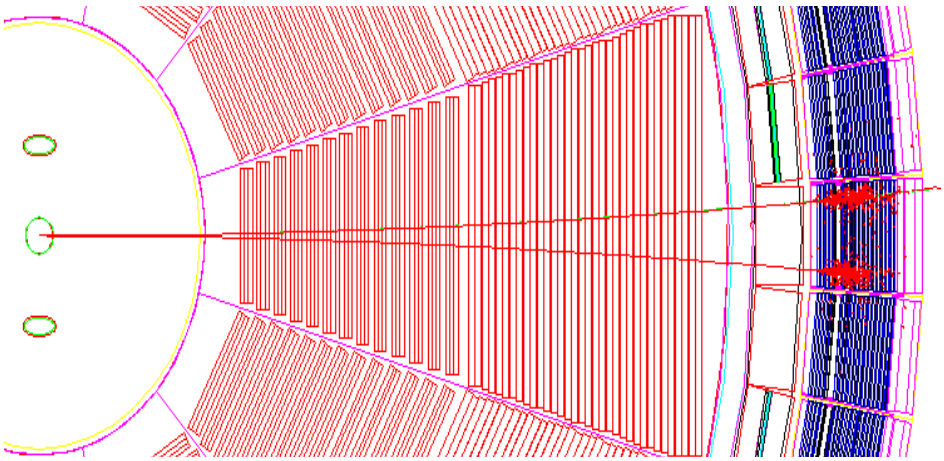

Figure 4.9: GEANT simulation of separation distance between a positron and electron with $p_T = 5$ GeV/$c$ bending in the 0.5 T magnetic field at STAR.

critical for this analysis to separate electrons from positrons and thus discriminate $W^+$ from $W^-$ production. The separation of electrons and positrons is critical because the single spin asymmetries for $W^+$ and $W^-$ are expected to have opposite sign. Therefore, contamination from the opposite charge sign will diminish the asymmetry signal.

For charged particles with a $p_T$ of 5 GeV/$c$, the bending induced by the magnetic field results in a displacement of $\sim$ 15 cm at the outer edge of the active TPC volume, as shown in Fig. 4.9. The $p_T$ of electrons and positrons decaying from $W$s at mid-rapidity, however, are much higher ($\sim$ 25-50 GeV/$c$). Therefore, the displacement is much smaller (on the order of $\sim$ 1-2 cm), making it more challenging to distinguish the two charge signs. Adding to the complication is the large amount of space charge in the TPC caused by pile-up events in the high-luminosity environment of $pp$ collisions at $\sqrt{s}$ 500 GeV (discussed in Sec. 3.3.1). The presence of this space charge ionization and other factors requires that distortion corrections (on the order of a few cm) be made to the reconstructed TPC cluster positions to compensate for these effects.

The resulting charge separation plot is shown in Fig. 4.10, which displays the reconstructed candidate TPC track charge sign, multiplied by $1/p_T$, as a function of $E_T^e$ measured in BEMC towers for events satisfying all the $W$ candidate event selection requirements. The

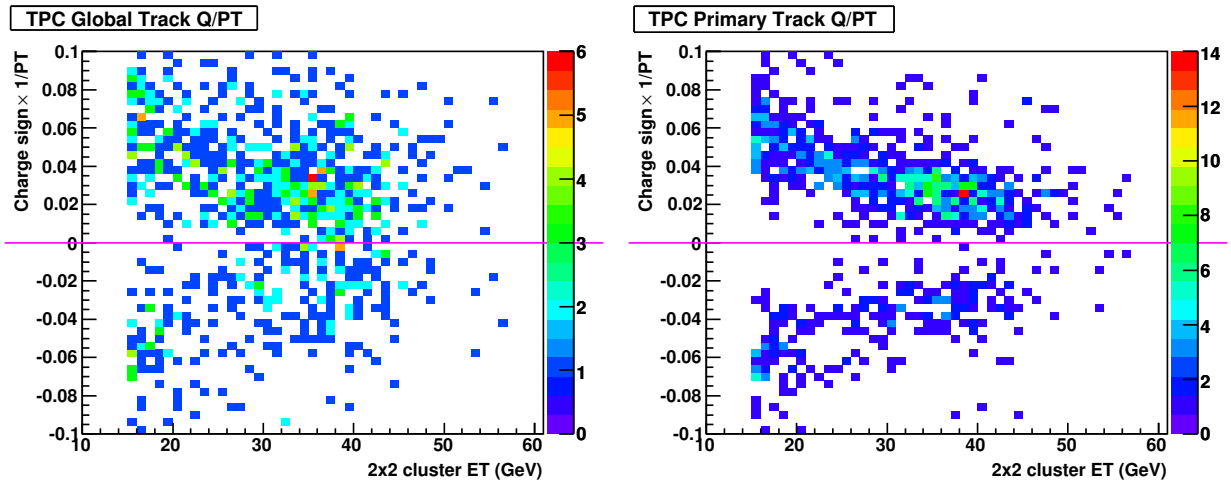


Figure 4.10: Product of the reconstructed candidate TPC track charge sign and $1/p_T$ as a function of $E_T^e$ measured in BEMC towers for events satisfying all the $W$ candidate event selection requirements. Global tracks are on the left and primary tracks on the right.

left panel shows the global tracks, which are reconstructed before the vertex position is found, while the right plot shows only the primary tracks which include the vertex position in the track reconstruction fit. The inclusion of the vertex position in the fit is seen to have a significant impact on the $1/p_T$ resolution. Finally, the clear valley observed between the opposite charge signs up to $E_T^e \sim 50$ GeV demonstrates the effectiveness of the charge sign discrimination of the TPC at the energies relevant for this measurement.

### 4.3.4 Charge Separated Yields

After all the reconstruction and event selection requirements described in the previous sections have been imposed, the raw $W$ candidate yields are shown as a function of $E_T^e$ in Fig. 4.11. The characteristic Jacobian peak for the decay $W \to e\nu$ decay is clearly seen above the QCD background at $E_T^e \sim M_W/2$ for both the $W^+$ and $W^-$ events.

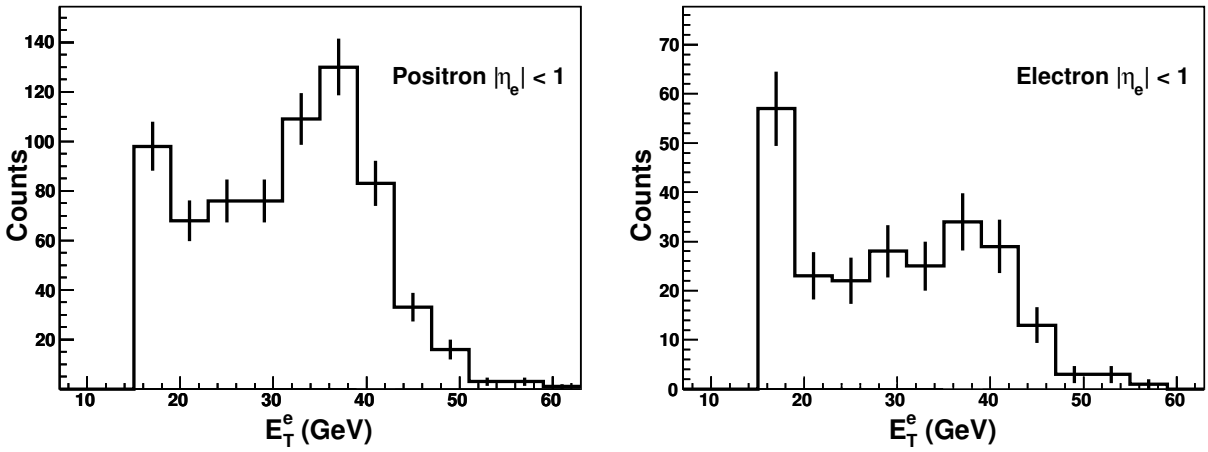


Figure 4.11: Raw $W$ candidate yields as a function of $E_T^e$ after passing all selection cuts ($W^+$ on the left and $W^-$ on the right).

## 4.4 $Z$ Candidate Event Selection

The selection of $Z$ candidate events begins with the same isolated $e^\pm$ sample as the $W$ selection, described in Sec. 4.2. $Z \to e^+e^-$ events were selected by requiring that a pair of isolated $e^\pm$ candidates, with opposite charge signs, be reconstructed in the candidate event. The invariant mass of each $e^+e^-$ pair is then reconstructed.

### 4.4.1 Reduction of Background by Cuts

The invariant mass distributions of the reconstructed $Z$ candidates are shown in Fig. 4.12 after each of the selection criteria described in Sec. 4.2 has been satisfied for both the $e^+$ and $e^-$ candidates. The $e^\pm$ selection and isolation criteria clearly also reduce the QCD background for the $Z$ signal. When only the pair of TPC tracks and BEMC tower clusters is reconstructed, the distribution (solid line) contains significant background at low mass; however, the signal at $m_{e^+e^-} \sim M_Z$ is clearly evident over the background even with these minimal requirements. After all of the selection requirements have applied, the clear signal near the $Z$ mass remains. Additionally, there is an indication of a small signal at lower invariant mass which is likely the result of lower mass Drell-Yan pairs. This is consistent

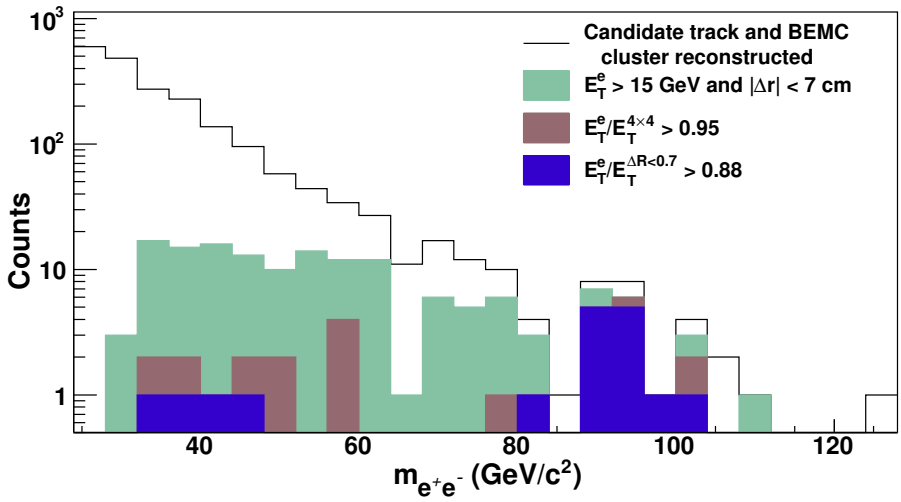


Figure 4.12: Reconstructed $e^+e^-$ invariant mass distributions after the various cuts described in section 4.2 have been applied.

with the expectation from the $Z/\gamma^* \to e^+e^-$ MC simulation, as shown in Fig. 4.13.

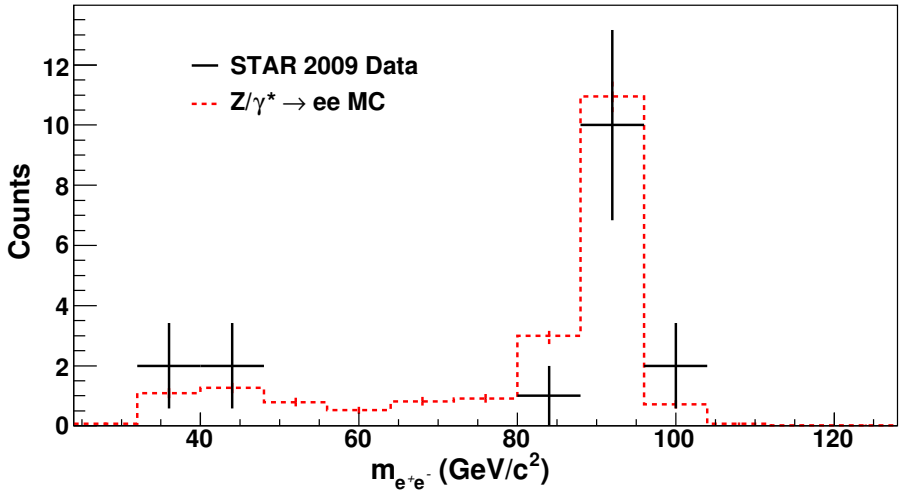


Figure 4.13: Invariant mass distribution of the final $Z$ candidate yield, compared to the $Z/\gamma*$ signal MC yield.

# Chapter 5

# Background Estimation

## 5.1 Background Estimation for $W$ Signal

The selection of $W$ candidate events, described in Sec. 4.3, was developed to identify events consistent with $W \to e\nu$ event topologies, and to reduce contributions from hard scattering QCD background events (*e.g.,* di-jets). Despite a significant reduction of QCD background in this selection process, some QCD background events will still resemble $W \to e\nu$ events when a jet fragments in such a way that it satisfies the isolated electron requirements. Our detector acceptance effects can then allow these events to satisfy the remaining $W \to e\nu$ event selection criteria. There are other background processes that can contribute to the $W \to e\nu$ candidate yield as well. Other electroweak processes, such as $W \to \tau\nu$ and $Z \to e^+e^-$, yield isolated electrons, which can be effectively indistinguishable from $W \to e\nu$ events, resulting in some contamination from these processes. This section describes how the contributions of these background processes are accounted for, using simulation to estimate the electroweak components and "data-driven" methods to estimate the QCD contributions.

### 5.1.1 $W \to \tau\nu$ Background

$W$ bosons decay to $\tau + \nu$ with a branching ratio of $\sim 11\%$. This decay branch of the $W$ contaminates the $W \to e\nu$ signal when the $\tau$ decays leptonically to $e + \nu_e + \nu_\tau$, which occurs with a branching ratio of $\sim 13\%$. These $W \to \tau\nu \;\to\; e\nu\nu\nu$ events contain an isolated $e^\pm$ with a large missing energy opposite in azimuth, making it effectively indistinguishable from the $W \to e\nu$ signal. However, the $e^\pm$ produced in $\tau$ decay must share the energy of the $\tau$ with the two secondary neutrinos, resulting in a much lower $E_T^e$, on average, than the $e^\pm$ that decay directly from the $W$. As a result, the $W \to \tau\nu$ contributions are largest at low $E_T^e$, and are rather small compared the the $W \to e\nu$ yield at the maximum of the Jacobian peak ($E_T^e \sim 40$ GeV).

The $W \to \tau\nu$ background contributions were estimated using the simulation samples described in detail in Sec. 3.3. One important correction applied to the $W \to \tau\nu$ simulation sample is due to the assumptions made about $\tau$ decay in the default PYTHIA event generator that was used. The default PYTHIA generator assumes unpolarized $\tau \to e + \nu_e + \nu_\tau$ decays (*i.e.,* the $\tau$ is assumed to decay isotropically). When the $\tau$ is produced polarized in a $W$ decay however, this underestimates the $W \to \tau + \nu$ background by a factor of $1.5 \pm 0.15$ for both the $W^+$ and $W^-$ signals. The Michel spectrum [105] of the $\tau$ decay was used to determine this correction factor. A toy model for the Michel decay was developed to allow us to generate decay $E_T^e$ distributions twice, once assuming fully polarized $\tau$ decays and another assuming unpolarized $\tau$ decays. The ratio of the number of $e^\pm$'s with $E_T^e > 25$ GeV for fully polarized and unpolarized $\tau$ decays is the value of the correction factor. The uncertainties in this correction factor of 1.5 were determined by varying the $E_T^e$ cut and parameters of the Michel decay spectrum. The background contributions from $W \to \tau\nu$, including the enhancement factor of 1.5 discussed above, is shown in Fig. 5.1 along with the raw $W$ candidate yields for comparison. Table 5.1 lists each of the background processes discussed here and its estimated contribution to the $W$ yield for candidates with $E_T^e > 25$ GeV. The uncertainties on the $W \to \tau\nu$ background component are due to the statistical uncertainty of the MC calculation

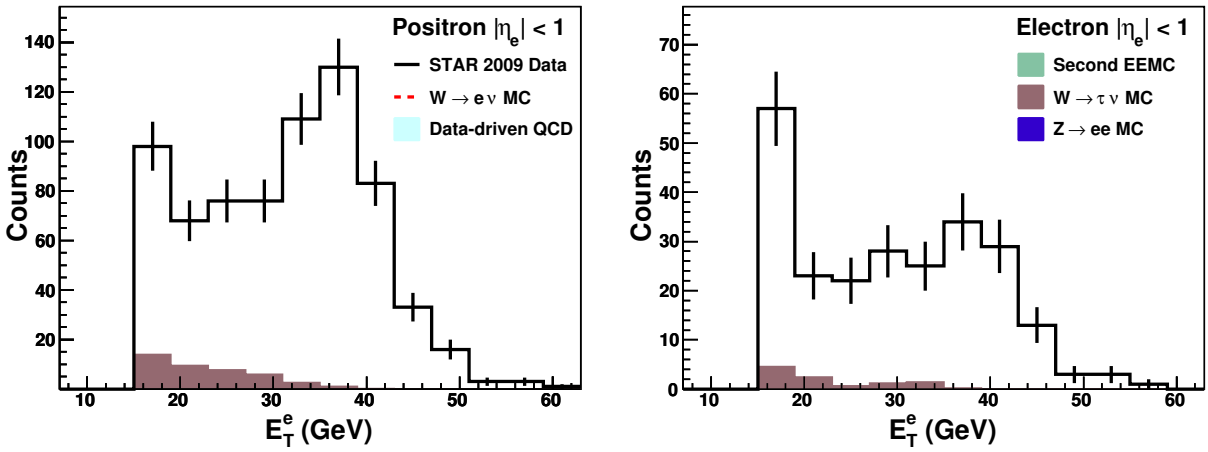


Figure 5.1: $W \to \tau\nu$ background contributions (brown), corrected for polarization effects, plotted along with the raw $W$ candidate yields for comparison ($W^+$ on the left and $W^-$ on the right).

and the systematic uncertainty of the normalization of the MC sample to the integrated luminosity of the data (related to the uncertainty in the luminosity measurement), as well as the correction factor for polarized $\tau$ decay discussed above.

### 5.1.2 $Z \to e^+e^-$ Background

$Z \to e^+e^-$ events are also a significant background to the $W \to e\nu$ signal, due to the fact that one of the decay $e^\pm$ sometimes escapes detection. This may occur from either a detector inefficiency or an $e^\pm$ traversing an uninstrumented region of phase space. When one of the decay $e^\pm$ is undetected, the other $e^\pm$ of the pair is likely to pass all of the $W$ candidate analysis cuts, as well as the signed $p_T$-balance cut, as the event topology would be indistinguishable from a $W \to e\nu$ event. The contamination from this background channel was estimated using the $Z/\gamma^* \to e^+e^-$ simulation sample described in Sec. 3.3.

Figure 5.2 shows the contribution from this background along with the raw $W$ candidate yields. Unlike the other background sources, the $Z \to e^+e^-$ background yield is approximately constant as a function of $E_T^e$. This results in a significant contribution to the $W$ yield

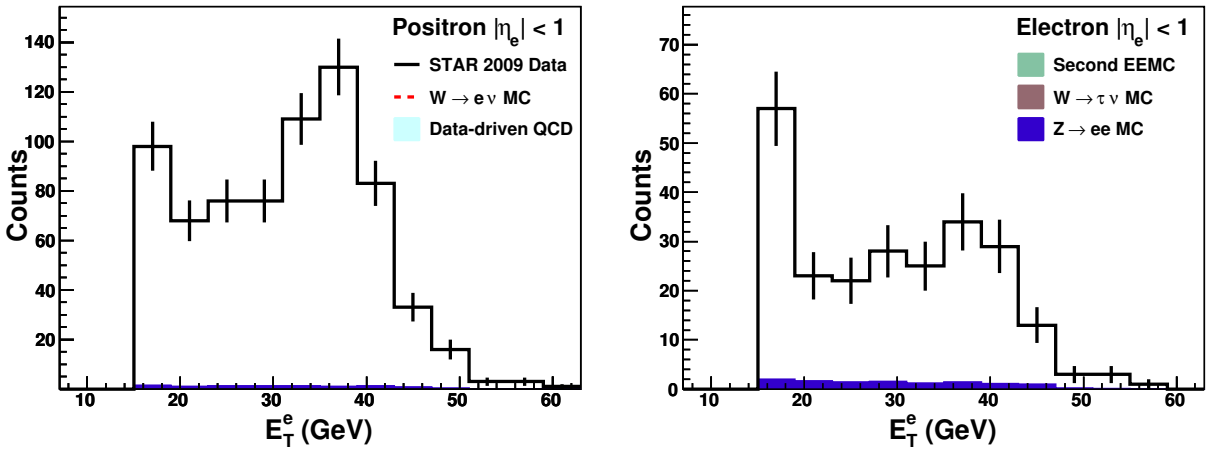


Figure 5.2: $Z/\gamma^* \to e^+e^-$ background contribution (blue) plotted along with the raw $W$ candidate yield for comparison ($W^+$ on the left and $W^-$ on the right).

at relatively large $E_T^e$, even though the $Z$ production cross section is small compared to that of the other background processes. The uncertainties on the $Z \to e^+e^-$ background component are again due to the statistical uncertainty of the MC calculation, and the systematic uncertainty of the normalization of the MC sample to the integrated luminosity of the data.

### 5.1.3 Second EEMC Background

The EEMC provides full azimuthal calorimetry coverage for a pseudorapidity of $1.09 < \eta < 2$ and helps to reject QCD background events in which the jet opposite in $\phi$ from the $e^\pm$ candidate deposits a significant amount of energy in the EEMC towers. There is, however, no EEMC on the East side (negative pseudorapidity portion) of STAR. Thus, any background $e^\pm$ candidate that has an opposite-side jet in the range $-2 < \eta < -1.09$ would satisfy the $W \to e\nu$ signal requirements, because the opposite-side jet would escape detection. This also impacts the isolation requirements, as our EEMC towers are included in the isolation cone sum of $\Delta R < 0.7$ around an $e^\pm$ candidate. If this isolation cone overlaps with this missing negative pseudorapidity acceptance, QCD background events may satisfy the $W \to e\nu$ signal requirements as well.

This contamination of the $W$ yield, resulting from the missing acceptance of the fictitious second EEMC, is referred to as the 'second EEMC' background. The magnitude of this background contribution was estimated by repeating the $W$ signal selection process, but with the EEMC towers excluded from the isolation ratio, $E_T^e/E_T^{\Delta R<0.7}$, and from the reconstruction of jets summed in the $\vec{p}_T^{\,bal}$ vector. The difference in the $E_T^e$ distributions between this analysis pass without the EEMC and the nominal signal selection is a direct measure of the background rejected by the EEMC, and is assumed to be the same as the background distribution that would have been rejected by a second EEMC.

The sample of second EEMC background events is expected to be predominantly the result of QCD processes, but it does contain a small amount of $Z \to e^+e^-$ contamination from events where one of the $e^\pm$ is in the BEMC while the other is in the EEMC. Since the background from the $Z \to e^+e^-$ process was already taken into account separately in Sec. 5.1.2, the $Z \to e^+e^-$ MC sample was used to remove any contamination from $Z \to e^+e^-$ processes in the second EEMC background distribution. The uncertainty on the second EEMC background is the statistical uncertainty of the events vetoed by the EEMC and the systematic uncertainty in the normalization of $Z \to e^+e^-$ contamination which was subtracted using the $Z \to e^+e^-$ MC (similar to the electroweak normalization systematic in Sec. 5.1.2).

### 5.1.4 Data-driven QCD Background

After the backgrounds discussed in the previous three sections are subtracted from the raw $W$ candidate yield, the remaining background is attributed to QCD $2 \to 2$ processes in which a jet fragments in such a way that it satisfies the isolated $e^\pm$ candidate requirements, while all other jets escape detection outside the $|\eta| < 2$ acceptance. This component of the background was estimated by determining a data-driven QCD background distribution as a function of $E_T^e$ (*i.e.,* a data-driven QCD background "shape"). In order to obtain this background shape, a sample of events was selected with an isolated $e^\pm$ candidate that

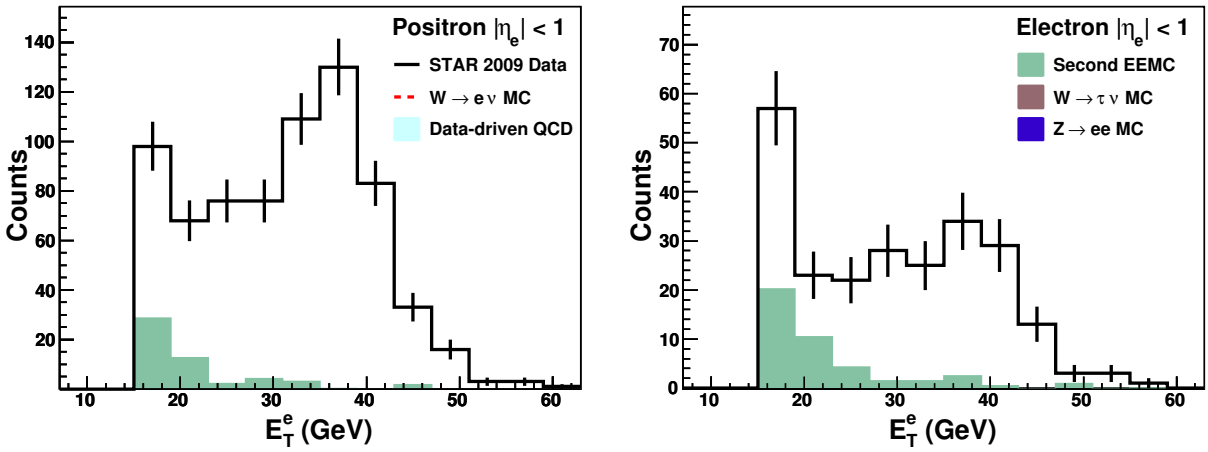


Figure 5.3: Second EEMC background contribution (green) plotted along with the raw $W$ candidate yield for comparison ($W^+$ on the left and $W^-$ on the right).

satisfied all the conditions described in Sec. 4.2, but which failed the signed $P_T$-balance cut described in Sec. 4.3.1. This sample is dominated by QCD multi-jet background events where one jet imitates an $e^{\pm}$, but the event is rejected due to the reconstructed jet opposite in azimuth. The sample should also contain some $Z \to e^+e^-$ events which have already been accounted for in Sec. 5.1.2; thus to avoid double counting the $Z$ background, the majority of $Z$ candidate events are vetoed from this background shape distribution by the method described in Sec. 5.1.5 below. Any remaining contamination of the data-driven background distribution from $Z \to e^+e^-$ events was removed using the $Z \to e^+e^-$ MC sample, similar to what was done for the second EEMC in the previous section.

The data-driven QCD background shape (in $E_T^e$) must then be normalized to the remaining $W$ yield to account for the final background contribution. To accomplish this, the background distributions discussed in the previous three sections were subtracted from the raw $W$ candidate yield, producing an intermediate background-subtracted distribution to which the data-driven QCD background shape can be normalized.

Ideally the normalization of the data-driven QCD background would be done in a region of $E_T^e$ where there are no $W \to e\nu$ signal events present, so the background shape would

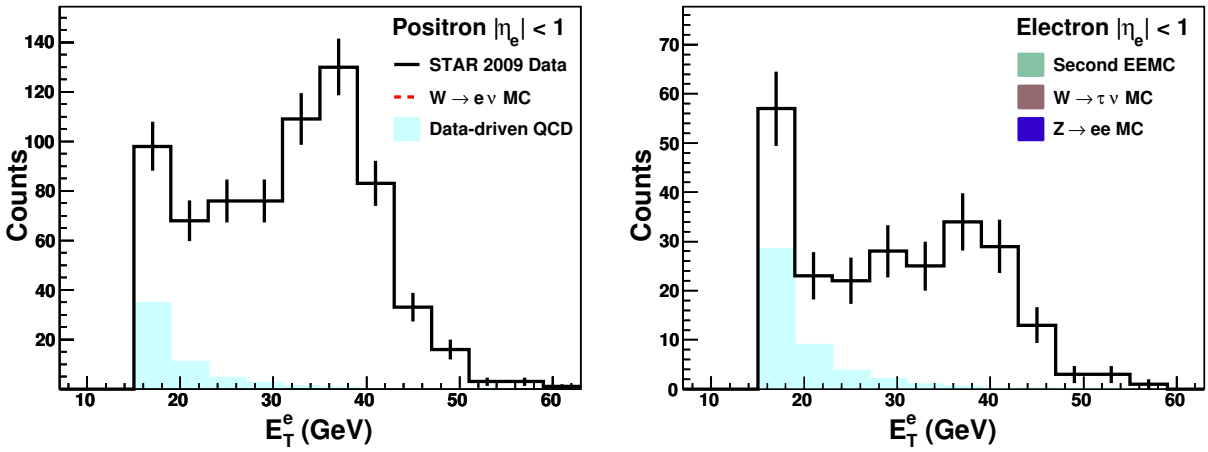


Figure 5.4: Normalized data-driven QCD background shape contributions (light blue) plotted along with the raw $W$ candidate yields ($W^+$ on the left and $W^-$ on the right).

be normalized to pure background. At low $E_T^e$, the $W$ yield is dominated by background, however due to the trigger threshold being set at $E_T \sim 13$ GeV, there are still a small number of $W \to e\nu$ signal events in the distribution, even at the lowest $E_T^e$ accessible in this analysis. Therefore, the normalization of the data-driven QCD background shape to this intermediate background-subtracted distribution was done over the range $15 < E_T^e < 19$ GeV, where the QCD background is most dominant. The $W \to e\nu$ signal MC simulation was used to estimate the number of true $W \to e\nu$ signal events in this region. The scale of the data-driven QCD background was then set such that the sum of the normalized data-driven QCD background yield and the $W \to e\nu$ signal events in this region equaled the intermediate background-subtracted distribution in the $E_T^e$ normalization range. The resulting normalized data-driven QCD background shape is shown in Fig. 5.4 along with the $W$ candidate yield.

In order to determine the systematic uncertainty of this data-driven QCD background procedure, the threshold for the signed-$P_T$-balance cut used to generate the background shape was varied from 5 to 25 GeV/$c$ in steps of 1 GeV/$c$, and the $E_T^e$ range used to normalize the shape was varied using $E_T$ = [15,17], [15,19], and [15,21] GeV. By independently varying the background shape and the normalization range, sixty different normalized background

distributions were generated. The systematic uncertainty in each $E_T^e$ bin was taken to be the largest deviation among these sixty distributions from the nominal value.

### 5.1.5 $Z \to e^+e^-$ Events in the QCD Background Distribution

The signed $P_T$-balance requirement for $W$ candidate events provides a significant suppression of QCD di-jet and $Z \to e^+e^-$ background in the event selection process. However, because the data-driven QCD background distribution is determined by inverting the signed $P_T$-balance cut, it will inevitably contain some $Z \to e^+e^-$ events as well. Since the $Z \to e^+e^-$ background contribution is already accounted for (see Sec. 5.1.2), it is beneficial to remove the identified $Z \to e^+e^-$ events from this data-driven QCD background distribution so as not to double count them. This was achieved by rejecting events that have an isolated $e^\pm$ candidate and an additional isolated $e$-like 2×2 cluster in a reconstructed jet, where $E_T^{2\times2} > p_T^{jet}/2$ and the invariant mass of the two $e^\pm$-like clusters was within the range of 70 to 140 GeV/$c^2$. This selection criteria is "looser" than the $Z$ signal reconstruction because the *two* track requirement is somewhat inefficient, and the goal of this veto is to remove as many $Z \to e^+e^-$ events from the data-driven QCD background shape as possible.

### 5.1.6 Summary of Background Contributions to the $W$ signal

Table 5.1 summarizes the background yield contributions from each of the sections above for $E_T^e > 25$ GeV and $|\eta_e| < 1$. The dominant systematic uncertainties for the $W \to \tau\nu$ and $Z \to e^+e^-$ yields are perfectly correlated as they are the result of the uncertainty in the integrated luminosity measurement. Therefore, they are added linearly to obtain the uncertainty on the total background.

| Source | $W^+$ | $W^-$ |
|---|---|---|
| $W \to \tau\nu$ | $13.4 \pm 1.7 \pm 3.2$ | $3.3 \pm 0.8 \pm 0.8$ |
| $Z \to e^+e^-$ | $7.3 \pm 0.4 \pm 1.7$ | $7.3 \pm 0.4 \pm 1.7$ |
| Second EEMC | $9.1 \pm 3.0 \pm 0.5$ | $9.2 \pm 3.0 \pm 0.4$ |
| Data-driven QCD | $7.0 \pm 0.6\ ^{+2.3}_{-1.6}$ | $5.8 \pm 0.5\ ^{+2.6}_{-1.2}$ |
| Total | $36.6 \pm 3.5\ ^{+5.4}_{-5.2}$ | $25.8 \pm 3.2\ ^{+3.6}_{-2.8}$ |

Table 5.1: Summary of background yield contributions to the $W$ signals with $E_T^e > 25$ GeV and $|\eta_e| < 1$.

## 5.2 Background Estimation for $Z$ Signal

The background for the $Z \to e^+e^-$ signal is expected to be small due to the coincidence requirement of a pair of oppositely charged, high-$E_T$ $e^+$ and $e^-$ which both satisfy the selection cuts described in Sec. 4.2. The contributions from other electroweak processes were estimated using the embedding samples described in Sec. 3.3 and noting the number of candidates that satisfied all the $Z$ signal requirements within the defined mass window ($70 < m_{e^+e^-} < 110$ GeV/$c^2$) for each sample. The background contribution was determined to be $0.1\ ^{+0.3}_{-0.1}$ events from $W \to e\nu$, and negligible from the other $Z$ decay channels. The $W \to e\nu$ background uncertainty was estimated using the 68% C.L. interval of the unified statistical approach described in Ref. [106].

An accurate data-driven estimate of the QCD background was difficult to obtain for the $Z$ signal due to the limited statistics of the data set. One method for estimating the background is to determine the number of $e^\pm$ pairs that satisfy all the $Z \to e^+e^-$ signal criteria other than the opposite charge-sign requirement. However, no same charge-sign pairs satisfying all requirements were observed in the data, as seen in Fig. 5.5. Therefore, the QCD background was found to be consistent with zero. An upper bound on the QCD background systematic uncertainty was estimated to be 1.3 events, using a 68% C.L. interval [106].

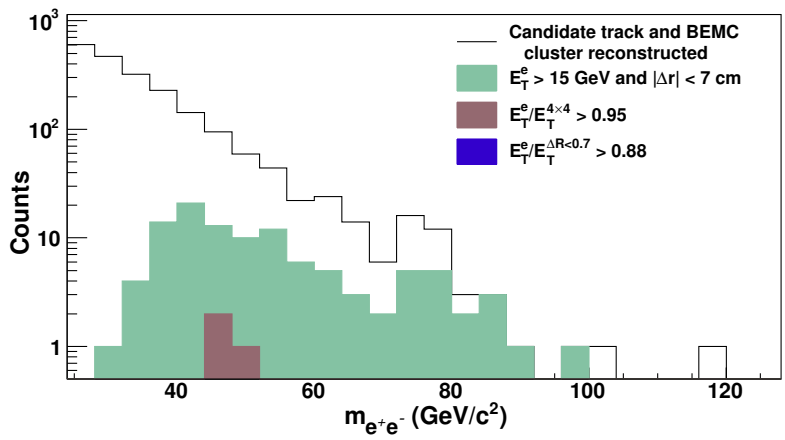


Figure 5.5: Reconstructed invariant mass of same charge-sign lepton pairs after applying various cuts, as described in Sec. 4.2.

## 5.3 Comparison of Data and Simulation

After understanding the different background components and estimating their contributions to the signal yields, it is useful to compare the yields from the data and simulation samples to assure that there is satisfactory agreement. This is important for two reasons. First, it confirms that the background estimation does a reasonable job reproducing the expected shapes of the distributions in $E_T^e$. Also, the verification of good data to simulation agreement is essential in order to confirm the validity of using the simulation samples to estimate the reconstruction efficiencies (Sec. 6.1) for both the $W \to e\nu$ and $Z/\gamma^* \to e^+e^-$ signals, which is necessary for the cross section measurement. The charge-separated $E_T^e$ distributions of $W^\pm \to e^\pm + \nu_e$ candidates satisfying all the selection criteria described in Secs. 4.2 and 4.3 are shown in Fig. 5.6 for $|\eta_e| < 1$. Also shown here are the contributions from the different backgrounds discussed in this chapter, along with the $W \to e\nu$ signal MC distribution, which is normalized to the integrated luminosity of the data. The sum of the background contributions and the $W \to e\nu$ MC signal (red dashed line) $E_T^e$ spectra agrees nicely with the $W$ candidate distribution from the data.

The $W$ yield is also displayed in Fig. 5.7, though now as a function of $e^\pm$ pseudorapidity for candidates with $E_T^e > 25$ GeV. The background contributions were estimated indepen-

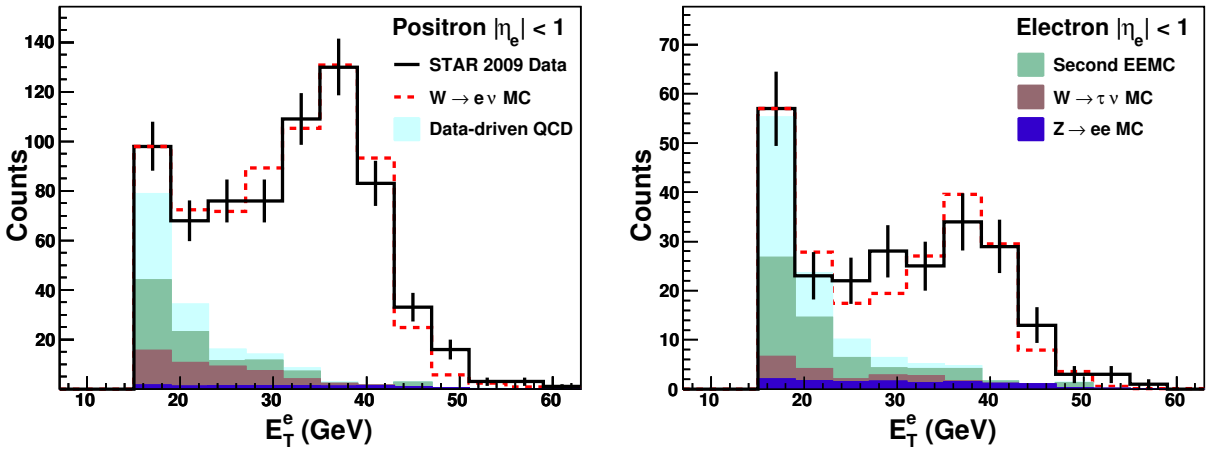


Figure 5.6: $E_T^e$ distribution of $W^+$ (left) and $W^-$ (right) candidate events, background components, and $W \to e\nu$ MC signal for comparison. Note the factor of two difference in the vertical scales. The various background contributions and $W \to e\nu$ MC signal are "stacked" on top of each other for comparison to the data.

dently for each $|\eta_e|$ bin using the methods described in the previous sections. Again, good agreement is found between the data distributions and the sum of the $W \to e\nu$ signal MC and background components. In both Figs. 5.6 and 5.7 the $W \to e\nu$ signal MC sample is normalized to the integrated luminosity of the data.

Finally, Fig. 4.13 shows the comparison of the $Z/\gamma^* \to e^+e^-$ yield as a function of $e^+e^-$ invariant mass for the $Z/\gamma^* \to e^+e^-$ signal MC and the data. The simulation sample is normalized to the integrated luminosity of the dataset and is seen to be in reasonable agreement with the data distribution near the $Z$ pole, as well as for lower mass Drell-Yan pairs.

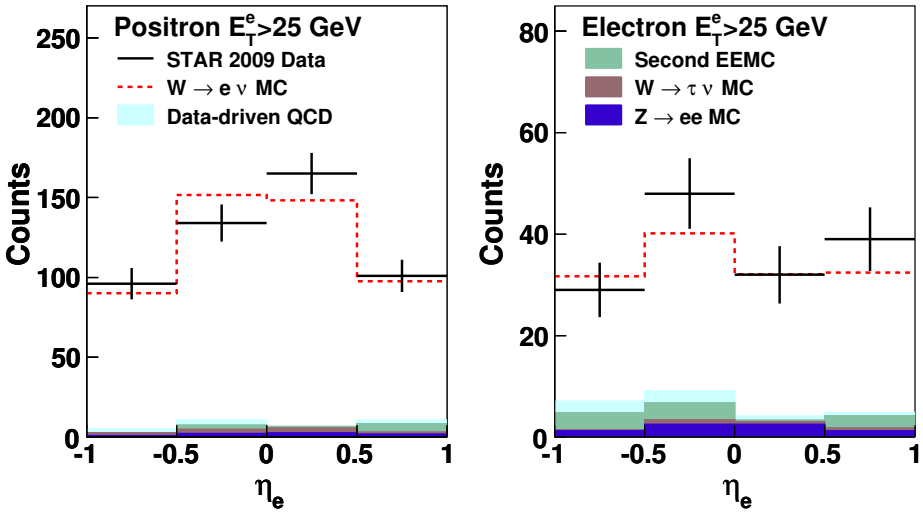


Figure 5.7: Lepton pseudorapidity distribution of $W^+$ (left) and $W^-$ (right) candidate events, background components, and $W \to e\nu$ MC signal for comparison. The various background contributions and $W \to e\nu$ MC signal are "stacked" on top of each other for comparison to the data.

# Chapter 6

# Cross Section Analysis

$W$ and $Z$ boson production cross sections were measured using the samples of candidate events that satisfied the event selection criteria described in Ch. 4. These event samples were further refined for the cross section measurement by requiring they satisfy additional fiducial and kinematic conditions. The fiducial condition was simply a geometric constraint on the $e^{\pm}$ candidates, requiring that they have $|\eta_e| < 1$. The kinematic condition was that candidates for the $W$ analysis must have $E_T^e > 25$ GeV, which restricts the sample to regions where the background contributions are small, thereby reducing sensitivity to the uncertainty in the background estimation. For the $Z$ analysis, both the $e^+$ and $e^-$ were required to have $E_T^e > 15$ GeV and $70 < m_{e^+e^-} < 110$ GeV/$c^2$. The condition on $m_{e^+e^-}$ limits the $Z/\gamma^*$ cross section measurement to a region of phase space where it is dominated by the $Z$ resonance, and thus not strongly effected by the virtual photon ($\gamma^*$) interference.

The cross sections times branching ratios measured within these constraints are defined as the fiducial cross sections, and can be written as:

$$\sigma_W^{fid} \cdot \mathrm{BR}(W \to e\nu) = \frac{N_W^{obs} - N_W^{bkgd}}{L \cdot \epsilon_W^{tot}} \tag{6.1}$$

$$\sigma_Z^{fid} \cdot \mathrm{BR}(Z \to ee) = \frac{N_Z^{obs} - N_Z^{bkgd}}{L \cdot \epsilon_Z^{tot}} \tag{6.2}$$

where

- $N^{obs}_{W(Z)}$ is the number of observed $W(Z)$ candidates within the defined kinematic acceptance that satisfied all the selection criteria described in Ch. 4,
- $N^{bkgd}_{W(Z)}$ is the total number of $W(Z)$ background events within the defined kinematic acceptance that satisfied all the selection criteria described in Ch. 4; these were estimated from various contributions as described in Ch. 5,
- $\epsilon^{tot}_{W(Z)}$ is the total efficiency correction described in Sec. 6.1 below,
- $L$ is the integrated luminosity of the data set, discussed in Sec. 3.2.

To determine the *total* production cross sections times branching ratios, it is necessary to apply acceptance correction factors, $A_{W(Z)}$, to the fiducial cross sections defined above, to account for the fiducial and kinematic constraints imposed in the analysis. The total production cross sections are then defined via the relations

$$\sigma^{tot}_W \cdot \mathrm{BR}(W \to e\nu) = \frac{\sigma^{fid}_W \cdot \mathrm{BR}(W \to e\nu)}{A_W} \tag{6.3}$$

$$\sigma^{tot}_Z \cdot \mathrm{BR}(Z \to e^+e^-) = \frac{\sigma^{fid}_Z \cdot \mathrm{BR}(Z \to e^+e^-)}{A_Z}. \tag{6.4}$$

The determination of these acceptance corrections, which are needed to extract the total production cross sections, is discussed in Sec. 6.2.

## 6.1 Efficiency Corrections

The efficiency correction factors are the measures of how efficiently $W \to e\nu$ and $Z \to e^+e^-$ decays, falling within the defined acceptance requirements, are reconstructed in the event selection process. Ideally, the efficiency correction factors would be determined from an independent sample of high $E_T$ $e^\pm$ candidates from the data. However, there is simply no such sample in the current data set that can be used to measure the efficiencies. Therefore, the efficiency corrections were obtained using the $W \to e\nu$ and $Z \to e^+e^-$ PYTHIA MC samples described in Sec. 3.3. These MC samples are suitable for estimating the efficiency corrections as they contain significant pileup contributions. The samples were generated by embedding PYTHIA MC events in zerobias data events which simulate the pileup effects known to be in the data sample.

### 6.1.1 $W$ Efficiency Correction Factors

The total efficiency correction is factorized into four conditional efficiency terms described in this section: trigger, vertex finding, tracking, and algorithm efficiency, *i.e,*

$$\epsilon_W^{tot} = \epsilon_W^{trig} \cdot \epsilon_W^{vert} \cdot \epsilon_W^{trk} \cdot \epsilon_W^{algo}. \tag{6.5}$$

Only the subset of events from the MC samples which satisfy the acceptance conditions for the fiducial cross section ($E_T^e < 25$ GeV and $|\eta_e| < 1$) were used in the efficiency calculations, as the acceptance correction is accounted for separately in the definition of the total cross section.

#### *W* Trigger Efficiency

The $W$ trigger efficiency, $\epsilon_W^{trig}$, is the fraction of $W \to e\nu$ MC events which satisfy the trigger condition defined in Sec. 3.1. This trigger condition was emulated in the MC by imposing both the level-0 single high tower requirement, $E_T > 7.3$ GeV, and the level-2 software

trigger requirement on the simulated response of the BEMC towers. The trigger efficiency is shown in Figs. 6.1 and 6.2 for $W^+$ and $W^-$, respectively. The individual distributions are shown as functions of physical $\eta_e$ (a), detector $\eta_e$ (b), $E_T^e$(c), and $\phi_e$ modulo 12 degrees (d), where physical $\eta_e$ is the pseudorapidity defined from the reconstructed primary vertex, while detector $\eta_e$ is the pseudorapidity defined from $z_{\text{vertex}} = 0$. There are several interesting features of these trigger efficiency distributions, which should be discussed here briefly.

First, there is a notably lower trigger efficiency in Figs. 6.1 a) and 6.2 a) as physical $|\eta_e|$ approaches 1. However, when comparing to the detector $\eta_e$ distributions in Figs. 6.1 b) and 6.2 b), there is no similar decrease in trigger efficiency as detector $|\eta_e|$ approaches 1. Therefore, the decrease in efficiency in this region is not due to a real inefficiency for candidates to satisfy the trigger condition when an $e^{\pm}$ deposits its energy in the BEMC towers, but instead implies that some fraction of the candidates simply don't traverse the BEMC at all. While a fiducial requirement on the physical $\eta_e$ has been applied in the definition of the trigger efficiency, there is a rather wide $z_{\text{vertex}}$ distribution in our data sample, which makes physical $\eta_e$ significantly different from the detector $\eta_e$ for a sizable fraction of the events, *i.e,* those with $|z_{\text{vertex}}|$ far from $z = 0$. Thus, some $e^{\pm}$ candidates will satisfy the fiducial requirement that physical $|\eta_e| < 1$, while having a detector $|\eta_e| > 1$, and therefore will not satisfy the trigger requirement because no energy is deposited in the BEMC towers.

The $E_T^e$ dependence of the trigger efficiency is relatively constant for the $W^+$ sample, which is naively expected as the kinematic threshold of 25 GeV is well above the trigger threshold of 13 GeV for the 2×2 cluster of BEMC tower $E_T$. The $W^-$ trigger efficiency, however, has a significant slope in $E_T^e$. The lower efficiency at smaller $E_T^e$ is a result of the $\eta_e$ dependence of the $W^-$ yield. Figure 6.3 shows the detector $\eta_e$ distributions for four $E_T^e$ bins. The larger yield as detector $|\eta_e|$ approaches one for the lower $E_T^e$ bins results in a larger fraction of events satisfying the particle $|\eta_e| < 1$ requirement, while falling outside the detector acceptance due to a displaced $z_{\text{vertex}}$ as described above. The results

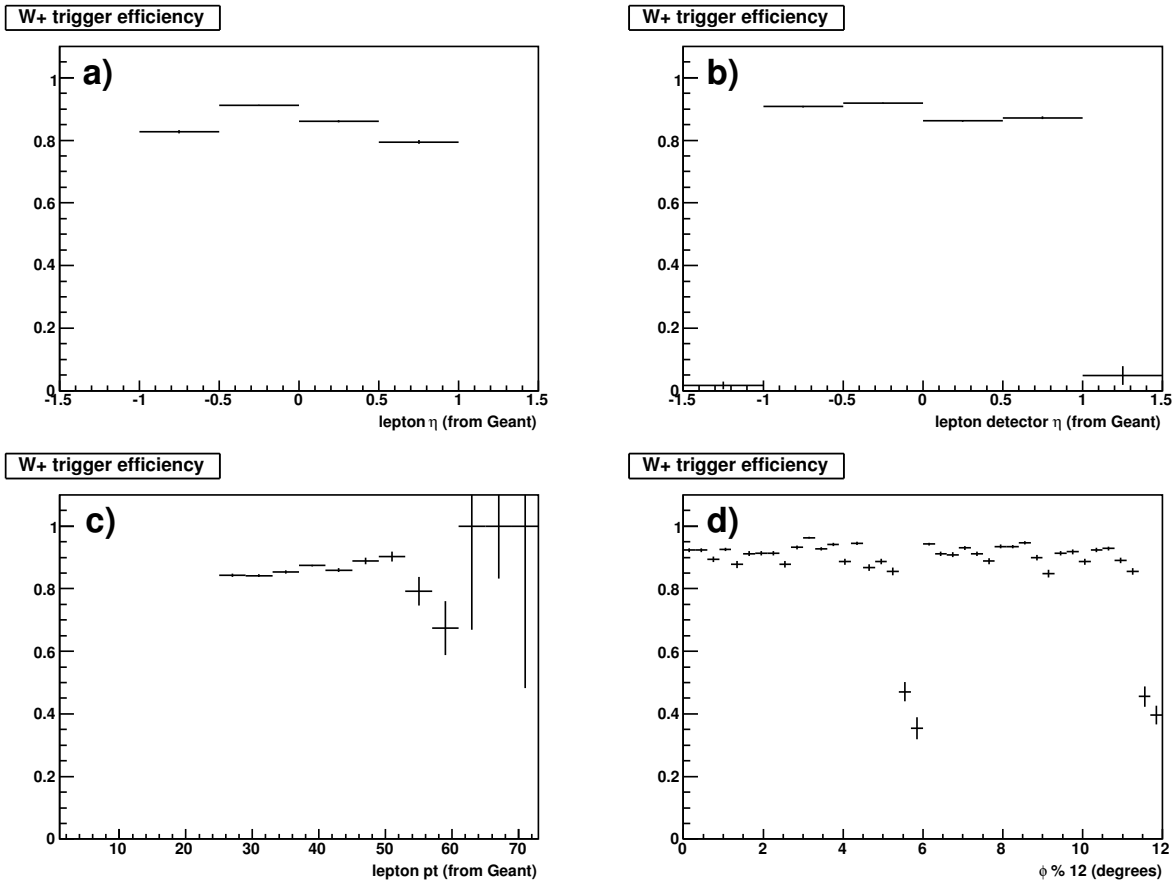


Figure 6.1: $W^+$ trigger efficiency as a function of physical $\eta_e$ (a), detector $\eta_e$ (b), $E_T^e$(c), and $\phi_e$ modulo 12 degrees (d).

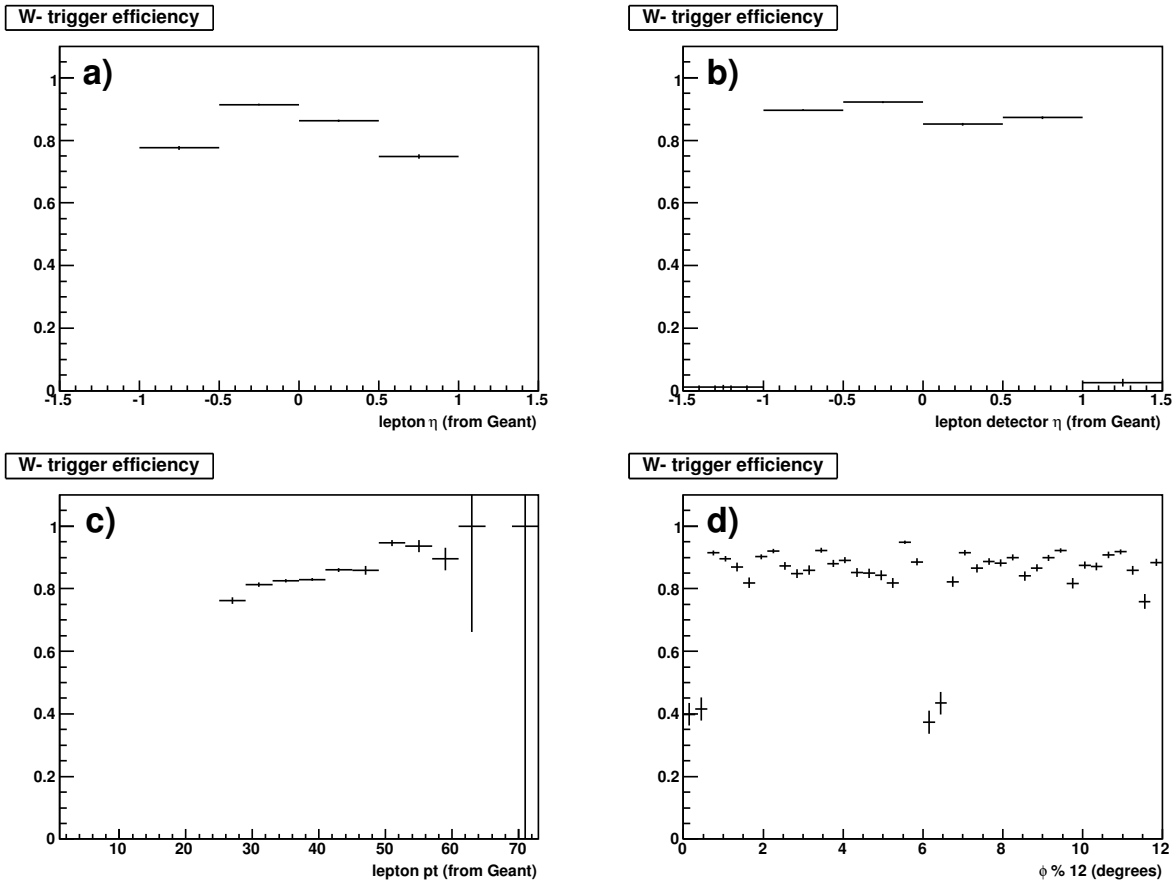


Figure 6.2: $W^-$ trigger efficiency as a function of physical $\eta_e$ (a), detector $\eta_e$ (b), $E_T^e$(c), and $\phi_e$ modulo 12 degrees (d).

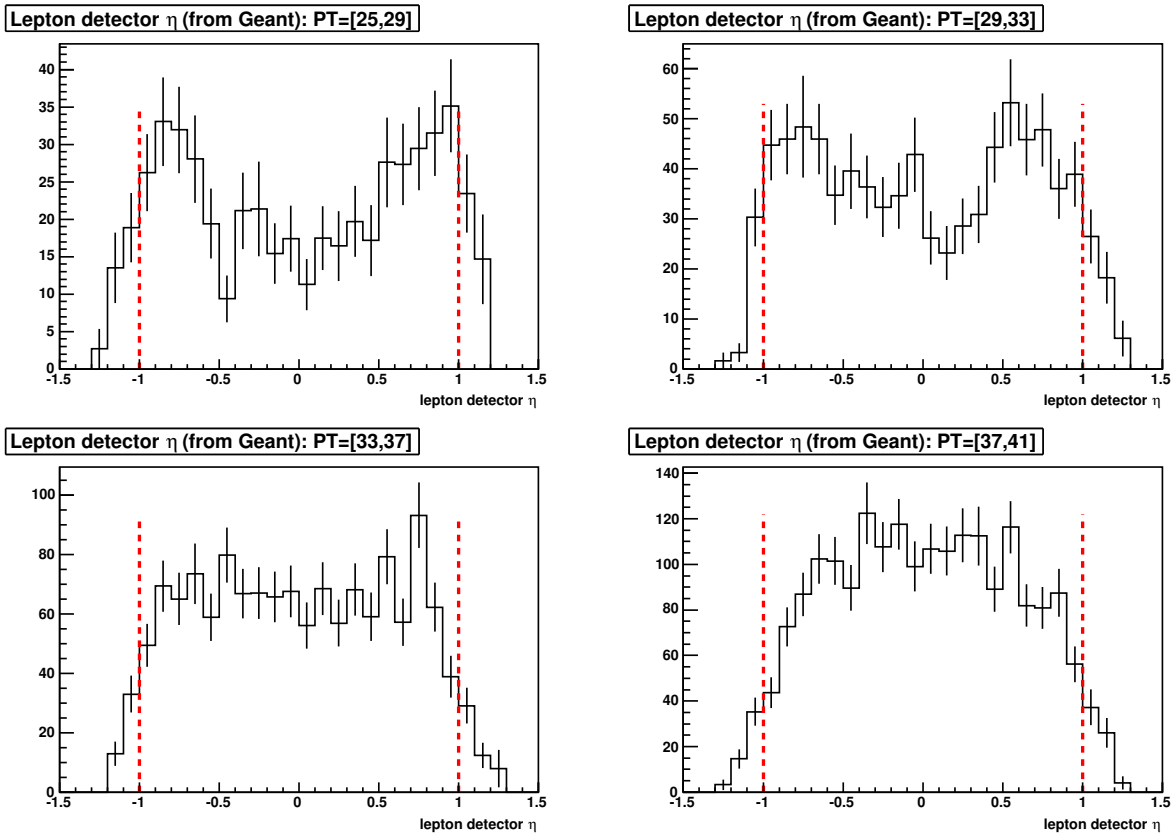


Figure 6.3: Detector $\eta_e$ distribution of $e^-$ tracks from the $W^-$ MC sample for four bins in $E_T^e$.

shown in Table 6.1 indicates that the increasing trigger efficiency with $E_T^e$ corresponds to the increasing fraction of events with detector $|\eta_e| < 1$.

Each BEMC module is 6 degrees wide in $\phi$, thus to see the effects of the module boundaries, the efficiency is binned in $\phi_e\%12$ degrees. Figures 6.1 d) and 6.2 d) show the trigger efficiency as a function of $\phi_e$ modulo 12 degrees (*i.e,* $\phi\%12$). The gaps between the module boundaries at $\phi\%12 = 6$ and 12 (0) clearly introduce some efficiency losses for $e^+(e^-)$ candidates escaping between modules.

The average $W$ trigger efficiencies were determined to be 0.857 ± 0.005 (stat) ± 0.004 (syst) and 0.825 ± 0.006 (stat) ± 0.004 (syst) for $W^+$ and $W^-$, respectively. The systematic uncertainty in the trigger efficiency was estimated by varying the BEMC tower gains by their scale uncertainty of 3.6% and then calculating the associated variation in the trigger

| | $W$ Trigger Efficiency value ± (stat) | | Fraction of events with detector $\lvert\eta_e\rvert < 1$ | |
|---|---|---|---|---|
| | $W^+$ | $W^-$ | $W^+$ | $W^-$ |
| 25< $E_T$ <29 | 0.843 ± 0.005 | 0.762 ± 0.011 | 0.948 | 0.862 |
| 29< $E_T$ <33 | 0.842 ± 0.005 | 0.814 ± 0.007 | 0.962 | 0.901 |
| 33< $E_T$ <37 | 0.853 ± 0.004 | 0.825 ± 0.005 | 0.962 | 0.932 |
| 37< $E_T$ <41 | 0.874 ± 0.003 | 0.829 ± 0.004 | 0.970 | 0.940 |
| 41< $E_T$ <45 | 0.860 ± 0.006 | 0.860 ± 0.006 | 0.951 | 0.974 |
| 45< $E_T$ <49 | 0.889 ± 0.010 | 0.859 ± 0.014 | 0.971 | 0.979 |
| $E_T$ >49 | 0.850 ± 0.039 | 0.921 ± 0.043 | 0.925 | 0.968 |

Table 6.1: $W$ trigger efficiency for different $E_T^e$ bins

efficiency. As mentioned before, the kinematic requirement on $E_T^e$ results in all candidates being well above threshold, therefore the effect of varying the BEMC tower gains is small, as expected. Due to the changing trigger efficiency as a function of $E_T^e$ an $E_T^e$-dependent trigger efficiency correction was used in the computation of the $W$ cross sections.

### *W* Vertex Finding Efficiency

The $W$ vertex finding efficiency, $\epsilon_W^{vert}$, is defined as the fraction of triggered $W \to e\nu$ MC events which contain a reconstructed primary vertex rank $> 0$ and $|z_{\text{vertex}}| < 100$ cm, as described in Sec. 4.1. As indicated in Eq. 6.5, the total efficiency is factorized into four individual terms of the $W$ candidate reconstruction, therefore, the vertex finding efficiency is determined using only the sample of events which satisfied the simulated trigger condition described in Sec. 3.1. To assure that the reconstructed vertex matches the simulated vertex position of the PYTHIA event, the reconstructed vertex is also required to be within 5 cm of the simulated PYTHIA event vertex. The average vertex finding efficiencies were 0.881 ± 0.005 and 0.886 ± 0.006 for $W^+$ and $W^-$, respectively. Figures 6.4 and 6.5 show the vertex efficiencies as functions of $z_{\text{vertex}}$ and the ZDC coincidence rate.

Unlike the trigger efficiency, the vertex finding efficiency does not show dependencies on quantities related to the $e^\pm$ candidate. However, as seen in Figs. 6.4 b) and 6.5 b), there is a notable decrease at the highest collision intensities (*i.e.,* ZDC coincidence rates) due

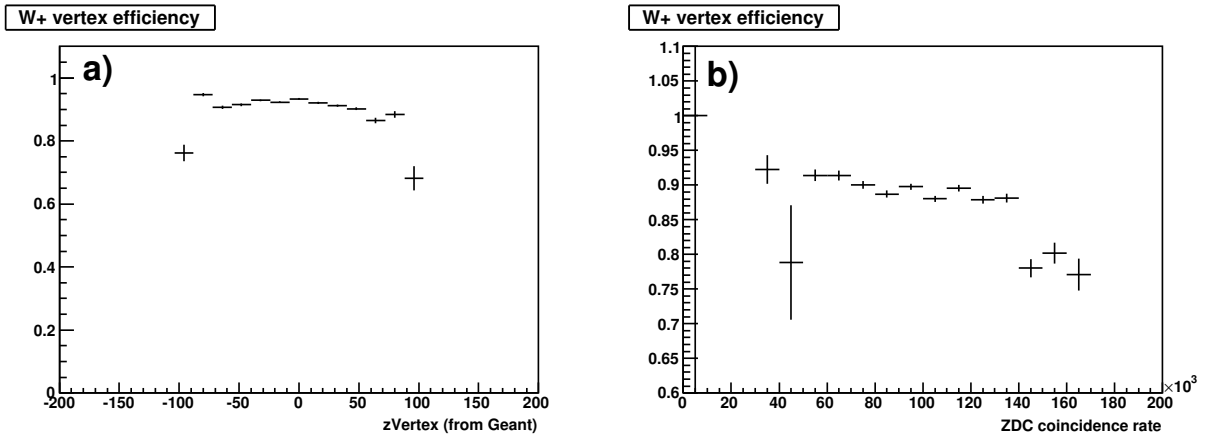


Figure 6.4: $W^+$ vertex finding efficiency as a function of $z_{\text{vertex}}$ (a) and ZDC coincidence rate (b).

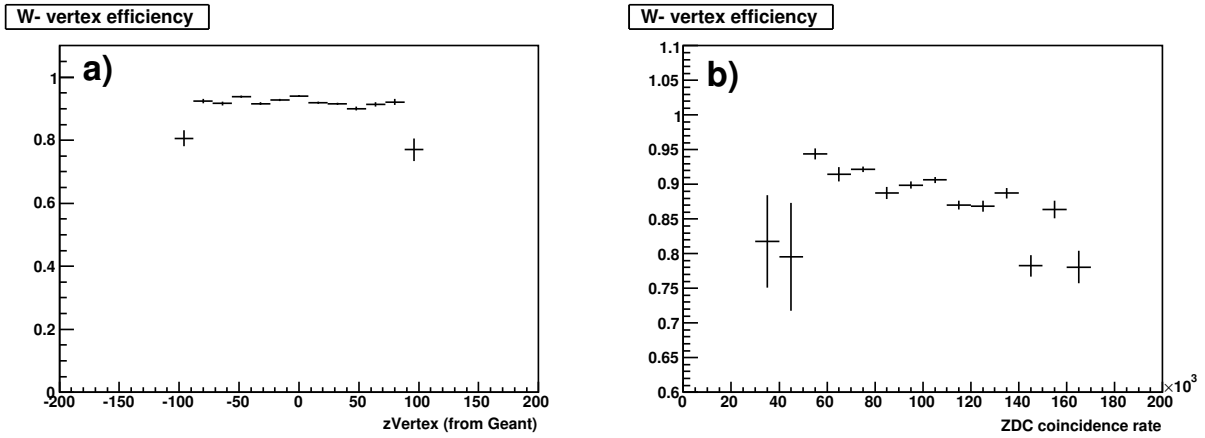


Figure 6.5: $W^-$ vertex finding efficiency as a function of $z_{\text{vertex}}$ (a) and ZDC coincidence rate (b).

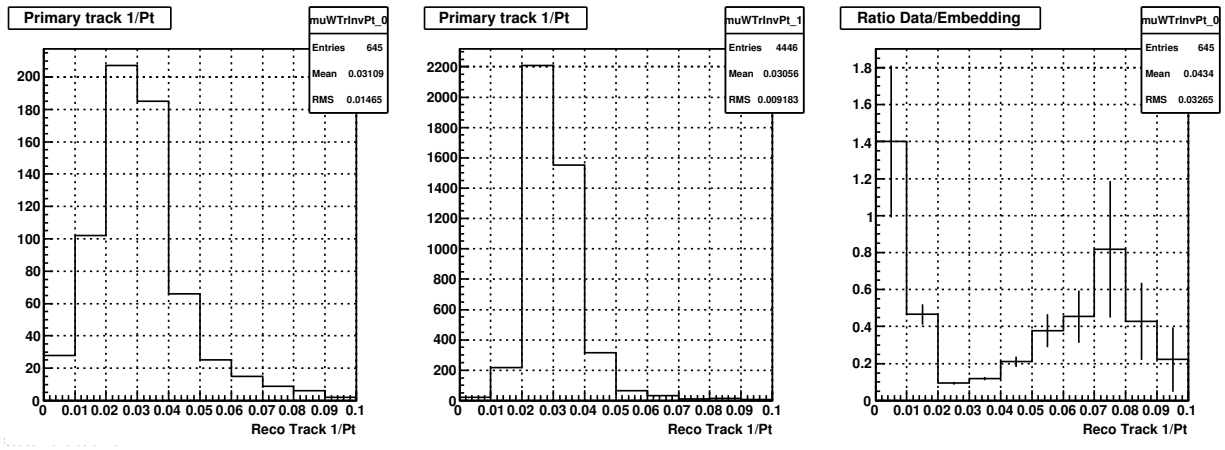


Figure 6.6: Reconstructed track $1/p_T$ distributions for $W^{\pm}$candidates satisfying all $W$ signal requirements with $E_T^e > 25$ GeV for the data and simulation samples, displayed in the left and middle plots, respectively. The right plot shows the ratio of data to simulation distributions.

to the underlying zerobias events in which the $W \to e\nu$ PYTHIA events were embedded. At these high collision intensities the TPC pileup effects are increased, producing many more tracks which are not associated with the triggered vertex of interest. This makes vertex reconstruction more difficult due to the larger number of tracks which can be incorrectly identified as originating from the primary vertex. Because the majority of the data in this analysis was recorded at lower collision intensities, this decrease does not have a significant impact on this work. However, the anticipated higher statistics samples to be collected over the next several years will use increasingly larger collision intensities, and this effect will need to be considered.

### *W* Tracking Efficiency

The $W$ tracking efficiency, $\epsilon_W^{trk}$, is determined only from the sample of $W \to e\nu$ MC events which satisfy the simulated trigger condition and also have a valid reconstructed primary vertex, as described in Sec. 4.1. It is defined as the fraction of these events which contain a reconstructed track with $p_T > 10$ GeV/$c$ that also satisfy the track quality requirements described in Sec. 4.2.1.

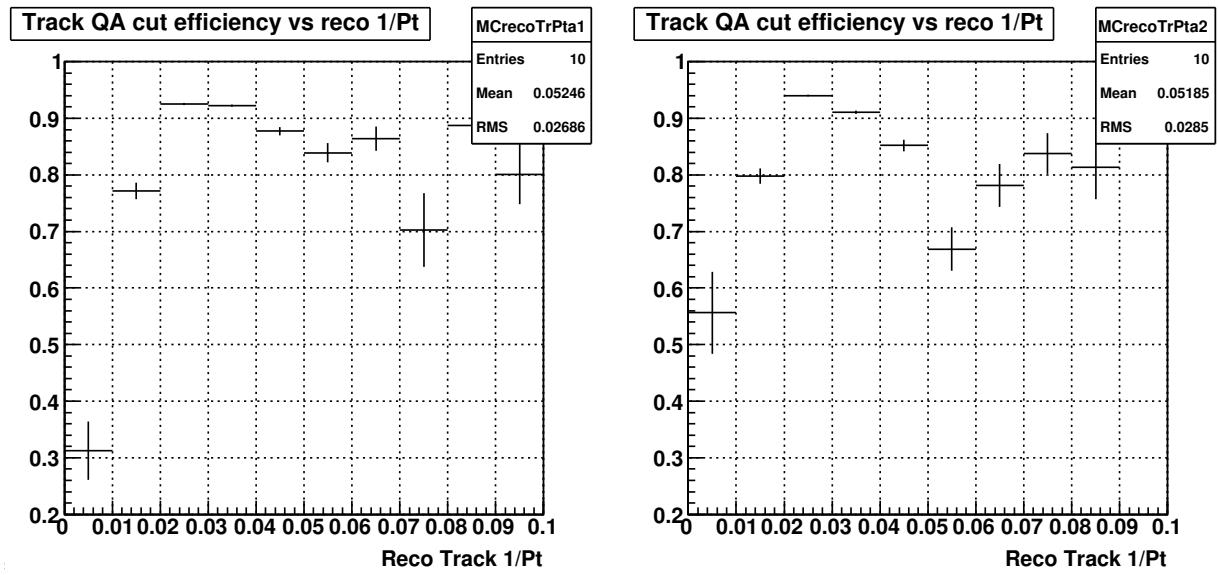


Figure 6.7: Track quality cut efficiency vs reconstructed track $1/p_T$ for $W^+$ (left) and $W^-$ (right).

Most of the tracking variables (number of TPC points, ratio of TPC points used to points possible, etc.) show good agreement between reconstructed $W$s in the data and the simulation samples. However, the distribution of reconstructed track $p_T$ is noticeably wider in the data than in simulation, representing a spatial reconstruction resolution in the data which is worse than in the simulation sample. This is shown in Fig. 6.6, which presents the reconstructed track $1/p_T$ distributions for events which satisfy all of the $W$ candidate selection requirements (with $E_T^e > 25$ GeV) in the data (left), simulation (middle), and ratio of data to simulation (right). The tails of the distribution are seen to be more populated in the data than the simulation. Figure 6.7 shows the efficiency (determined from the simulation) for a reconstructed track to satisfy the track quality requirements as a function of reconstructed track $1/p_T$. The lower efficiencies seen in the tails of the $1/p_T$ distributions are expected, as tracks with incorrectly reconstructed $p_T$ are also more likely to be lower in quality. However, because the $1/p_T$ distributions in the data and simulations don't agree in shape, the simulation alone does not correctly account for these lower efficiency regions. In order to correct for this effect, the average track quality cut efficiency was calculated

once with the nominal simulation sample, and then again after re-weighting it by the $1/p_T$ distribution of the data. Table 6.2 shows that this re-weighting reduces the track quality cut efficiency by $\sim 4.5\%$ for $W^+$ and $W^-$ relative to the nominal simulation values. This correction from the re-weighting is then applied to the total track reconstruction efficiency to give the final average values listed in Table 6.3. The relative systematic uncertainty assigned to the tracking efficiency ($\sim 4\%$) is due to the limited statistics available to determine the re-weighting factors, and the larger uncertainties associated with the track quality cut efficiency uncertainties in the tails of the simulation $1/p_T$ distributions.

| | $W$ Track Quality Cut Efficiency | |
|---|---|---|
| | Nominal Simulations ± (stat) | Re-weighted by Data ± (stat) ± (syst) |
| $W^+$ | 0.901 ± 0.006 | 0.860 ± 0.006 ± 0.035 |
| $W^-$ | 0.902 ± 0.007 | 0.867 ± 0.007 ± 0.035 |

Table 6.2: Track quality cut efficiencies and corrections for re-weighting the simulations by the data reconstructed $1/p_T$ distribution.

| | $W$ Total Tracking Efficiency | |
|---|---|---|
| | Nominal Simulations ± (stat) | Final Average Value ± (stat) ± (syst) |
| $W^+$ | 0.776 ± 0.005 | 0.741 ± 0.005 ± 0.030 |
| $W^-$ | 0.779 ± 0.006 | 0.748 ± 0.005 ± 0.030 |

Table 6.3: Total tracking efficiencies and corrections for re-weighting the simulations by the data reconstructed $1/p_T$ distribution.

The total tracking efficiencies determined from the nominal simulations (which does not include the correction for the $1/p_T$ re-weighting discussed above) is shown in Figs. 6.8 and 6.9 as a function of the ZDC coincidence rate and $\phi_e$, the azimuthal angle of the $e^{\pm}$.

Similar to the decrease in vertex finding efficiency at high collision intensities (discussed in the previous section), the tracking efficiency also decreases with higher ZDC rate. Due to increased pileup at these higher luminosities, the number of reconstructed tracks that don't originate from the triggered vertex increases, resulting in larger distortions to the tracks of interest. This in turn, makes track reconstruction more complex, which results in a slightly lower efficiency. Again, with future higher luminosity data these effects will need to be

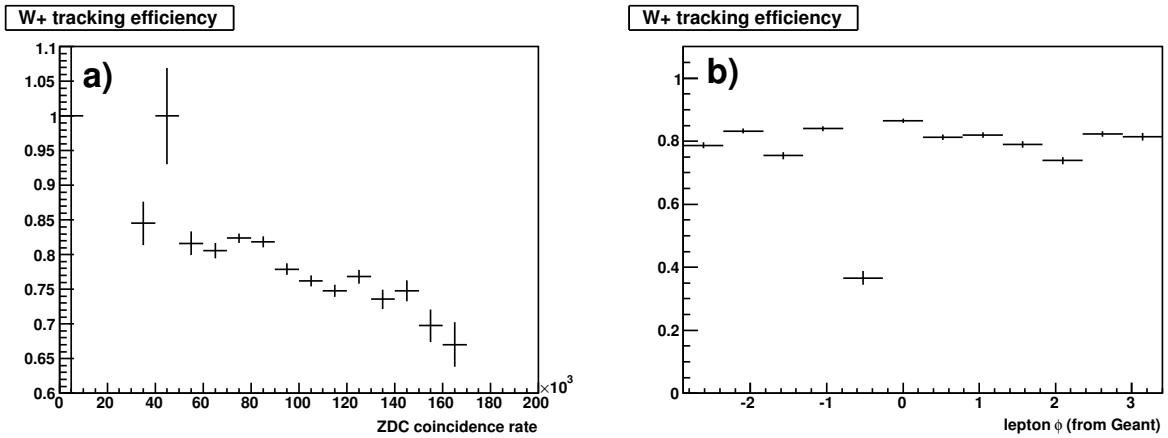


Figure 6.8: $W^+$ tracking efficiency as a function of ZDC coincidence rate (a) and $\phi_e$ (b).

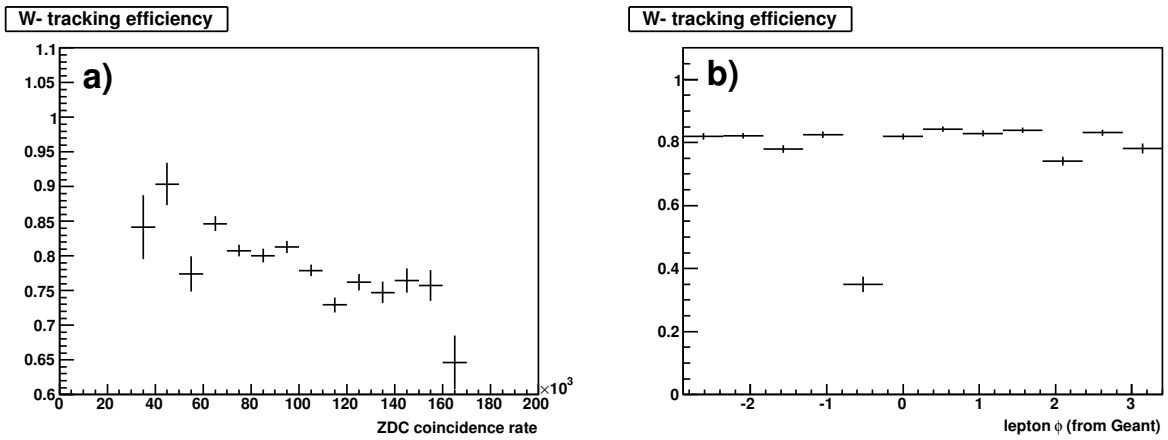


Figure 6.9: $W^-$ tracking efficiency as a function of ZDC coincidence rate (a) and $\phi_e$ (b).

further investigated.

Another interesting feature of the tracking efficiency distributions is the clear $\phi_e$ dependence. This is directly related to several TPC sectors having dead regions due to malfunctioning electronics and one sector that was removed from the analysis due to a problem in calibration. Figures 6.8 (b) and 6.9 (b) show the tracking efficiencies as a function of $\phi_e$ with each bin being the width of a single TPC sector. The TPC sectors listed in Table 6.4 contained dead regions caused by electronics problems in the data sample used for this analysis. The $\phi_e$ dependence observed in the tracking efficiency roughly matches the understood tracking problems due to these dead regions.

| TPC sector | Approx. $\phi$ (radians) | Comment |
|---|---|---|
| 4 | -0.5 | First 8 padrows dead for 73% of the data |
| 5 | -1.0 | 8 outer sector padrows dead for 42% of the data |
| 6 | -1.6 | 8 outer sector padrows dead for all of the data |
| 11 | 2.1 | First 8 padrows dead for 84% of the data |
| 20 | -0.5 | Masked out of analysis due to problems with calibration |

Table 6.4: TPC sectors with dead regions caused by electronics malfunctions.

### *W* Algorithm Efficiency

The final term in the total efficiency correction factor is the algorithm efficiency, $\epsilon_W^{algo}$. The subset of $W \to e\nu$ MC events that satisfy the trigger, have a valid reconstructed vertex, and contain a reconstructed track that satisfies the tracking requirements in section 4.2.1 are used to determine $\epsilon_W^{algo}$. This algorithm efficiency is defined to be the fraction of events that satisfy the remaining requirements in the $W$ candidate event selection described in Sec. 4.2.2, 4.2.3, and 4.3.1 which also have a reconstructed $E_T^e > 25$ GeV. The algorithm efficiency is plotted as a function of $E_T^e$ and ZDC coincidence rate in Figs. 6.10 and 6.11 for $W^+$ and $W^-$, respectively.

The interesting feature of the algorithm efficiency is its rise with $E_T^e$. The variables on which cuts are placed for each of the algorithm requirements are shown in Figs. 6.12 and 6.13 as a function of $E_T^e$ for the $W^+$ and $W^-$ simulation samples, respectively. The red lines

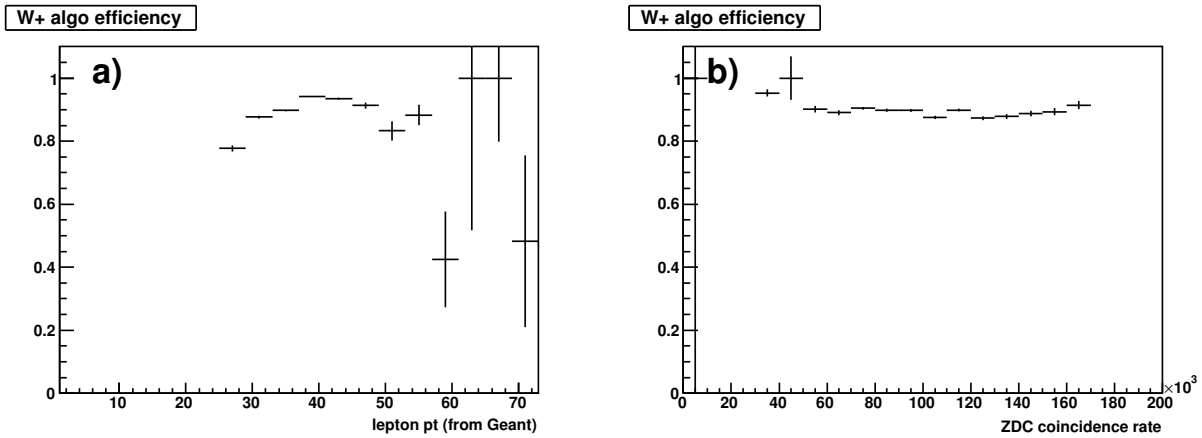


Figure 6.10: $W^+$ algorithm efficiencies as a function of $E_T^e$ and the ZDC coincidence rate.

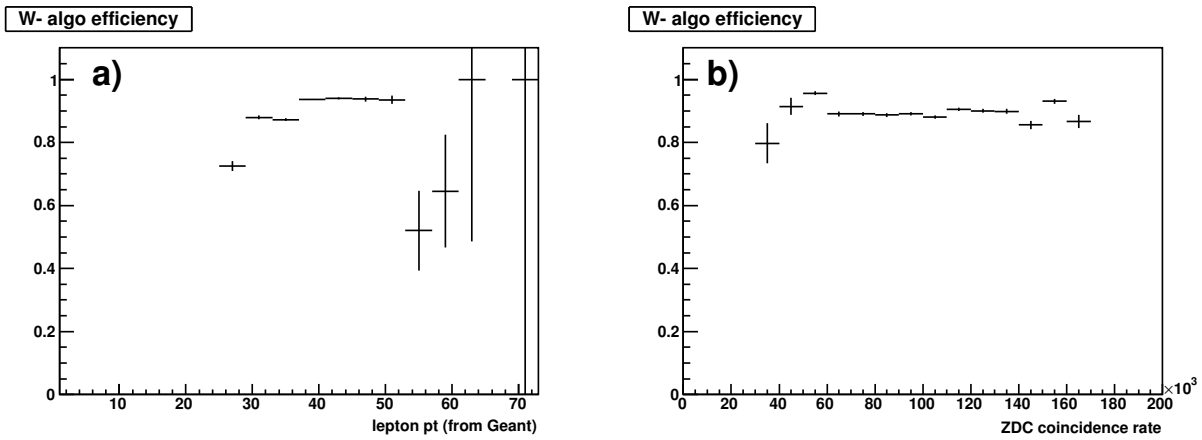


Figure 6.11: $W^-$ algorithm efficiencies as a function of $E_T^e$ and the ZDC coincidence rate.

| | $W$ Algorithm Efficiency ± (stat) | |
|---|---|---|
| | $W^+$ | $W^-$ |
| 25< $E_T$ <29 | 0.777 ± 0.009 | 0.726 ± 0.016 |
| 29< $E_T$ <33 | 0.876 ± 0.005 | 0.879 ± 0.006 |
| 33< $E_T$ <37 | 0.897 ± 0.003 | 0.873 ± 0.005 |
| 37< $E_T$ <41 | 0.942 ± 0.002 | 0.937 ± 0.002 |
| 41< $E_T$ <45 | 0.935 ± 0.004 | 0.940 ± 0.003 |
| 45< $E_T$ <49 | 0.913 ± 0.010 | 0.937 ± 0.008 |
| $E_T$ >49 | 0.796 ± 0.051 | 0.821 ± 0.063 |

Table 6.5: $W$ algorithm efficiencies for different $E_T$ bins

indicate the values where the cuts were placed. From the figures it is clear that the near-side cone cut, shown in panel c) and described in Sec. 4.2.3, is mainly responsible for the reduction in efficiency for both samples. These figures also demonstrate that the inefficiency seen at lower $E_T^e$ is expected due to the $E_T^e$ dependence of the near-side cone sum ratio $E_T^e/E_T^{\Delta R<0.7}$. The very lowest $E_T^e$ bin also has a reduced efficiency due to resolution effects in the BEMC towers, which cause some candidates to have a reconstructed $E_T^e < 25$ GeV even though the electron satisfied the kinematic acceptance cuts at the MC particle level. The $E_T^e$ dependent efficiency values (which are used in the cross section calculation) are given in Table 6.5. The average algorithm efficiencies are 0.892 ± 0.005 (stat) ± 0.023 (syst) and 0.892 ± 0.006 (stat) ± 0.023 (syst) for $W^+$ and $W^-$, respectively. The systematic uncertainty in the algorithm efficiency was determined by varying the BEMC tower gains by their scale uncertainty and calculating the variation in the algorithm efficiency. The resulting relative systematic uncertainty is estimated to be ±2.6% for both $W^+$ and $W^-$.

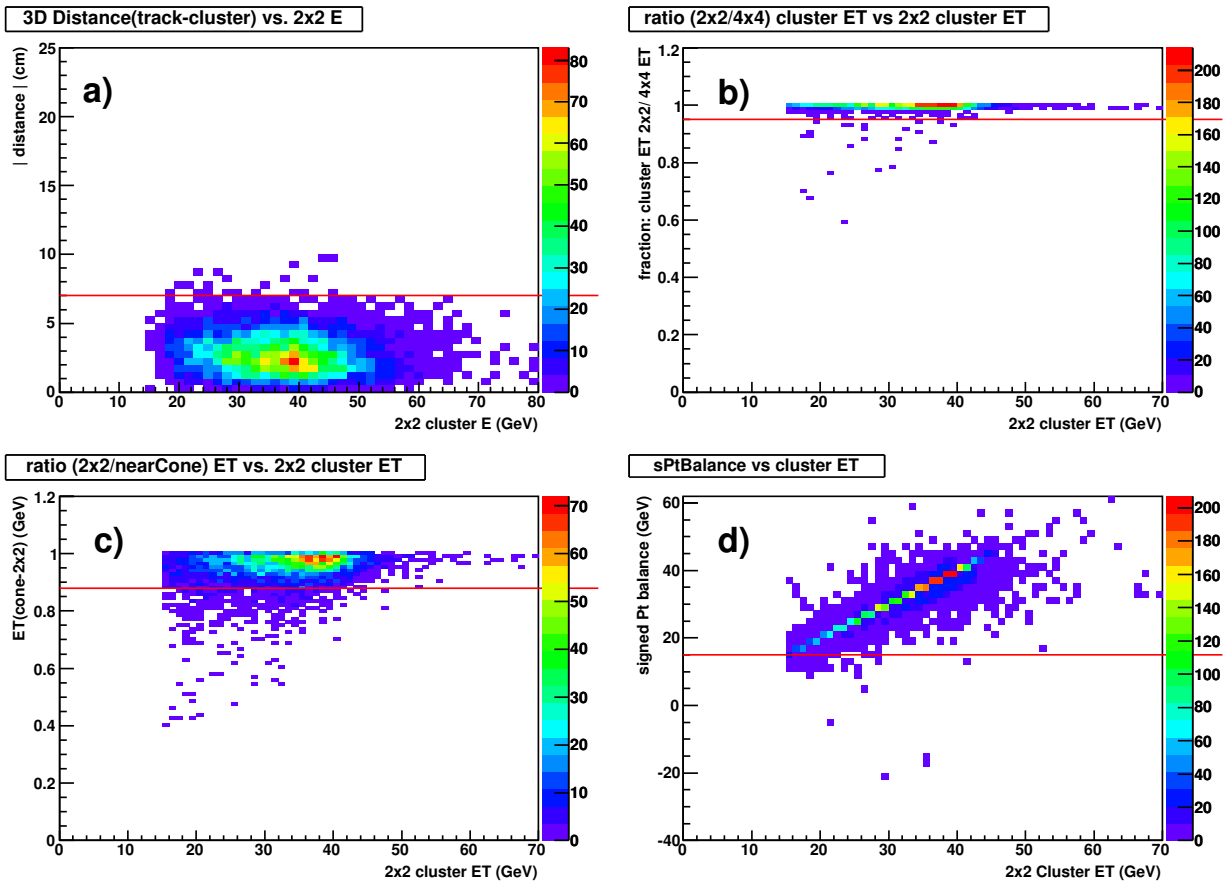


Figure 6.12: $W^+$ distributions relevant to the $W$ reconstruction algorithm cuts, each as a function of $E_T^e$. (a) 3D distance between track and tower centroid, (b) cluster ratio $E_T^e/E_T^{4\times4}$, (c) near-side cone sum ratio $E_T^e/E_T^{\Delta R<0.7}$, and (d) signed $P_T$-Balance.

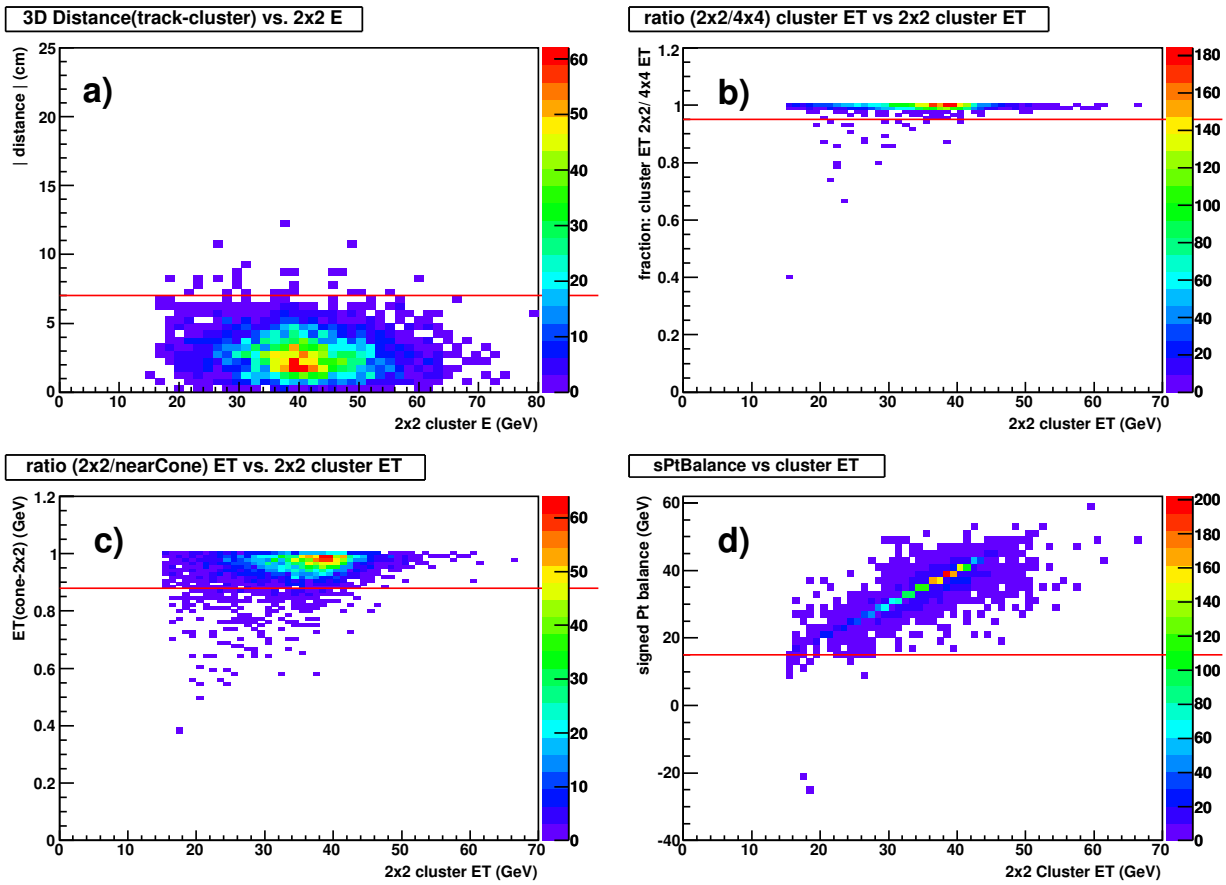


Figure 6.13: $W^-$ distributions relevant to the $W$ reconstruction algorithm cuts, each as a function of $E_T^e$. (a) 3D distance between track and tower centroid, (b) cluster ratio $E_T^e/E_T^{4\times4}$, (c) near-side cone sum ratio $E_T^e/E_T^{\Delta R<0.7}$, and (d) signed $P_T$-Balance.

### 6.1.2 $Z$ Efficiency Correction Factors

Similar to the $W$ efficiency correction, the total $Z$ efficiency correction is factorized into four conditional efficiency terms described in this section: trigger, vertex finding, tracking, and algorithm efficiency, that is

$$\epsilon_Z^{tot} = \epsilon_Z^{trig} \cdot \epsilon_Z^{vert} \cdot \epsilon_Z^{trk} \cdot \epsilon_Z^{algo}, \tag{6.6}$$

As described previously, the fiducial cross section will be measured within the kinematic acceptance of $70 < m_{e^+e^-} < 110$ GeV/$c^2$, $E_T^e > 15$ GeV, and $|\eta_e| < 1$. Therefore, each efficiency term is calculated for events that satisfy these acceptance requirements.

#### $Z$ Trigger Efficiency

The trigger efficiency for $Z \to e^+e^-$ events, $\epsilon_Z^{trig}$, is defined as the fraction of $Z \to e^+e^-$ MC events which satisfy the simulated trigger condition, similar to the $W$ trigger efficiency. In Fig. 6.14 the trigger efficiency is plotted as a function of invariant mass ($m_{e^+e^-}$) and the ZDC coincidence rate of the zerobias event in which the simulated $Z \to e^+e^-$ PYTHIA event was embedded. As expected, the $Z$ trigger efficiency is higher than that of the $W$ trigger efficiency, as there are two high-$p_T$ $e^\pm$ which can satisfy the trigger condition. Thus, even if one of the $e^\pm$ falls outside of the detector acceptance due to a displaced vertex, or traverses a BEMC tower dead region, the trigger condition may still be satisfied by the other $e^\pm$. The average $Z$ trigger efficiency was estimated to be $0.968 \pm 0.004 \pm 0.005$. The relative systematic uncertainty in the trigger efficiency was determined by varying the BEMC tower gains by their scale uncertainty and then calculating the variation in the trigger efficiency, which was found to be 0.5%.

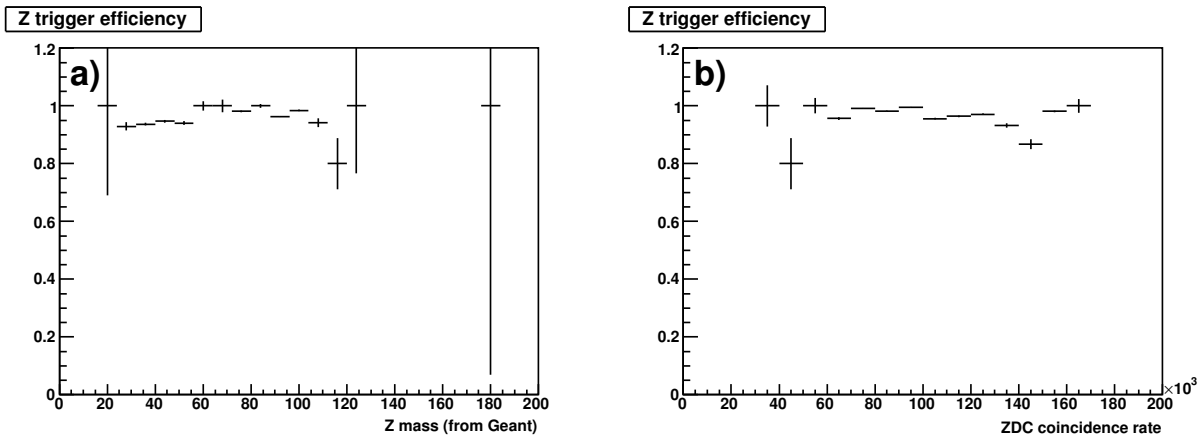


Figure 6.14: $Z$ trigger efficiency plotted as a function of $m_{e^+e^-}$ and the ZDC coincidence rate.

### $Z$ Vertex Finding Efficiency

Similar to the $W$ vertex finding efficiency, the $Z$ vertex finding efficiency, $\epsilon_Z^{vert}$, is defined as the fraction of events with a reconstructed vertex that satisfied the cuts described in 4.1, where the reconstructed vertex is required to be within 5 cm of the simulated vertex from PYTHIA. This was determined from the sample of $Z \to e^+e^-$ MC events which satisfied the simulated trigger condition, so the trigger efficiency had already been accounted for. The average value for the vertex finding efficiency is $0.938 \pm 0.006$. In Fig. 6.15 the vertex finding efficiency is plotted as a function of $m_{e^+e^-}$ and the ZDC coincidence rate. As expected, $\epsilon_Z^{vert}$ does not depend on $m_{e^+e^-}$; however, a dependence on ZDC rate is seen (similar to that of the the $W$ vertex finding efficiency) due to the same pile-up related issues. It is also worth noting that the vertex finding efficiency is larger for $Z \to e^+e^-$ events than for $W \to e\nu$, again due to the fact that there are two $e^\pm$ in the $Z \to e^+e^-$ final state, which allows a vertex to be reconstructed even if one of the two $e^\pm$ tracks is not reconstructed in the TPC.

### $Z$ Tracking Efficiency

The tracking efficiency, $\epsilon_Z^{trk}$, for the $Z \to e^+e^-$ signal is determined from the subset of $Z \to e^+e^-$ MC events which satisfy the simulated trigger condition, and have a valid reconstructed

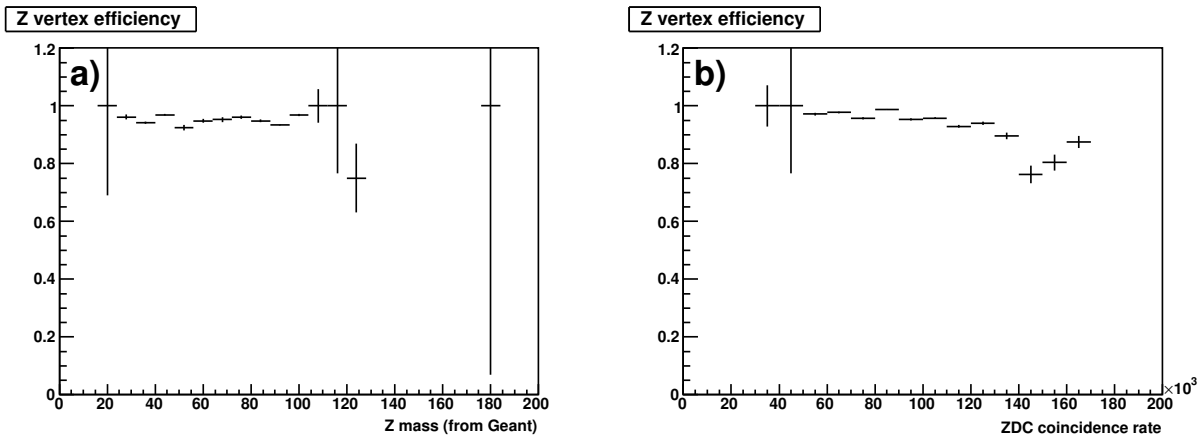


Figure 6.15: $Z$ vertex finding efficiency plotted as a function of $m_{e^+e^-}$ and the ZDC coincidence rate.

primary vertex as described in Sec. 4.1. It is defined as the fraction of events containing *two* reconstructed tracks that satisfy the track quality cuts described in Sec. 4.2.1, each having $p_T > 10$ GeV. The two-track requirement implies that the $Z$ tracking efficiency should be approximately the square root of the tracking efficiency for the $W$ sample squared. This simple assumption is approximately correct, as one can see by comparing the tracking efficiencies in Figs. 6.16 and 6.8 for $Z$ and $W^+$ events, respectively. It is important to point out that the correction to the tracking efficiency based on the $1/p_T$ normalization discussed in Sec. 6.1.1 is applied to each $e^\pm$ here to account for a lower efficiency for each track decaying from the $Z$. Finally, the decrease in tracking efficiency with ZDC rate is even more dramatic than what is seen for the $W^+$ case due to the two track requirement. The average value for the $Z$ tracking efficiency is 0.511 $\pm$ 0.013 (stat) $\pm$ 0.029 (syst), where the systematic uncertainty is found by combining the single tracking efficiency systematic from Sec. 6.1.1 in quadrature for the two tracks.

### $Z$ Algorithm Efficiency

Finally, the algorithm efficiency, $\epsilon_Z^{algo}$, is defined as the fraction of events with reconstructed $e^+$ and $e^-$ candidates, both of which satisfy all of the $Z$ candidate event conditions described in sections 4.2.2 and 4.2.3. As usual, the algorithm efficiency is determined from the subset

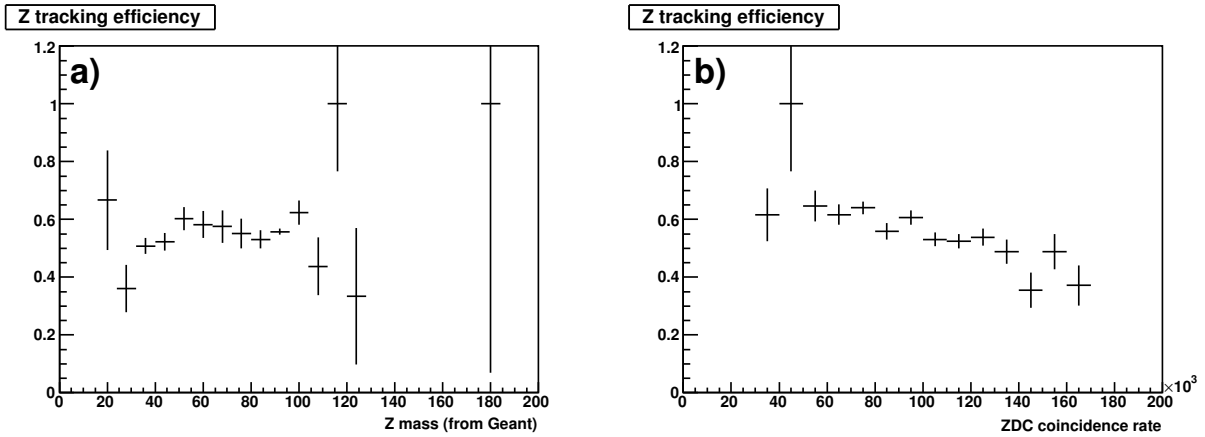


Figure 6.16: $Z$ tracking efficiency plotted as a function of $m_{e^+e^-}$ and the ZDC coincidence rate.

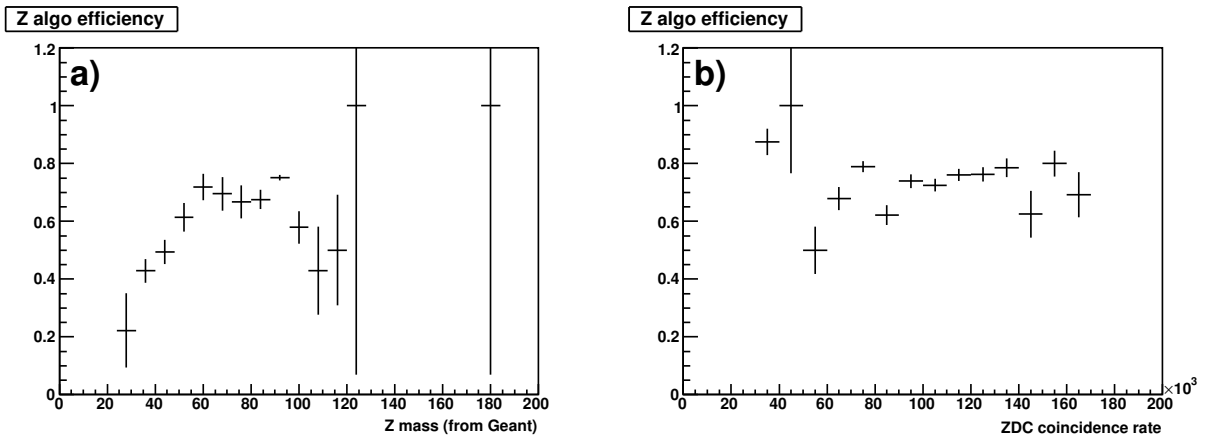


Figure 6.17: $Z$ algorithm efficiency plotted as a function of $m_{e^+e^-}$ and the ZDC coincidence rate.

of events that satisfy the trigger condition, have a valid reconstructed vertex, and have two reconstructed tracks which passed the track quality cuts. The $Z$ algorithm efficiency is plotted in Fig. 6.17; its average value is 0.730 ± 0.015 (stat) ± 0.019 (syst). The relative systematic uncertainty in the algorithm efficiency was determined by varying the BEMC tower gains by their scale uncertainty and then calculating the variation in the algorithm efficiency, which was found to be 2.6%.

## 6.2 Acceptance Corrections

In order to determine the total cross section for $W$ or $Z$ boson production, it is necessary to correct for the detector acceptance and any self-imposed kinematic acceptance requirements. As outlined at the beginning of this chapter, this is done by applying correction factors $A_W$ and $A_Z$ to the fiducial cross sections, as indicated in Eqs. 6.3 and 6.4. These acceptance correction factors were calculated using the FEWZ program [107], which provides cross section calculations for $W$ and $Z$ boson production up to next-to-next-to leading order (NNLO) in perturbative QCD. Parton distribution functions from the MSTW 2008 [1] and CTEQ 6.6 [28] groups were used as input for the cross section calculations. The use of these acceptance factors in the total cross section measurements introduces some additional theoretical uncertainties, which originate from two sources:

- Uncertainties in the proton PDFs used as input for the calculation. This was estimated by: 1) noting the difference between MSTW 2008 NLO and CTEQ 6.6 NLO PDF sets; and 2) using the PDF error eigenvector sets to determine the uncertainty within one PDF set (details discussed in section 6.4).

- Uncertainties in the modeling of the production process, estimated by comparing the acceptance values from calculations with different orders of QCD corrections, using the same PDF set (*i.e.,* comparing LO, NLO, and NNLO for MSTW 2008).

| | $A_{W^+}$ | $A_{W^-}$ | $A_Z$ |
|---|---|---|---|
| LO MSTW 2008 | 0.591 | 0.444 | 0.377 |
| NLO MSTW 2008 | 0.597 | 0.444 | 0.378 |
| NNLO MSTW 2008 | 0.603 | 0.435 | 0.385 |
| NLO CTEQ 6.6 | 0.592 | 0.430 | 0.370 |

Table 6.6: Summary of acceptance values calculated with the FEWZ program. The MSTW 2008 NLO values are used for the total cross section calculations.

A summary of the acceptance correction values is shown in Table 6.6 for different orders of the calculation and for two different PDF sets. The theoretical uncertainties for these

| | $\delta A_{W^+}/A_{W^+}$ | $\delta A_{W^-}/A_{W^-}$ | $\delta A_Z/A_Z$ |
|---|---|---|---|
| Difference between PDFs | 1.0% | 3.2% | 2.1% |
| MSTW 2008 NLO error PDFs | 0.9% | 2.7% | 1.2% |
| CTEQ 6.6 NLO error PDFs | 0.9% | 4.5% | 1.8% |
| Calculation Order | 1.0% | 2.0% | 1.9% |
| Total | 1.7% | 5.2% | 3.2% |

Table 6.7: Summary of the relative uncertainties in the acceptance correction factors, $A_W$ and $A_Z$, as computed by the FEWZ program.

acceptance factors are summarized in Table 6.7. Both the MSTW and CTEQ groups provide error eigenvector PDF sets which estimate the variation allowed in the global fit that was used to determine the distribution functions at various confidence levels. The uncertainty due to the individual PDF sets was determined using the 90% confidence level error eigenvector PDF sets, and taking the average of the individual uncertainties introduced by the MSTW 2008 NLO and CTEQ 6.6 NLO PDF sets. The uncertainty due to the variation of the order of calculation was taken to be the maximum difference from the nominal value, MSTW 2008 NLO, and the calculations at other orders using MSTW 2008. The individual contributions listed in Table 6.7 were added in quadrature to determine the total uncertainty for each acceptance factor. Interestingly, the $A_{W^-}$ uncertainties are significantly larger than those for $A_{W^+}$. This is primarily due to the PDF related errors, which is consistent with the general expectation of larger uncertainties for the $\bar{u}$ and $d$ quarks, compared to those of the $\bar{d}$ and $u$ quarks.

## 6.3 Results

### 6.3.1 $W^+$ and $W^-$ Cross Sections

The fiducial cross sections for $W^+$ and $W^-$ are defined in Eq. 6.1, and the input values and uncertainties necessary to compute them are summarized in Table 6.8.

| | $W^+$ | | | | $W^-$ | | | |
|---|---|---|---|---|---|---|---|---|
| | value | stat | syst | lumi | value | stat | syst | lumi |
| $N_W^{obs}$ | 496 | 22.3 | - | - | 148 | 12.2 | - | - |
| $N_W^{bkgd}$ | 36.6 | 3.5 | $^{+5.4}_{-5.2}$ | - | 25.8 | 3.2 | $^{+3.6}_{-2.5}$ | - |
| $\epsilon_W^{tot}$ | 0.498 | 0.006 | 0.025 | - | 0.488 | 0.007 | 0.025 | - |
| $L$ (pb$^{-1}$) | 13.2 | 0.2 | - | 1.7 | 13.2 | 0.2 | - | 1.7 |

Table 6.8: Summary of input values for the $W \to e\nu$ fiducial cross section measurement, with their statistical, systematic, and luminosity uncertainties. As noted in Sec. 6.1.1, an $E_T^e$-dependent efficiency correction factor is used for the actual cross section measurement, and only the average value is given here.

The product of the fiducial cross section and the relevant branching ratio is measured within the kinematic acceptance of $E_T^e > 25$ GeV and $|\eta_e| < 1$ for $W^+$ and $W^-$. The results are the following:

$$\sigma_{W^+}^{fid} \cdot \mathrm{BR}(W^+ \to e^+ \nu_e) = 70.0 \pm 3.5 \text{ (stat)} \pm 3.5 \text{ (syst)} \pm 9.1 \text{ (lumi) pb}$$

$$\sigma_{W^-}^{fid} \cdot \mathrm{BR}(W^- \to e^- \bar{\nu}_e) = 19.2 \pm 2.1 \text{ (stat)} \pm 1.1 \text{ (syst)} \pm 2.5 \text{ (lumi) pb}$$

The dominant uncertainty for both the $W^+$ and $W^-$ cross sections is due to the systematic uncertainty in the measured integrated luminosity of the data sample.

To obtain the total cross section, the fiducial cross section is divided by the acceptance correction factors discussed in Sec. 6.2. The results for the $pp \to W^\pm$ total production cross sections, times branching ratio, at $\sqrt{s} = 500$ GeV are the following:

$$\sigma_{W^+}^{tot} \cdot \mathrm{BR}(W^+ \to e^+ \nu_e) = 117.3 \pm 5.9 \text{ (stat)} \pm 6.2 \text{ (syst)} \pm 15.2 \text{ (lumi) pb},$$

$$\sigma_{W^-}^{tot} \cdot \mathrm{BR}(W^- \to e^- \bar{\nu}_e) = 43.3 \pm 4.6 \text{ (stat)} \pm 3.4 \text{ (syst)} \pm 5.6 \text{ (lumi) pb}.$$

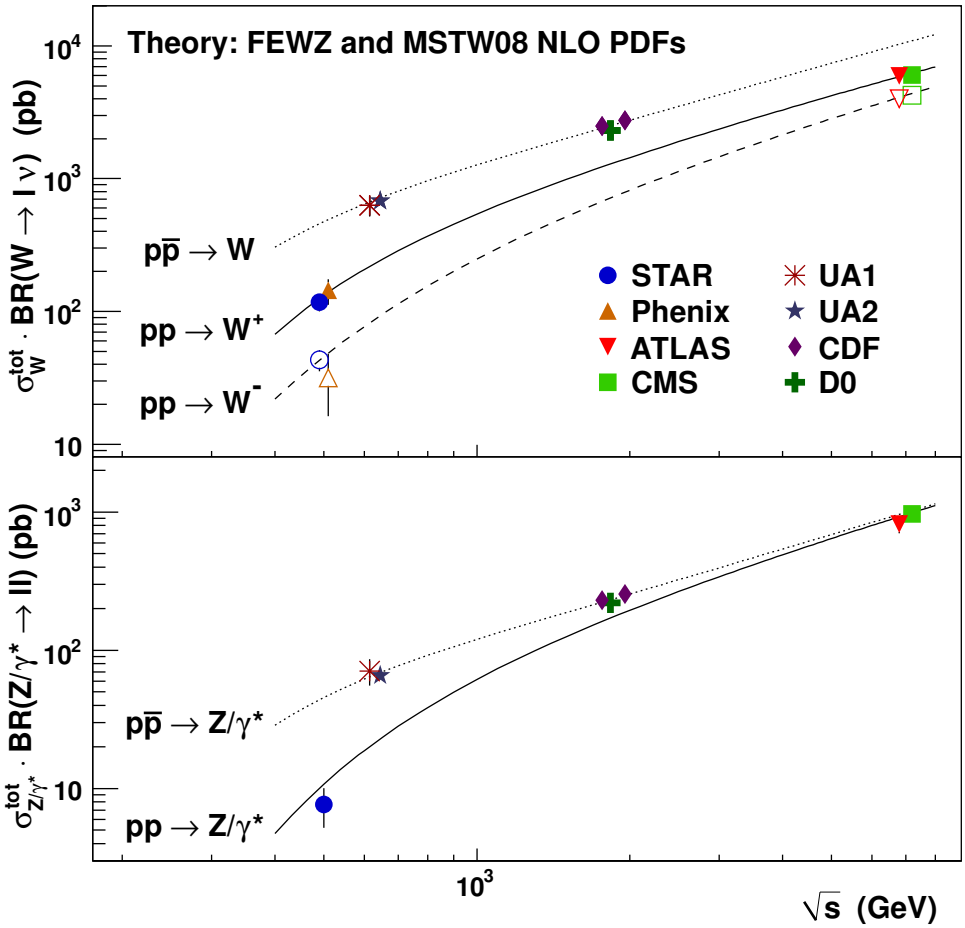


Figure 6.18: Measurements of the $W^{\pm}$ and $Z$ ($70 < m_{e^+e^-} < 110$ GeV/$c^2$) total cross section times branching ratio as a function of center-of-mass energy. For the $W^{\pm}$ cross sections in $pp$ collisions, the closed symbols represent $W^+$ and the open symbols represent $W^-$. The theory curves are from the FEWZ program at NLO using the MSTW 2008 PDF set.

The total cross sections times branching ratio are shown in Fig 6.18 as a function of center-of-mass energy, along with other measurements in both $pp$ (PHENIX [69], ATLAS [70], and CMS [71, 72]) and $p\bar{p}$ (UA1 [57, 58], UA2 [59, 60], CDF [61, 62] and D0 [63, 64]) collisions. NLO theoretical predictions provided by the FEWZ program using the MSTW 2008 PDF set are shown for comparison. A more thorough discussion of the theoretical calculations and uncertainties is presented in Sec. 6.4.

### 6.3.2 $Z/\gamma^*$ Cross Section

The fiducial cross section for $Z/\gamma^*$ is defined in Eq. 6.2, and the input relevant for calculation of the fiducial cross section is listed in Table 6.9 along with the estimated uncertainties.

| | Z | | | |
|---|---|---|---|---|
| | value | stat | syst | lumi |
| $N_Z^{obs}$ | 13 | 3.6 | - | - |
| $N_Z^{bkgd}$ | 0.1 | 0.1 | $^{+1.3}_{-0.0}$ | - |
| $\epsilon_Z^{tot}$ | 0.338 | 0.012 | 0.021 | - |
| $L$ (pb$^{-1}$) | 13.2 | 0.2 | - | 1.7 |

Table 6.9: Summary of input values for the $Z \to e^+e^-$ fiducial cross section, with their statistical, systematic, and luminosity uncertainties.

The fiducial cross section times branching ratio is measured within the kinematic acceptance of $E_T^e > 15$ GeV, $|\eta_e| < 1$, and $70 < m_{e^+e^-} < 110$ GeV/$c^2$. Our final result is the following:

$$\sigma_{Z/\gamma^*}^{fid} \cdot \mathrm{BR}(Z/\gamma^* \to e^+e^-) = 2.9 \pm 0.8 \text{ (stat)} \pm^{+0.2}_{-0.3} \text{ (syst)} \pm 0.4 \text{ (lumi) pb}$$

The $Z/\gamma^*$ cross section uncertainty is currently dominated by the low statistics of the data sample, with the next largest contribution from the systematic uncertainty in the measured integrated luminosity. The fiducial cross section is divided by the acceptance correction factors discussed in Sec. 6.2, to obtain the total cross section. Our result for the $pp \to Z/\gamma^*$ total production cross section times branching ratio at $\sqrt{s} = 500$ GeV in the invariant mass range of $70 < m_{e^+e^-} < 110$ GeV/$c^2$ is

$$\sigma_{Z/\gamma^*}^{tot} \cdot \mathrm{BR}(Z/\gamma^* \to e^+e^-) = 7.7 \pm 2.1 \text{ (stat)} \,^{+0.5}_{-0.9} \text{ (syst)} \pm 1.0 \text{ (lumi) pb.}$$

This result is included in Fig 6.18 as a function of center-of-mass energy, along with the $W^+$ and $W^-$ measurements and theoretical predictions from the FEWZ program at NLO.

### 6.3.3 $W^+/W^-$ Cross Section Ratio

The $W^+/W^-$ cross section ratio is defined within the kinematic acceptance $E_T^e > 25$ GeV and $|\eta_e| < 1$, so the acceptance correction factors used in extracting the total production cross sections in Sec. 6.3.1 are not necessary here. The cross section ratio can therefore be written as

$$R_W = \frac{\sigma_{W^+}^{fid}}{\sigma_{W^-}^{fid}} = \frac{N_{W^+}^{obs} - N_{W^+}^{bkgd}}{N_{W^-}^{obs} - N_{W^-}^{bkgd}} \cdot \frac{\epsilon_{W^-}^{tot}}{\epsilon_{W^+}^{tot}}, \tag{6.7}$$

where the integrated luminosity (and its sizable uncertainty) cancel out. This significantly reduces the systematic uncertainty of $R_W$ with respect to the $W^+$ and $W^-$ cross sections when calculated independently.

To compute $R_W$, the $W$ candidate yields, background contributions, efficiency correction factors, and uncertainties were extracted in two bins in $|\eta_e|$ following the same procedure as was used for the $\eta_e$ integrated fiducial cross section measurement described in section 6.3.1. The results are presented in Fig. 6.19, which shows the $R_W$ data points along with theory points from the FEWZ calculation for both the MSTW 2008 NLO and the CTEQ 6.6 NLO PDF sets. The uncertainties for the data points are the statistical and systematic errors added in quadrature, and the uncertainties for the theory points are from the 90% confidence level error eigenvector PDF sets described in Sec. 6.4. Table 6.10 contains numerical values for the data points and their uncertainties.

| | $R_W \pm$ (stat) $\pm$ (syst) |
|---|---|
| $\lvert\eta_e\rvert < 0.5$ | $4.3 \pm 0.7 \pm 0.3$ |
| $0.5 < \lvert\eta_e\rvert < 1.0$ | $2.9 \pm 0.5 \pm 0.2$ |

Table 6.10: Measurements of the $W$ cross section ratio, $R_W$, for the two $e^\pm$ pseudorapidity bins.

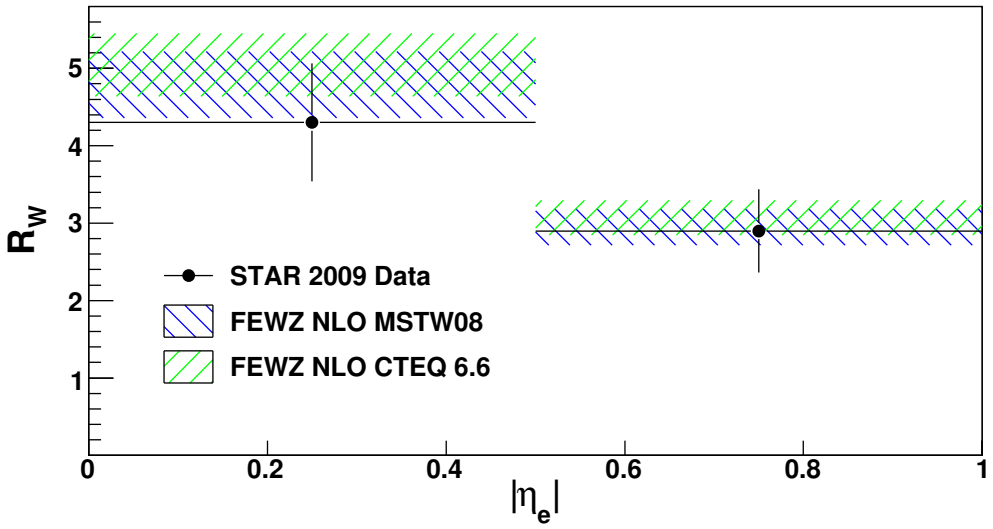


Figure 6.19: $W$ cross section ratio, $R_W$, for two $e^{\pm}$ pseudorapidity bins. Theory calculations at NLO from the FEWZ program using the MSTW 2008 and CTEQ 6.6 PDF sets (with 90% confidence level error eigenvector uncertainties) are shown for comparison.

## 6.4 Theory Calculations

This section is intended to provide a brief review of the theoretical calculations used both to estimate the acceptance corrections (section 6.2), and for comparison to our measurements. The theory code we have used most often is the FEWZ program [107]. This program provides calculations of $W$ and $Z/\gamma^*$ production cross sections that incorporate various kinematic constraints and can use a number of PDF sets, as well as working to different orders of QCD corrections in the calculation (LO, NLO, and NNLO). For additional comparison, the RHICBOS program [56], which provides a full soft-gluon resummation calculation, has been used for the $W$ cross sections as well.

The PDF sets used in these calculations are the MSTW 2008 [1] and CTEQ 6.6 [28] sets. Both of these groups use a global fit analysis to determine a PDF set which best fits the constraints of the relevant data from DIS, hadron colliders, and fixed target measurements. These fits contain 20 and 22 parameters for the MSTW 2008 and CTEQ 6.6 sets, respectively. The groups also provide what are known as "error eigenvector PDF sets," which are the distribution functions obtained by varying each parameter (up and down) at some given confidence level around the best fit value resulting in two error eigenvector sets for each fit parameter. These error eigenvector PDF sets are then used to calculate the cross sections within the allowed variation of the parameter space of the global PDF fit to determine the dependence of the calculation on these variations. The 90% confidence level error eigenvector PDFs from these two groups have been used to determine the uncertainty in the cross section calculations due to the input PDFs. A symmetric uncertainty formula, written as

$$\delta\sigma = \frac{1}{2}\sqrt{\sum_{i=1}^{d}(\sigma_i^+ - \sigma_i^-)^2} \tag{6.8}$$

was used to evaluate this uncertainty, where $\sigma_i^+$ and $\sigma_i^-$ are the cross sections calculated from the error eigenvector variation of parameter $i$, and $d$ is the number of varied parameters. The MSTW and CTEQ groups also provide error eigenvector sets corresponding to the

variation of the strong coupling constant, $\alpha_s$. These $\alpha_s$ error PDFs were considered as well, but the uncertainties were negligible compared to the PDF uncertainties. Table 6.11 lists the results of theory calculations from the FEWZ and RHICBOS programs for all the production cross sections and ratios, relevant for this work, along with their uncertainties. The error eigenvector PDF sets were not available for the RHICBOS program, therefore they were not evaluated here.

| Quantity | Theory Value |
|---|---|
| NLO MSTW 2008 $\sigma^{tot}_{W+}$ | 132.4 ± 9.0 |
| NNLO MSTW 2008 $\sigma^{tot}_{W+}$ | 136.7 ± 9.5 |
| NLO CTEQ 6.6 $\sigma^{tot}_{W+}$ | 121.8 ± 8.8 |
| RHICBOS CTEQ 6.6 $\sigma^{tot}_{W+}$ | 121.1 |
| NLO MSTW 2008 $\sigma^{tot}_{W-}$ | 45.7 ± 3.6 |
| NNLO MSTW 2008 $\sigma^{tot}_{W-}$ | 48.1 ± 3.0 |
| NLO CTEQ 6.6 $\sigma^{tot}_{W-}$ | 41.1 ± 4.3 |
| RHICBOS CTEQ 6.6 $\sigma^{tot}_{W-}$ | 39.9 |
| NLO MSTW 2008 $\sigma^{tot}_{Z/\gamma*}$ | 10.8 ± 0.8 |
| NNLO MSTW 2008 $\sigma^{tot}_{Z/\gamma*}$ | 11.2 ± 0.8 |
| NLO CTEQ 6.6 $\sigma^{tot}_{Z/\gamma*}$ | 9.8 ± 0.8 |
| NLO MSTW 2008 $\sigma_{W+}/\sigma_{W-}$ ($\lvert\eta\rvert < 0.5$) | 4.79 ± 0.44 |
| NLO CTEQ 6.6 $\sigma_{W+}/\sigma_{W-}$ ($\lvert\eta\rvert < 0.5$) | 5.04 ± 0.40 |
| NLO MSTW 2008 $\sigma_{W+}/\sigma_{W-}$ ($0.5 < \lvert\eta\rvert < 1.0$) | 2.95 ± 0.24 |
| NLO CTEQ 6.6 $\sigma_{W+}/\sigma_{W-}$ ($0.5 < \lvert\eta\rvert < 1.0$) | 3.07 ± 0.23 |

Table 6.11: Summary of FEWZ and RHICBOS cross section calculations and uncertainties at $\sqrt{s} = 500$GeV. The $Z/\gamma^*$ values are defined within the invariant mass range of $70 < m_{e^+e^-} < 110$ GeV/$c^2$.

# Chapter 7

# Spin Asymmetry Analysis

The measurement of the parity-violating longitudinal single-spin asymmetry, $A_L$, for $W$ production is a critical component of the spin program at RHIC because of its unique sensitivity to the antiquark helicity distributions (see Sec. 1.1.3). As a single-spin asymmetry, this measurement only requires alternating the helicity of one of the incoming longitudinally-polarized proton beams. However, as was discussed in Sec. 2.1, both proton beams (blue and yellow) at RHIC are polarized, resulting in four possible helicity configurations of colliding protons at the STAR detector interaction region. These four helicity configurations are labeled $++, +-, -+$, and $--$, denoting the helicity of the blue and yellow beam, respectively. The actual spin asymmetry can then be extracted using the $W^+$ and $W^-$ yield in each of these independent helicity configurations. This chapter describes the details of this asymmetry measurement from the spin-dependent yields and a comparison of the experimental results to theoretical expectations.

## 7.1 Extraction of $A_L$ from Spin Dependent Yields

As described in the introduction (Sec. 1.1.3), the longitudinal single-spin asymmetry $A_L$ is defined as:

$$A_L \equiv \frac{\sigma_+ - \sigma_-}{\sigma_+ + \sigma_-}. \tag{7.1}$$

Because both beams are polarized at RHIC, a single-spin asymmetry can be measured independently for each beam, and subsequently combined to form a final measurement using both beams. To obtain the expressions for the measurable asymmetries it is useful to write the formulas for the spin-dependent yields as a function of the longitudinal asymmetries and beam polarizations:

$$N_{++} = \sigma_0 \; L_{++} \; \epsilon_0 \; (1 \; + A_L P_1 \; + A_L P_2 \; + A_{LL} P_1 P_2 \; ) \tag{7.2}$$

$$N_{+-} = \sigma_0 \; L_{+-} \; \epsilon_0 \; (1 \; + A_L P_1 \; - A_L P_2 \; - A_{LL} P_1 P_2 \; ) \tag{7.3}$$

$$N_{-+} = \sigma_0 \; L_{-+} \; \epsilon_0 \; (1 \; - A_L P_1 \; + A_L P_2 \; - A_{LL} P_1 P_2 \; ) \tag{7.4}$$

$$N_{--} = \sigma_0 \; L_{--} \; \epsilon_0 \; (1 \; - A_L P_1 \; - A_L P_2 \; + A_{LL} P_1 P_2 \; ) \tag{7.5}$$

where $\sigma_0$ is the unpolarized cross section, $L_{\pm\pm}$ is the luminosity integrated for that particular spin state, $\epsilon_0$ is the reconstruction efficiency, $P_{1(2)}$ is the polarization of the blue (yellow) beam, and $A_L$ ($A_{LL}$) is the longitudinal single(double)-spin asymmetry. Because the asymmetries are extracted from ratios of these yields, any spin-independent factors ($\sigma_0$ and $\epsilon_0$) cancel nicely in the asymmetry calculation. The spin-dependent integrated luminosity is accounted for by applying a relative luminosity correction to the spin-dependent yields, and will be discussed in Sec. 7.4. The yields in Eqs. 7.2-7.5, of course, only represent the true $W$ signal events, and do not reflect how the backgrounds might effect the spin-dependent yields. The correction for the dilution of the $W$ candidate yield by polarized or unpolarized background is discussed in Sec. 7.5.

For this analysis five asymmetries have been defined from these four spin-dependent

yields, three of which are independent. In the simplified case where the integrated luminosity for each spin state is identical, they are given by:

$$A_L^{blue} = \frac{1}{P_1}\frac{N_{++} + N_{+-} - N_{--} - N_{-+}}{\Sigma N_i} \tag{7.6}$$

$$A_L^{yellow} = \frac{1}{P_2}\frac{N_{++} + N_{-+} - N_{--} - N_{+-}}{\Sigma N_i} \tag{7.7}$$

$$A_L^{avg} = \frac{2}{P_1 + P_2}\frac{N_{++} - N_{--}}{\Sigma N_i} \tag{7.8}$$

$$A_{LL} = \frac{1}{P_1 P_2}\frac{N_{++} + N_{--} - N_{+-} - N_{-+}}{\Sigma N_i} \tag{7.9}$$

$$\epsilon_{Null} = \frac{N_{+-} - N_{-+}}{\Sigma N_i} = A_L(P_1 - P_2) \tag{7.10}$$

where $\Sigma N_i \equiv N_{++} + N_{--} + N_{+-} + N_{-+}$ is the sum over all four helicity states. $A_L^{blue}$ and $A_L^{yellow}$ are the independent asymmetries measured for each beam, while $A_L^{avg}$ is the single-spin asymmetry of interest, which combines the results from the two beams. For the remainder of this chapter, $A_L^{avg}$ will be referred to as $A_L$. The longitudinal double-spin asymmetry, $A_{LL}$, is the asymmetry more commonly associated with measurements of the gluon polarization at RHIC, but has been recently discussed for $W$ production [108] as well. The asymmetry denoted $\epsilon_{Null}$ is a null test, and is expected to be very small when the two beams have similar polarization due to the fact that it effectively contains a factor $(P_1 - P_2)$ in the raw asymmetry. This provides a consistency test of the process of spin-sorting the yields, which is useful as a cross check for the other physics asymmetries.

## 7.2 Beam Polarization

The results of the polarimeter analysis for the data taken in 2009 are reported in Ref. [10], which contains polarization values for each RHIC fill. The CNI and hydrogen gas-jet target polarimeters used in the determination of the beam polarizations are described in Sec. 2.1.2. Figure 7.1 shows the measured polarization values during the $\sqrt{s} = 500$ GeV portion of the run for both the blue and yellow beams.

For the asymmetry analysis, 30 RHIC fills (listed in Appendix B) were used, with a total sampled luminosity of $\sim$12 pb$^{-1}$. The average polarizations from these fills for the blue and yellow beams were 0.38 $\pm$ 8.3% and 0.40 $\pm$ 12.1%, respectively. The relative systematic uncertainty for the sum of the beam polarizations, $P_1 + P_2$, relevant for the measurement of $A_L$ in Eq. 7.8, was reported to be 9.2% [10].

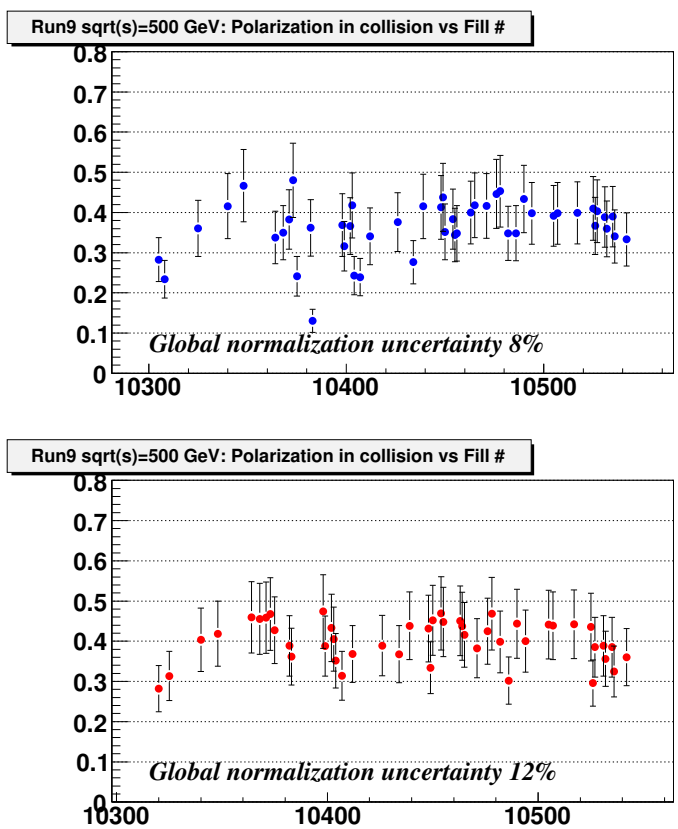


Figure 7.1: Polarization of the blue (top) and yellow (bottom) beams corrected for polarization profile vs. RHIC fill number, as reported in Ref. [10].

## 7.3 Spin Patterns

The order of the helicity states by bunch number (*i.e.,* the spin pattern) is different for the two beams, to ensure that the four possible helicity combinations are all colliding in every given fill. A cartoon of one particular spin pattern for the two beams at the STAR interaction region, shown in Fig. 7.2, illustrates how each of the four helicity combinations is sampled every fourth bunch in this spin pattern. There were four such polarization patterns that were rotated through from fill to fill during the 2009 data taking. During each fill, the intended polarization pattern and the intensity of each bunch was broadcast by the RHIC Collider-Accelerator Department (CAD) and recorded in an offline STAR database, to be used in sorting the spin-dependent yields.

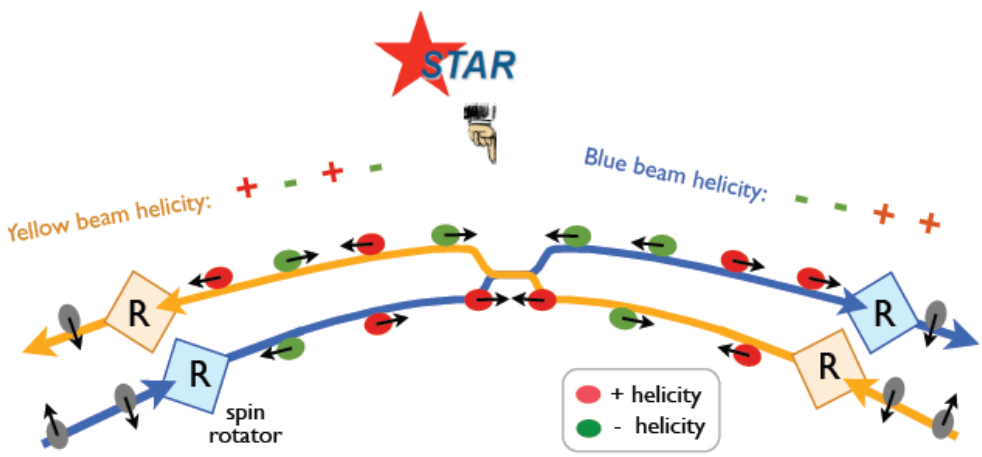


Figure 7.2: Cartoon of one particular spin pattern for the blue and yellow beams colliding at the STAR interaction region.

The spin patterns of the two beams, as broadcast by CAD, must then be translated into the spins of the protons colliding from a crossing of two bunches at the STAR interaction region. There are 120 bunches possible in the RHIC rings, though only ∼109 of them are typically filled in each ring. The ∼11 missing bunches in each ring are known as the abort gaps, and provide a fingerprint to identify which bunches identified by CAD are actually colliding in the STAR interaction region. Using these unique identifiers relates the spin pattern broadcast by CAD to the combination of helicities for each bunch crossing observed

at STAR. This assignment of the proton helicities in each bunch crossing is recorded in an offline database, and was used to determine the yield of $W$s in each helicity configuration. During the 2009 run four different fill polarization patterns were used, denoted as P1 through P4. The polarization state of the two proton bunches in a bunch crossing recorded in the STAR terminology is the 'spin-4' value. The spin-4 value corresponds to a specific combination of polarization states for the blue and yellow beams, listed in Table 7.1, in that particular bunch crossing at STAR. The correlation of the spin-4 value and the bunch crossing ID at STAR is shown in Fig. 7.3, for the four different fill polarization patterns. Each polarization pattern is clearly unique, and the abort gaps (where one beam's bunch is not filled for that bunch crossing) can be seen by the lower yield for bunch crossing IDs $\sim$ 29-39 and 111-119. The abort gap bunches are assigned an invalid spin-4 value, as these events are beam-background induced.

| spin-4 value | Blue Beam Helicity | Yellow Beam Helicity |
|---|---|---|
| 5 | $-$ | $-$ |
| 6 | $-$ | $+$ |
| 9 | $+$ | $-$ |
| 10 | $+$ | $+$ |

Table 7.1: Correspondence of spin-4 value and helicity state of the blue and yellow colliding beams at STAR.

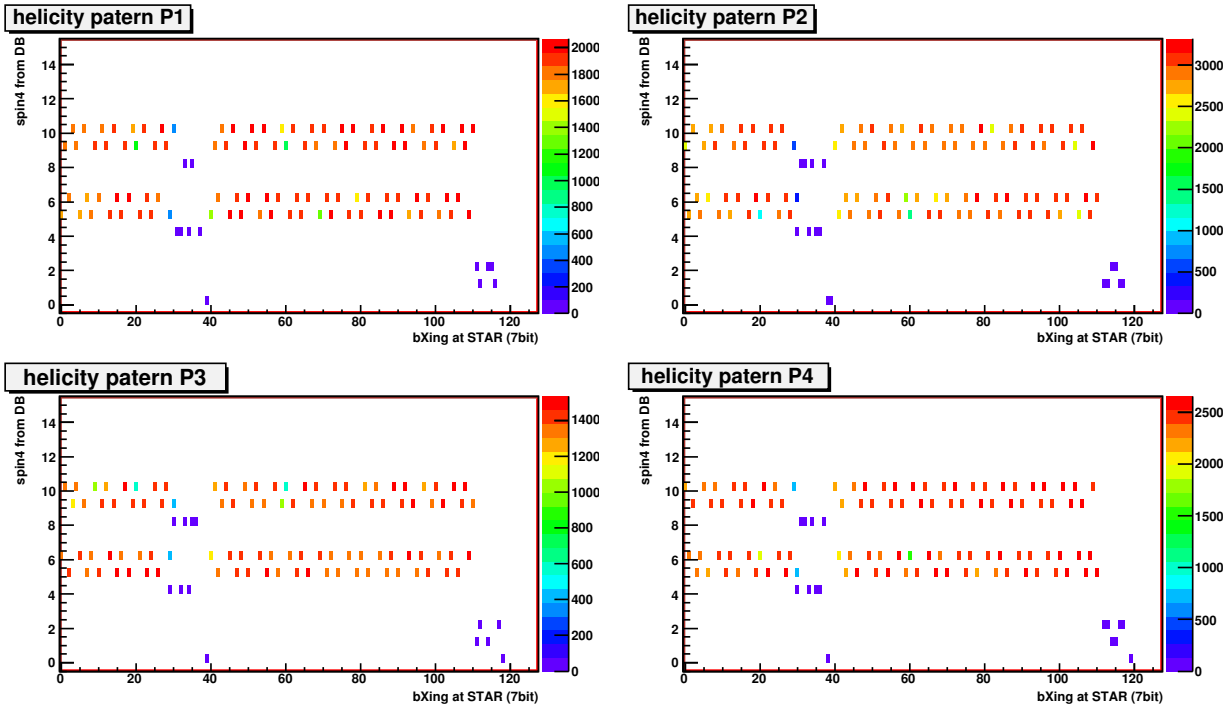


Figure 7.3: Correlation of STAR spin-4 value (*i.e.*, two-beam helicity combination) and the bunch crossing ID at STAR for each of the four fill polarization patterns used in 2009.

## 7.4 Relative Luminosity

In the expressions for the spin-sorted yields (Eqs. 7.2-7.5), there is a multiplicative factor for the luminosity integrated by the particular spin state. Ideally each spin state would integrate the same luminosity, since each spin state is represented in every fill and alternated from bunch to bunch. However, some bunches may be more (or less) intense than others, which results in small deviations from this ideal setup. Thus, for the computation of the spin asymmetries, a relative luminosity correction is applied to normalize the yields from each spin state relative to the others. The relative luminosity factor for the $i^{th}$ spin state ($i = ++, +-, -+, --$) is defined as $R_i \equiv L_0/(4L_i)$, where $L_i$ is the integrated luminosity for the specific spin state and $L_0 = \Sigma_i L_i$ is the sum over all spin states. Accounting for this correction to Eq. 7.8 results in the following expression for the longitudinal single-spin asymmetry:

$$A_L = \frac{2}{P_1 + P_2} \frac{R_{++}N_{++} - R_{--}N_{--}}{\Sigma R_i N_i}. \tag{7.11}$$

The relative luminosity factors for each spin state were determined using a statistically independent set of QCD background events, for which parity conservation in QCD requires that $A_L$=0. These events were selected using some of the same conditions as for the $W$ candidates, but also requiring two conditions to select QCD background events and assure no contamination from $W$ events. The specific requirements for this sample are that the event satisfy the trigger condition for this analysis (Sec. 3.1), reconstruct a high $p_T$ track pointing to the BEMC towers (Sec. 4.2.2), that the ratio of 2×2 to 4×4 tower $E_T$ is *below* 0.95 (opposite that of the $W$ candidate requirement, see Sec. 4.2.3), and that the 2×2 BEMC tower cluster $E_T$ be less than 20 GeV.

Because $R_i$ is a simple ratio of luminosities, it is unnecessary to know the absolute luminosity of the dataset ($L_0$) to apply the relative luminosity correction. Instead, a simple ratio formed from the QCD background event sample is used. $R_i$ can be written as $R_i = \Sigma_j N_j^{bkgd}/(4N_i^{bkgd})$, where $N_i^{bkgd}$ is the yield from the statistically independent set of

QCD background events (described above) in the $i^{th}$ spin state. The yield of these QCD background events in each helicity configurations is given in Table 7.2 along with the relative luminosity correction, $R_i$, and its uncertainty.

| Blue Beam Helicity | Yellow Beam Helicity | Background Yield | $R_i$ (error=$1/\sqrt{N}$) |
|---|---|---|---|
| + | + | 18595 | 1.002 ± 0.007 |
| + | − | 18439 | 0.993 ± 0.007 |
| − | + | 18472 | 0.995 ± 0.007 |
| − | − | 18740 | 1.010 ± 0.007 |

Table 7.2: Spin-dependent yields for the QCD background events used for relative luminosity corrections and the relative luminosity correction factors, $R_i$.

## 7.5 Background Corrections

So far, the equations given in this chapter for calculating the single-spin asymmetry $A_L^W$ have been limited by the fact that they assume no background in the $W$ candidate yield. The corrections for the polarized and unpolarized background from the sources described in Sec. 5.1 are discussed in this section.

In Eq. 7.11 in the previous section, the spin-dependent values $N_{++}, N_{+-}, ...$ are the yields of all candidates satisfying the $W$ selection requirements in a given spin state with no background subtraction. We will label this as the "observed" asymmetry, $A_L^{obs}$, as it is the asymmetry for all $W$ candidate events. This observed asymmetry can be decomposed into the contributions from real $W$ events and background, written as

$$A_L^{obs} = (f_W + f_{W\to\tau\nu})\, A_L^W + f_Z A_L^Z + f_{\mathrm{EEMC}} A_L^{\mathrm{EEMC}} + f_{\mathrm{QCD}} A_L^{\mathrm{QCD}}, \tag{7.12}$$

where $A_L^W$ is the single-spin asymmetry of interest for $W$ production, $A_L^Z$ is the single-spin asymmetry for $Z$ contamination of the $W$ yield, and $A_L^{\mathrm{EEMC}}$ and $A_L^{\mathrm{QCD}}$ are the single-spin asymmetries for the second EEMC and data-driven QCD backgrounds, respectively. The $f$'s are the fractions of each background component contained in the $W$ candidate yield, which are determined with the background estimation procedures described in Sec. 5.1. It should be noted that, in contrast to the $W^\pm$ cross section measurements, the $W \to \tau\nu$ channel is not a background for the $W^\pm$ single-spin asymmetry measurement. Aside from the fact that the $E_T^e$ for $W \to \tau\nu$ events is preferentially smaller than the $E_T^e$ for $W \to e\nu$ events, the $A_L$ for $W \to \tau\nu$ and $W \to e\nu$ should be identical. This is why the fractions $f_W$ and $f_{W\to\tau\nu}$ are multiplied by the same $A_L^W$ asymmetry factor in Eq. 7.12 above.

Equation 7.12 can then be solved for the asymmetry of interest, $A_L^W$, as a function of the observed asymmetry, background fractions, and background asymmetries:

$$A_L^W = \frac{A_L^{obs} - \left(f_Z A_L^Z + f_{\mathrm{EEMC}} A_L^{\mathrm{EEMC}} + f_{\mathrm{QCD}} A_L^{\mathrm{QCD}}\right)}{1 - f_Z - f_{\mathrm{EEMC}} - f_{\mathrm{QCD}}}. \tag{7.13}$$

The values for the $f$'s are known from background estimations similar to those in Sec. 5.1, and are given in Table 7.3. The observed asymmetry, $A_L^{obs}$, is directly measured from the spin-dependent yields. The other asymmetries were estimated using NLO calculations and data.

In addition to predictions for the $A_L^W$ asymmetry of most interest, the CHE NLO program [9] provides predictions for $A_L^Z$ as well. The value of $A_L^Z$ is computed within the phase space kinematics expected for $Z \to e^+e^-$ events which could contaminate the $W \to e\nu$ signal. In particular, we expect these to be dominated by events where one $e^\pm$ is in the BEMC ($|\eta_{e_1}| < 1$) and the other is outside the detector acceptance ($\eta_{e_2} < -1$ or $\eta_{e_2} > 2$). The computed value of this asymmetry is $A_L^Z = -0.06$, and a conservative systematic uncertainty of $\pm$ 50% is used, as a more accurate systematic uncertainty on the NLO calculation is difficult to obtain. For the asymmetry of the second EEMC background, we take $A_L^{\mathrm{EEMC}} = 0.3\ A_L^Z$ based on the contamination of the second EEMC background from $Z$ decays found in Sec. 5.1. $A_L^{\mathrm{QCD}}$ is the asymmetry of the remainder of the QCD background which is assumed to be negligible due to the very small contamination of the data-driven QCD background from $Z$ decays obtained by the veto described in Sec. 5.1.5.

The final expression used to calculate the $W$ single-spin asymmetry $A_L^W$ can be written in a simplified form as:

$$A_L^W = \frac{1}{\beta}\frac{2}{P_1 + P_2}\frac{R_{++}N_{++} - R_{--}N_{--}}{\Sigma R_i N_i} - \frac{\alpha}{\beta}, \tag{7.14}$$

where $\beta = 1 - f_Z - f_{\mathrm{EEMC}} - f_{\mathrm{QCD}}$ is the background dilution factor, and $\alpha \equiv f_Z A_L^Z + f_{\mathrm{EEMC}} A_L^{\mathrm{EEMC}}$ is the polarized background correction. Both $\alpha$ and $\beta$ are calculated independently for $W^+$ and $W^-$ and are given in Table 7.3.

| | $W^+$ | $W^-$ |
|---|---|---|
| $f_Z$ | 0.0198 ± 0.004 | 0.0565 ± 0.013 |
| $f_{\mathrm{EEMC}}$ | 0.0195 ± 0.006 | 0.0719 ± 0.022 |
| $f_{\mathrm{QCD}}$ | 0.0232 ± 0.015 | 0.0336 ± 0.020 |
| $\alpha$ | -0.002 ± 0.001 | -0.005 ± 0.002 |
| $\beta$ | 0.938 ± 0.017 | 0.838 ± 0.032 |

Table 7.3: Summary of background contributions to the "observed" $A_L$ (see Eq. 7.14).

## 7.6 Results

After the $W$ candidate yields have been spin-sorted, the results for each of the asymmetries given in Eqs. 7.6-7.10 (after correcting for relative luminosity and backgrounds as discussed in Secs. 7.4 and 7.5, respectively) are shown in Fig. 7.4. The asymmetries are calculated from the sample of events that satisfy all the $W \to e\nu$ signal requirements with $|\eta_e| < 1$ and $25 < E_T^e < 50$ GeV. An additional condition was also placed on the product of the candidate charge sign and $1/p_T$ (*i.e.,* $Q/p_T$), as shown in Fig. 2 of Ref. [67], to reduce contamination from possible mis-reconstructed charge signs. The double-spin asymmetries, $A_{LL}$, have somewhat larger uncertainties as they contain a factor of $1/P^2$ (as opposed to $1/P$ for $A_L$) and do not provide much insight with the current dataset. The $\epsilon_{Null}$ asymmetries are consistent with zero as expected providing additional confidence in our spin-sorting technique.

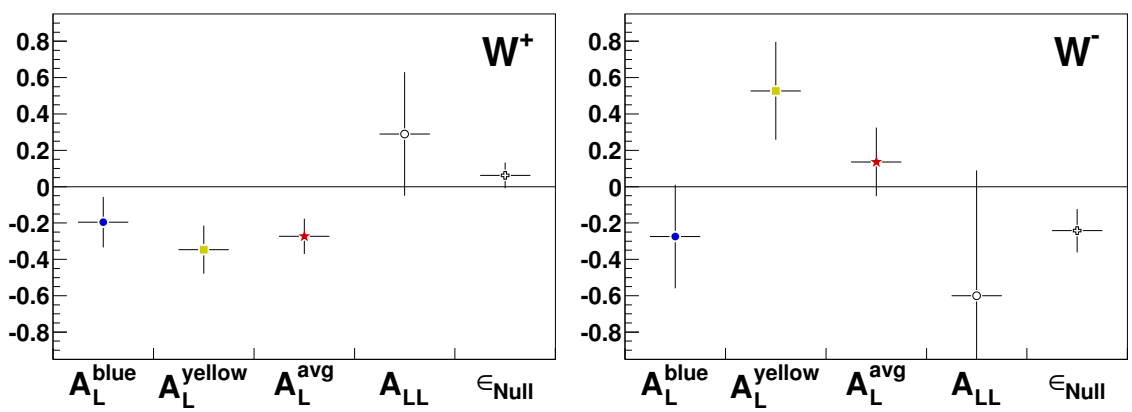


Figure 7.4: Spin asymmetries, defined in Eqs. 7.6-7.10 and corrected for relative luminosity and backgrounds, for $W^+$ (left) and $W^-$ (right) with $|\eta_e| < 1$ and $25 < E_T^e < 50$ GeV.

The quantity of primary interest, $A_L^{avg}$, is given explicitly by Eq. 7.14. The measured values for $|\eta_e| < 1$ and $25 < E_T^e < 50$ GeV are:

$$A_L^{W^+} = -0.27 \pm 0.10 \text{ (stat) } \pm 0.02 \text{ (syst)}$$

$$A_L^{W^-} = \ \ 0.14 \pm 0.19 \text{ (stat) } \pm 0.02 \text{ (syst)}$$

These measured values for the $A_L$ asymmetries are also shown in Fig. 7.5, along with theoretical predictions for the asymmetries from both the RHICBOS [56] and CHE [9] calculations. The statistical uncertainties on the measured $A_L$ values are shown by the black error bars, while the systematic uncertainty, shown as the gray band, is computed as the quadrature sum of the contributions from the polarized and unpolarized background factors ($\alpha$ and $\beta$). The overall normalization uncertainty due to the 9.2% uncertainty on the polarization sum $P_1 + P_2$ is not included in the displayed systematic uncertainty. An explanation of the theoretical calculations shown in Fig. 7.5, as well as the polarized PDFs used, can be found in Sec. 1.2. However, it is useful to point out here that by integrating the $e^{\pm}$ yields over $|\eta_e| < 1$, the measured $A_L^W$ are sensitive to a combination of quark and antiquark polarizations. The $A_L^{W^+}$ asymmetry is found to be negative and in good agreement with theoretical expectations in a region where the asymmetry is primarily related to the large $u$ quark polarization. The uncertainty for $A_L^{W^-}$ is signficantly larger (due to its smaller cross section), but the central value is positive, as expected.

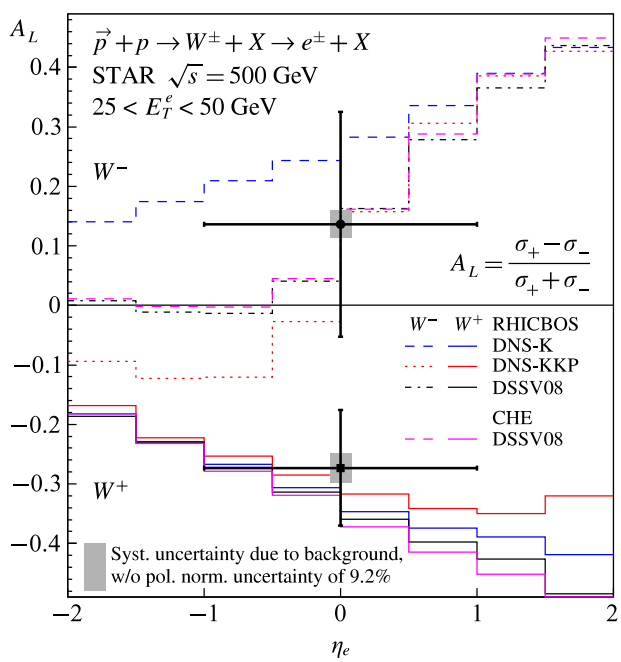


Figure 7.5: Longitudinal single-spin asymmetry, $A_L$, for $W^{\pm}$ production as a function of $e^{\pm}$ pseudorapidity.

# Chapter 8

# Conclusions and Outlook

The spin and flavor structure of the proton have been the subject of experimental study for more than two decades, yet still possess a fundamental challenge in QCD. In particular, a deeper understanding of the observed flavor asymmetry of the light antiquark momentum distributions is integral to furthering our knowledge of the mechanism(s) responsible for the production of sea quarks in the proton. The study of $W$ boson production in polarized $pp$ collisions provides a new technique to probe both the unpolarized $\bar{d}/\bar{u}$ flavor asymmetry, as well as the flavor-separated antiquark helicity distributions, which are currently not well constrained. These observables should provide new insights into the origin of the light quark sea of the proton.

In polarized $pp$ collisions, $W$ bosons are produced through the fusion of a quark and an antiquark from the colliding protons (*i.e.,* $u + \bar{d} \rightarrow W^+$ and $d + \bar{u} \rightarrow W^-$), and can be reconstructed through their leptonic decay, $W \rightarrow e\nu$. The large acceptance of the STAR detector at RHIC was used in the reconstruction of $W \rightarrow e\nu$ candidate events to identify isolated, high-$E_T$ electrons and positrons at mid-rapidity ($|\eta_e| < 1$). The undetected neutrino in $W \rightarrow e\nu$ events results in an event topology with a large missing transverse energy when compared to typical QCD background di-jet events. The final selection of $W$ candidates takes advantage of this difference in event topologies using a signed $P_T$-balance requirement,

while the selection of $Z \to e^+e^-$ candidates identifies pairs of isolated, high-$E_T$ $e^\pm$ candidates.

The measurements presented here are based on data recorded in longitudinally polarized $pp$ collisions at $\sqrt{s} = 500$ GeV in 2009, with an integrated luminosity of 13.2 pb$^{-1}$. Measurements of the cross sections for $W^+ \to e^+\,\nu_e$ and $W^- \to e^-\,\bar{\nu}_e$ production were presented, as well as first measurements of the $Z/\gamma^* \to e^+e^-$ production cross section at $\sqrt{s} = 500$ GeV$\dot{\text{P}}$redictions from NLO and resummed theoretical calculations are in good agreement with the measured values. This serves as a necessary validation of the theoretical framework in the (well understood) unpolarized case, which provides confidence in its use in global analyses of the polarized spin asymmetry observables. In addition, a first measurement of the $W^+/W^-$ cross section ratio at $\sqrt{s} = 500$ GeV was presented and the results were found to be consistent with theoretical expectations. The measurement of the $W^+/W^-$ cross section ratio is currently limited by statistical uncertainties, and future high-statistics measurements of this quantity will provide a new technique to study the $\bar{d}/\bar{u}$ flavor asymmetry of the antiquark sea.

First measurements of the parity-violating single-spin asymmetry $A_L$ for $W^\pm$ production were also presented. These results establish $W$ production as a unique tool for the study of the spin structure of the sea quarks inside the proton. Theoretical predictions from NLO and resummed calculations using recent polarized PDFs were shown to be in good agreement with the measured asymmetries. Anticipated future measurements with increased statistics and higher beam polarizations, carried out at both mid-rapidity and forward rapidity (with the Forward GEM Tracker upgrade [8]), will provide important new constraints on the $\bar{d}$ and $\bar{u}$ polarized PDFs.

# Appendix A

# Jet finding parameters

```
//set the analysis cuts: (see StJetMaker/StppJetAnalyzer.h -> class StppAnaPars )
StppAnaPars* anapars = new StppAnaPars();
anapars->setFlagMin(0); //track->flag() > 0
anapars->setNhits(12); //track->nHitsFit()>10
anapars->setCutPtMin(0.2); //track->pt() > 0.2
anapars->setAbsEtaMax(2.0); //abs(track->eta())<1.6
anapars->setJetPtMin(3.5);
anapars->setJetEtaMax(100.0);
anapars->setJetEtaMin(0);
anapars->setJetNmin(0);
//Setup the cone finder (See StJetFinder/StConeJetFinder.h -> class StConePars)
StConePars* cpars = new StConePars();
cpars->setGridSpacing(105, -3.0, 3.0, 120, -pi, pi); //include EEMC
cpars->setConeRadius(0.7);
cpars->setSeedEtMin(0.5);
cpars->setAssocEtMin(0.1);
cpars->setSplitFraction(0.5);
```

```
cpars->setPerformMinimization(true);

cpars->setAddMidpoints(true);

cpars->setRequireStableMidpoints(true);

cpars->setDoSplitMerge(true);

cpars->setDebug(true);
```

# Appendix B

# RHIC Fill Polarization Values

The RHIC polarization group has reported the measured values of the blue and yellow beam polarizations in Ref. [10]. The measured asymmetries integrate the average $A_L$ over all fills using the average of the beam polarizations listed in Table B, without any luminosity weighting.

| fill | blue pol | estat | esyst | yellow pol | estat | esyst |
|---|---|---|---|---|---|---|
| 10407 | 0.2392 | 0.0063 | 0.0459 | 0.3141 | 0.007 | 0.0603 |
| 10412 | 0.3407 | 0.0058 | 0.0704 | 0.3682 | 0.0057 | 0.0707 |
| 10415 | 0.225 | 0.0072 | 0.0432 | 0.2822 | 0.0079 | 0.0542 |
| 10426 | 0.3762 | 0.01 | 0.0722 | 0.3888 | 0.0093 | 0.0746 |
| 10434 | 0.2763 | 0.0087 | 0.0531 | 0.3676 | 0.0072 | 0.0706 |
| 10439 | 0.4153 | 0.0067 | 0.0797 | 0.4382 | 0.0061 | 0.0841 |
| 10448 | 0.4127 | 0.008 | 0.0792 | 0.4314 | 0.0083 | 0.0828 |
| 10449 | 0.4378 | 0.0093 | 0.0841 | 0.334 | 0.0082 | 0.0641 |
| 10450 | 0.3518 | 0.0081 | 0.0691 | 0.452 | 0.0076 | 0.0868 |
| 10454 | 0.3833 | 0.013 | 0.0736 | 0.4692 | 0.0132 | 0.0901 |
| 10455 | 0.3438 | 0.0081 | 0.066 | 0.4481 | 0.0076 | 0.086 |
| 10463 | 0.4 | 0.0067 | 0.078 | 0.4506 | 0.0069 | 0.0865 |
| 10465 | 0.4182 | 0.0077 | 0.0803 | 0.4158 | 0.0083 | 0.0798 |
| 10476 | 0.4462 | 0.0073 | 0.0857 | 0.4248 | 0.0065 | 0.0816 |
| 10478 | 0.4529 | 0.0087 | 0.0886 | 0.4687 | 0.0096 | 0.09 |
| 10482 | 0.3479 | 0.0094 | 0.0668 | 0.3983 | 0.0079 | 0.0765 |
| 10486 | 0.3485 | 0.0083 | 0.0679 | 0.302 | 0.0072 | 0.058 |
| 10490 | 0.4338 | 0.0084 | 0.0833 | 0.4435 | 0.0084 | 0.0852 |
| 10494 | 0.3979 | 0.0093 | 0.0764 | 0.4003 | 0.0079 | 0.0769 |
| 10505 | 0.3917 | 0.0072 | 0.0752 | 0.4412 | 0.0092 | 0.0847 |
| 10507 | 0.3981 | 0.0077 | 0.0764 | 0.4385 | 0.0069 | 0.0842 |
| 10508 | 0.3794 | 0.0102 | 0.0728 | 0.3602 | 0.01 | 0.0692 |
| 10517 | 0.3989 | 0.009 | 0.0766 | 0.442 | 0.0095 | 0.0849 |
| 10525 | 0.4099 | 0.0094 | 0.0787 | 0.4354 | 0.0092 | 0.0836 |
| 10526 | 0.3668 | 0.0095 | 0.0704 | 0.2957 | 0.009 | 0.0568 |
| 10527 | 0.4032 | 0.0082 | 0.0774 | 0.3852 | 0.0075 | 0.074 |
| 10531 | 0.3887 | 0.0086 | 0.0746 | 0.3886 | 0.0079 | 0.0746 |
| 10532 | 0.3594 | 0.0087 | 0.069 | 0.3562 | 0.008 | 0.0684 |
| 10535 | 0.3897 | 0.0087 | 0.0748 | 0.3853 | 0.0081 | 0.074 |
| 10536 | 0.3406 | 0.0095 | 0.0654 | 0.3246 | 0.0121 | 0.0623 |
| Average | 0.376 | | | 0.396 | | |

Table B.1: Measured beam polarizations and uncertainties reported by the polarimetery group for the RHIC fills in 2009 used in the asymmetry analysis.

# Appendix C

# List of STAR Runs

**Runs without good spin information (only used in cross section analysis):**

R10076134 R10076136 R10076152 R10076153 R10076154 R10076161 R10078077 R10078078 R10078081 R10078082 R10078092 R10078093 R10078094 R10079002 R10079004 R10079005 R10079006 R10079007 R10079015 R10079016 R10079017 R10079027 R10079028 R10079030 R10079031 R10079033 R10079034 R10079035 R10079040 R10079042 R10079045 R10079046 R10079047 R10079049 R10079050 R10079057 R10079059 R10079060 R10079061 R10079062 R10079063 R10079069 R10079070 R10079071 R10079074 R10079078 R10079079 R10079080 R10079081 R10079129 R10079130 R10079131 R10079135 R10079137 R10079138 R10079139 R10080019 R10080020 R10080022 R10080040 R10080042 R10080061 R10080062 R10080076 R10080077 R10080078 R10080080 R10080081

**Runs with good spin information (used in both cross section and spin asymmetry analyses):**

R10081007 R10081013 R10081026 R10081027 R10081047 R10081053 R10081055 R10081056 R10081096 R10081102 R10081104 R10081107 R10081108 R10081110 R10081111 R10081112 R10081115 R10081117 R10082003 R10082005 R10082008 R10082011 R10082018 R10082021 R10082022 R10082027 R10082029 R10082031 R10082032 R10082035 R10082043 R10082071 R10082072 R10082073 R10082074 R10082075 R10082076 R10082077 R10082078 R10082083

R10082085 R10082091 R10082092 R10082093 R10082095 R10083013 R10083018 R10083019
R10083026 R10083027 R10083028 R10083032 R10083033 R10083034 R10083037 R10083040
R10083041 R10083045 R10083047 R10083052 R10083053 R10083054 R10083055 R10083056
R10083058 R10084010 R10084011 R10084021 R10084022 R10084024 R10085016 R10085017
R10085018 R10085019 R10085023 R10085024 R10085025 R10085026 R10085027 R10085028
R10085029 R10085030 R10085031 R10085032 R10085038 R10085039 R10085104 R10085107
R10085108 R10085109 R10085113 R10085114 R10085115 R10085131 R10085132 R10085133
R10085134 R10085135 R10085136 R10085140 R10086001 R10086007 R10086008 R10086015
R10086022 R10086023 R10086024 R10086037 R10086043 R10086044 R10086046 R10087001
R10087009 R10087011 R10087012 R10087018 R10087020 R10087021 R10087022 R10087023
R10087025 R10087028 R10087031 R10087032 R10087033 R10087034 R10087035 R10087036
R10087037 R10087041 R10087051 R10087052 R10087053 R10087054 R10087057 R10087058
R10087059 R10087062 R10087063 R10087065 R10087067 R10087069 R10087070 R10087071
R10087077 R10087078 R10087082 R10087084 R10087085 R10087088 R10087094 R10087096
R10087097 R10087114 R10087117 R10087119 R10087125 R10087126 R10088001 R10088010
R10088011 R10088013 R10088022 R10088024 R10088026 R10088027 R10088028 R10088029
R10088030 R10088031 R10088036 R10088058 R10088062 R10088063 R10088069 R10088070
R10088071 R10088075 R10088077 R10088081 R10088084 R10088085 R10088096 R10088102
R10088110 R10088111 R10088112 R10088113 R10088120 R10088121 R10089001 R10089004
R10089008 R10089010 R10089011 R10089015 R10089016 R10089019 R10089021 R10089023
R10089079 R10089080 R10089081 R10090001 R10090004 R10090005 R10090008 R10090013
R10090015 R10090017 R10090018 R10090019 R10090020 R10090022 R10090026 R10090027
R10090037 R10090038 R10090040 R10090042 R10090046 R10090047 R10090072 R10090074
R10090076 R10090079 R10090080 R10090081 R10090089 R10090095 R10090100 R10090108
R10090109 R10090111 R10090112 R10091089 R10091090 R10092002 R10092004 R10092009
R10092011 R10092021 R10092022 R10092023 R10092024 R10092027 R10092028 R10092029
R10092030 R10092031 R10092033 R10092034 R10092036 R10092037 R10092038 R10092039

R10092040 R10092042 R10092046 R10092047 R10092048 R10092049 R10092050 R10092084
R10092098 R10092102 R10092105 R10092107 R10093082 R10093083 R10093084 R10093131
R10094003 R10094005 R10094006 R10094007 R10094016 R10094019 R10094021 R10094022
R10094023 R10094024 R10094063 R10094067 R10094071 R10094073 R10094078 R10094084
R10094088 R10094089 R10094090 R10094092 R10094095 R10094096 R10094098 R10094099
R10094100 R10095022 R10095023 R10095024 R10095030 R10095036 R10095037 R10095039
R10095040 R10095041 R10095045 R10095046 R10095047 R10095048 R10095049 R10095050
R10095051 R10095052 R10095056 R10095057 R10095120 R10095121 R10095122 R10095125
R10096001 R10096002 R10096005 R10096006 R10096007 R10096008 R10096009 R10096014
R10096015 R10096019 R10096024 R10096025 R10096026 R10096027 R10096141 R10097003
R10097004 R10097005 R10097008 R10097012 R10097016 R10097019 R10097021 R10097022
R10097026 R10097028 R10097029 R10097030 R10097038 R10097040 R10097044 R10097045
R10097087 R10097089 R10097091 R10097102 R10097104 R10097106 R10097108 R10097110
R10097117 R10097118 R10097137 R10097140 R10097145 R10097146 R10097149 R10097153
R10098029 R10098035 R10098038 R10098040 R10098045 R10099028 R10099029 R10099055
R10099057 R10099066 R10099067 R10099071 R10099073 R10099074 R10099076 R10099077
R10099078 R10099185 R10099186 R10099187 R10099188 R10099189 R10099194 R10099195
R10100005 R10100006 R10100008 R10100013 R10100014 R10100015 R10100016 R10100017
R10100021 R10100028 R10100029 R10100032 R10100067 R10100068 R10100070 R10100071
R10100072 R10100077 R10100079 R10100081 R10100093 R10100095 R10100098 R10100164
R10100165 R10100166 R10100167 R10100169 R10100172 R10100175 R10100176 R10100177
R10100178 R10100179 R10100180 R10101001 R10101005 R10101006 R10101008 R10101009
R10101011 R10101016 R10101017 R10101018 R10101019 R10101020 R10101028 R10101029
R10101030 R10101037 R10101038 R10101039 R10101040 R10101059 R10101060 R10101061
R10101064 R10101065 R10101069 R10101070 R10101071 R10101074 R10101075 R10101076
R10101078 R10101081 R10101082 R10101083 R10101086 R10101088 R10101089 R10101090
R10101091 R10101092 R10101093 R10101094 R10102003 R10102031 R10102033 R10102036

R10102037 R10102039 R10102045 R10102046 R10102048 R10102050 R10102051 R10102055 R10102056 R10102062 R10102063 R10102065 R10102066 R10102069 R10102070 R10102094 R10102095 R10102096 R10102098 R10102100 R10102104 R10102105 R10102107 R10102108 R10102109 R10102110 R10102112 R10103001 R10103007 R10103008 R10103010 R10103011 R10103012 R10103015 R10103016 R10103017 R10103018 R10103027 R10103028 R10103031 R10103033 R10103034 R10103041 R10103042

# Bibliography


[1] A. Martin, W. Stirling, R. Thorne, and G. Watt, Parton distributions for the LHC, Eur. Phys. J. **C63**, 189 (2009), arXiv:0901.0002 [hep-ph].

[2] R. Towell *et al.* (E866/NuSea), Improved measurement of the anti-d / anti-u asymmetry in the nucleon sea, Phys. Rev. **D64**, 052002 (2001), arXiv:hep-ex/0103030 [hep-ex].

[3] A. Baldit *et al.* (NA51), Study of the isospin symmetry breaking the in the light quark sea of the nucleon from the Drell-Yan process, Phys. Lett. **B332**, 244 (1994).

[4] G. T. Garvey and J.-C. Peng, Flavor asymmetry of light quarks in the nucleon sea, Prog. Part. Nucl. Phys. **47**, 203 (2001), arXiv:nucl-ex/0109010 [nucl-ex].

[5] D. de Florian, R. Sassot, M. Stratmann, and W. Vogelsang, Extraction of Spin-Dependent Parton Densities and Their Uncertainties, Phys. Rev. **D80**, 034030 (2009), arXiv:0904.3821 [hep-ph].

[6] M. Alekseev *et al.* (COMPASS Collaboration), Quark helicity distributions from longitudinal spin asymmetries in muon-proton and muon-deuteron scattering, Phys. Lett. **B693**, 227 (2010), arXiv:1007.4061 [hep-ex].

[7] G. Bunce, N. Saito, J. Soffer, and W. Vogelsang, Prospects for spin physics at RHIC, Ann. Rev. Nucl. Part. Sci. **50**, 525 (2000), to be published in Dec. 2000 by Annual Reviews, arXiv:hep-ph/0007218 [hep-ph].

[8] B. Surrow *et al.*, Forward GEM Tracker Upgrade Proposal for the STAR experiment, Unpublished (2007).

[9] D. de Florian and W. Vogelsang, Helicity Parton Distributions from Spin Asymmetries in W-Boson Production at RHIC, Phys. Rev. **D81**, 094020 (2010), arXiv:1003.4533 [hep-ph].

[10] I. Alekseev *et al.*, Run 9 pC Polarimeter Analysis. http://www4.rcf.bnl.gov/ cnipol/pubdocs/Run09Offline/, .

[11] F. Halzen and A. D. Martin, Quarks and Leptons: An Introductory Course in Modern Particle Physics, John Wiley and Sons, Inc. (1984).

[12] R. E. Taylor, Deep inelastic scattering: The early years, Rev. Mod. Phys. **63**, 573 (1991).

[13] H. W. Kendall, Deep inelastic scattering: Experiments on the proton and the observation of scaling, Rev. Mod. Phys. **63**, 597 (1991).

[14] J. I. Friedman, Deep inelastic scattering: Comparisons with the quark model, Rev. Mod. Phys. **63**, 615 (1991).

[15] J. Bjorken, Asymptotic Sum Rules at Infinite Momentum, Phys.Rev. **179**, 1547 (1969).

[16] E. D. Bloom, D. H. Coward, H. DeStaebler, J. Drees, G. Miller, L. W. Mo, R. E. Taylor, M. Breidenbach, J. I. Friedman, G. C. Hartmann, and H. W. Kendall, High-Energy Inelastic $e-p$ Scattering at 6° and 10°, Phys. Rev. Lett. **23**, 930 (1969).

[17] M. Breidenbach, J. I. Friedman, H. W. Kendall, E. D. Bloom, D. H. Coward, H. DeStaebler, J. Drees, L. W. Mo, and R. E. Taylor, Observed Behavior of Highly Inelastic Electron-Proton Scattering, Phys. Rev. Lett. **23**, 935 (1969).

[18] R. P. Feynman, Very High-Energy Collisions of Hadrons, Phys. Rev. Lett. **23**, 1415 (1969).

[19] J. D. Bjorken and E. A. Paschos, Inelastic Electron-Proton and $\gamma$-Proton Scattering and the Structure of the Nucleon, Phys. Rev. **185**, 1975 (1969).

[20] M. Gell-Mann, A schematic model of baryons and mesons, Physics Letters **8**, 214 (1964).

[21] G. Zweig, An $SU_3$ model for strong interaction symmetry and its breaking: Part I, CERN Preprint 8182/TH401 (1964).

[22] G. Zweig, An $SU_3$ model for strong interaction symmetry and its breaking: Part II, CERN Preprint 8419/TH412 (1964).

[23] J. Kuti and V. F. Weisskopf, Inelastic Lepton-Nucleon Scattering and Lepton Pair Production in the Relativistic Quark-Parton Model, Phys. Rev. D **4**, 3418 (1971).

[24] C. G. Callan and D. J. Gross, High-Energy Electroproduction and the Constitution of the Electric Current, Phys. Rev. Lett. **22**, 156 (1969).

[25] D. J. Gross and F. Wilczek, Ultraviolet Behavior of Non-Abelian Gauge Theories, Phys. Rev. Lett. **30**, 1343 (1973).

[26] H. D. Politzer, Reliable Perturbative Results for Strong Interactions?, Phys. Rev. Lett. **30**, 1346 (1973).

[27] C. Alexandrou, Hadron structure in lattice QCD, Progress in Particle and Nuclear Physics **67**, 101 (2012).

[28] P. M. Nadolsky *et al.*, Implications of CTEQ global analysis for collider observables, Phys. Rev. **D78**, 013004 (2008), arXiv:0802.0007 [hep-ph].

[29] V. N. Gribov and L. N. Lipatov, Sov. J. Nucl. Phys. **15**, 438 (1972).

[30] G. Altarelli and G. Parisi, Nucl. Phys. **B126**, 298 (1977).

[31] Y. L. Dokshitzer, Sov. Phys. JETP **46**, 641 (1977).

[32] J. M. Conrad, M. H. Shaevitz, and T. Bolton, Precision measurements with high-energy neutrino beams, Rev. Mod. Phys. **70**, 1341 (1998), arXiv:hep-ex/9707015 [hep-ex].

[33] K. Gottfried, Sum rule for high-energy electron - proton scattering, Phys. Rev. Lett. **18**, 1174 (1967).

[34] P. Amaudruz *et al.* (New Muon Collaboration), The Gottfried sum from the ratio F2(n) / F2(p), Phys. Rev. Lett. **66**, 2712 (1991).

[35] M. Arneodo *et al.* (New Muon Collaboration), A Reevaluation of the Gottfried sum, Phys. Rev. **D50**, 1 (1994), revised version of CERN-PPE-93-117.

[36] S. Ellis and W. J. Stirling, Constraints on isospin breaking in the light quark sea from the Drell-Yan process, Phys. Lett. **B256**, 258 (1991).

[37] K. Ackerstaff *et al.* (HERMES Collaboration), The Flavor asymmetry of the light quark sea from semiinclusive deep inelastic scattering, Phys. Rev. Lett. **81**, 5519 (1998), arXiv:hep-ex/9807013 [hep-ex].

[38] R. Field and R. Feynman, Quark Elastic Scattering as a Source of High Transverse Momentum Mesons, Phys. Rev. **D15**, 2590 (1977).

[39] D. Ross and C. T. Sachrajda, Flavor Symmetry Breaking in anti-Quark Distributions, Nucl. Phys. **B149**, 497 (1979).

[40] F. M. Steffens and A. W. Thomas, The Flavor asymmetry of the nucleon sea, Phys. Rev. **C55**, 900 (1997), to appear in Phys. Rev. C Report-no: ADP-96-28/T227, arXiv:nucl-th/9612056 [nucl-th].

[41] J. Peng *et al.* (E866/NuSea Collaboration), Anti-d / anti-u asymmetry and the origin of the nucleon sea, Phys. Rev. **D58**, 092004 (1998), arXiv:hep-ph/9804288 [hep-ph].

[42] A. Szczurek, M. Ericson, H. Holtmann, and J. Speth, Testing the meson cloud in the nucleon in Drell-Yan processes, Nucl. Phys. **A596**, 397 (1996), arXiv:hep-ph/9602213 [hep-ph].

[43] P. Pobylitsa, M. V. Polyakov, K. Goeke, T. Watabe, and C. Weiss, Isovector unpolarized quark distribution in the nucleon in the large N(c) limit, Phys. Rev. **D59**, 034024 (1999), arXiv:hep-ph/9804436 [hep-ph].

[44] A. Dorokhov and N. Kochelev, Instanton induced asymmetric quark configurations in the nucleon and parton sum rules, Phys. Lett. **B304**, 167 (1993).

[45] C. Bourrely, J. Soffer, and F. Buccella, A Statistical approach for polarized parton distributions, Eur. Phys. J. **C23**, 487 (2002), 49 pages, 27 eps figures Report-no: CPT-2001/P.4205, UNIV. NAPLES DSF 29/2001, arXiv:hep-ph/0109160 [hep-ph].

[46] P. Reimer, D. Geesaman, *et al.*, Fermilab E906/SeaQuest Drell-Yan Proposal, Unpublished (2001).

[47] V. Hughes, V. Papavassiliou, R. Piegaia, K. Schuler, and G. Baum, The Integral of the Spin Dependent Structure Function G(1)p and the Ellis-Jaffe Sum Rule, Phys. Lett. **B212**, 511 (1988).

[48] J. Ashman *et al.* (European Muon Collaboration), An Investigation of the Spin Structure of the Proton in Deep Inelastic Scattering of Polarized Muons on Polarized Protons, Nucl. Phys. **B328**, 1 (1989).

[49] J. R. Ellis and R. L. Jaffe, A Sum Rule for Deep Inelastic Electroproduction from Polarized Protons, Phys. Rev. **D9**, 1444 (1974).

[50] R. Jaffe and A. Manohar, The G(1) Problem: Fact and Fantasy on the Spin of the Proton, Nucl. Phys. **B337**, 509 (1990), revised version.

[51] X.-D. Ji, Gauge invariant decomposition of nucleon spin and its spin - off, Phys. Rev. Lett. **78**, 610 (1997), arXiv:hep-ph/9603249 [hep-ph].

[52] B. Adeva *et al.* (Spin Muon Collaboration), Polarized quark distributions in the nucleon from semiinclusive spin asymmetries, Phys. Lett. **B420**, 180 (1998), arXiv:hep-ex/9711008 [hep-ex].

[53] A. Airapetian *et al.* (HERMES Collaboration), Quark helicity distributions in the nucleon for up, down, and strange quarks from semi-inclusive deep-inelastic scattering, Phys. Rev. **D71**, 012003 (2005), arXiv:hep-ex/0407032 [hep-ex].

[54] S. Kumano and M. Miyama, Polarized light anti-quark distributions in a meson cloud model, Phys. Rev. **D65**, 034012 (2002), arXiv:hep-ph/0110097 [hep-ph].

[55] M. Wakamatsu, Light flavor sea quark distributions in the nucleon in the SU(3) chiral quark soliton model. 1. Phenomenological predictions, Phys. Rev. **D67**, 034005 (2003).

[56] P. M. Nadolsky and C. Yuan, Single spin asymmetries with weak bosons at RHIC, Nucl. Phys. **B666**, 31 (2003), arXiv:hep-ph/0304002 [hep-ph].

[57] C. Albajar *et al.* (UA1), Intermediate Vector Boson Cross-Sections at the CERN Super Proton Synchrotron Collider and the Number of Neutrino Types, Phys. Lett. **B198**, 271 (1987).

[58] C. Albajar *et al.* (UA1), Studies of Intermediate Vector Boson Production and Decay in UA1 at the CERN Proton - Antiproton Collider, Z. Phys. **C44**, 15 (1989).

[59] J. Alitti *et al.* (UA2), Measurement of the W and Z Production Cross Sections atthe CERN anti-p p Collider, Z. Phys. **C47**, 11 (1990).

[60] J. Alitti *et al.* (UA2), A Measurement of the W and Z production cross-sections and a determination of $\Gamma(W)$ at the CERN anti-p p collider, Phys. Lett. **B276**, 365 (1992).

[61] F. Abe *et al.* (CDF), Measurement of $\sigma \cdot B(W \to e\nu)$ and $\sigma \cdot B(Z^0 \to e^+e^-)$ in $p\bar{p}$ collisions at $\sqrt{s} = 1.8$ TeV, Phys. Rev. Lett. **76**, 3070 (1996), arXiv:hep-ex/9509010 [hep-ex].

[62] A. Abulencia *et al.* (CDF), Measurements of inclusive W and Z cross sections in p anti-p collisions at $\sqrt{s} = 1.96$-TeV, J. Phys. **G34**, 2457 (2007), arXiv:hep-ex/0508029 [hep-ex].

[63] S. Abachi *et al.* (D0), $W$ and $Z$ boson production in $p\bar{p}$ collisions at $\sqrt{s} = 1.8$-TeV, Phys. Rev. Lett. **75**, 1456 (1995), arXiv:hep-ex/9505013 [hep-ex].

[64] B. Abbott *et al.* (D0), Extraction of the width of the $W$ boson from measurements of $\sigma(p\bar{p} \to W + X) \times B(W \to e\nu)$ and $\sigma(p\bar{p} \to Z + X) \times B(Z \to ee)$ and their ratio, Phys. Rev. **D61**, 072001 (2000), arXiv:hep-ex/9906025 [hep-ex].

[65] T. Aaltonen *et al.* (CDF Collaboration), First Run II Measurement of the $W$ Boson Mass, Phys. Rev. **D77**, 112001 (2008), arXiv:0708.3642 [hep-ex].

[66] V. M. Abazov *et al.* (D0 Collaboration), Measurement of the W boson mass, Phys. Rev. Lett. **103**, 141801 (2009), arXiv:0908.0766 [hep-ex].

[67] M. Aggarwal *et al.* (STAR), Measurement of the parity-violating longitudinal single-spin asymmetry for $W^{\pm}$ boson production in polarized proton-proton collisions at $\sqrt{s} = 500$ GeV, Phys. Rev. Lett. **106**, 062002 (2011), arXiv:1009.0326 [hep-ex].

[68] L. Adamczyk *et al.* (STAR Collaboration), Measurement of the $W \to e\nu$ and $Z/\gamma^* \to e^+e^-$ Production Cross Sections at Mid-rapidity in Proton-Proton Collisions at $\sqrt{s} = 500$ GeV, Phys. Rev. D **85**, 092010 (2012), arXiv:1112.2980 [hep-ex].

[69] A. Adare *et al.* (PHENIX), Cross Section and Parity Violating Spin Asymmetries of $W^{\pm}$ Boson Production in Polarized $p + p$ Collisions at $\sqrt{s} = 500$ GeV, Phys. Rev. Lett. **106**, 062001 (2011), arXiv:1009.0505 [hep-ex].

[70] G. Aad *et al.* (ATLAS), Measurement of the $W \to \ell\nu$ and $Z/\gamma^* \to \ell\ell$ production cross sections in proton-proton collisions at $\sqrt{s} = 7$ TeV with the ATLAS detector, JHEP **12**, 060 (2010), arXiv:1010.2130 [hep-ex].

[71] V. Khachatryan *et al.* (CMS), Measurements of Inclusive W and Z Cross Sections in pp Collisions at sqrt(s)=7 TeV, JHEP **01**, 080 (2011), arXiv:1012.2466 [hep-ex].

[72] S. Chatrchyan *et al.* (CMS), Measurement of the Inclusive W and Z Production Cross Sections in pp Collisions at sqrt(s) = 7 TeV, JHEP **10**, 132 (2011), arXiv:1107.4789 [hep-ex].

[73] J. Peng and D. Jansen, Probing $\bar{u}/\bar{d}$ asymmetry in the proton via $W$ and $Z$ production, Phys. Lett. **B354**, 460 (1995), arXiv:hep-ph/9508243 [hep-ph].

[74] G. Aad *et al.* (ATLAS), Measurement of the $W$ charge asymmetry in the $W \to \mu\nu$ decay mode in $pp$ collisions at $\sqrt{s} = 7$ TeV with the ATLAS detector, Phys. Lett. **B701**, 31 (2011), arXiv:1103.2929 [hep-ex].

[75] S. Chatrchyan *et al.* (CMS), Measurement of the lepton charge asymmetry in inclusive $W$ production in pp collisions at $\sqrt{s} = 7$ TeV, JHEP **04**, 050 (2011), arXiv:1103.3470 [hep-ex].

[76] I. Alekseev, C. Allgower, M. Bai, Y. Batygin, L. Bozano, *et al.*, Polarized proton collider at RHIC, Nucl. Instrum. Meth. **A499**, 392 (2003).

[77] A. Zelensky, J. Alessi, B. Briscoe, H. Huang, A. Kponou, *et al.*, Optically pumped polarized H- ion source for RHIC spin physics, Rev. Sci. Instrum. **73**, 888 (2002).

[78] V. Bargmann, L. Michel, and V. Telegdi, Precession of the polarization of particles moving in a homogeneous electromagnetic field, Phys. Rev. Lett. **2**, 435 (1959).

[79] L. Thomas, The kinematics of an electron with an axis, Philos. Mag. **3**, 1 (1927).

[80] Y. Derbenev, A. Kondratenko, S. Serednyakov, A. Skrinsky, G. Tumaikin, *et al.*, Radiative Polarization: Obtaining, Control, Using, Part.Accel. **8**, 115 (1978).

[81] W. MacKay, L. Ahrens, M. Bai, E. Courant, W. Fischer, *et al.*, Commissioning Spin Rotators in RHIC, Conf.Proc. **C030512**, 1697 (2003).

[82] I. Nakagawa *et al.*, Polarization measurements of RHIC-pp RUN05 using CNI pC-polarimeter, AIP Conf. Proc. **915**, 912 (2007).

[83] A. Zelenski, A. Bravar, D. Graham, W. Haeberli, S. Kokhanovsky, *et al.*, Absolute polarized H-jet polarimeter development, for RHIC, Nucl. Instrum. Meth. **A536**, 248 (2005).

[84] H. Okada, I. Alekseev, A. Bravar, G. Bunce, S. Dhawan, *et al.*, Measurement of the analyzing power in pp elastic scattering in the peak CNI region at RHIC, Phys. Lett. **B638**, 450 (2006), arXiv:nucl-ex/0502022 [nucl-ex].

[85] N. H. Buttimore, B. Kopeliovich, E. Leader, J. Soffer, and T. Trueman, The spin dependence of high-energy proton scattering, Phys. Rev. **D59**, 114010 (1999), arXiv:hep-ph/9901339 [hep-ph].

[86] K. H. Ackermann *et al.* (STAR), STAR detector overview, Nucl. Instrum. Meth. **A499**, 624 (2003).

[87] K. Adcox *et al.* (PHENIX Collaboration), PHENIX detector overview, Nucl. Instrum. Meth. **A499**, 469 (2003).

[88] M. Anderson *et al.* (STAR), The Star time projection chamber: A Unique tool for studying high multiplicity events at RHIC, Nucl. Instrum. Meth. **A499**, 659 (2003).

[89] J. Abele *et al.* (STAR Collaboration), The laser system for the STAR time projection chamber, Nucl. Instrum. Meth. **A499**, 692 (2003).

[90] F. Bergsma *et al.* (STAR), The STAR detector magnet subsystem, Nucl. Instrum. Meth. **A499**, 633 (2003).

[91] M. Beddo *et al.* (STAR), The STAR barrel electromagnetic calorimeter, Nucl. Instrum. Meth. **A499**, 725 (2003).

[92] C. Allgower *et al.* (STAR), The STAR endcap electromagnetic calorimeter, Nucl. Instrum. Meth. **A499**, 740 (2003).

[93] B. Surrow, The STAR forward GEM tracker, Nucl. Instrum. Meth. **A617**, 196 (2010).

[94] R. L. Jaffe and J. R. Primack, Production of weak-interaction bosons in high-energy proton proton collisions, Nucl. Phys. **B61**, 317 (1973).

[95] P. Cameron *et al.*, The RHIC Wall Current Monitor System, Proceedings of the 1999 PAC (1999).

[96] S. van der Meer, Calibration of the effective beam height in the ISR, CERN-ISR-PO **68-31** (1968).

[97] R. Corliss, Measurement of absolute luminsotiy for STAR BHT3 trigger for $p + p$ collisions at $\sqrt{s}$ of 500 GeV in 2009, Internal STAR Note , 533.

[98] J. R. Stevens, Run 9 Luminosity Measurement Corrections. http://drupal.star.bnl.gov/STAR/blog/stevens4/2011/jun/15/investigating-run-9-luminosity, .

[99] T. Sjostrand, S. Mrenna, and P. Z. Skands, PYTHIA 6.4 Physics and Manual, JHEP **05**, 026 (2006), arXiv:hep-ph/0603175.

[100] R. Brun *et al.*, GEANT: Simulation Program for Particle Physics Experiments. User Guide and Reference Manual, CERN-DD-78-2-REV (1978).

[101] C. Adler, A. Denisov, E. Garcia, M. J. Murray, H. Strobele, *et al.*, The RHIC zero degree calorimeter, Nucl. Instrum. Meth. **A470**, 488 (2001), arXiv:nucl-ex/0008005 [nucl-ex].

[102] R. Reed, Vertex Finding in Pile-up Rich Events for $p + p$ and $d$+Au Collisions at STAR, Presented at CHEP 2008, Internal STAR Note , 488.

[103] B. Abelev *et al.* (STAR), Longitudinal double-spin asymmetry and cross section for inclusive jet production in polarized proton collisions at $\sqrt{s} = 200$ GeV, Phys. Rev. Lett. **97**, 252001 (2006), arXiv:hep-ex/0608030 [hep-ex].

[104] http://www.star.bnl.gov/cgi bin/protected/cvsweb.cgi/StRoot/StJetMaker/, .

[105] A. Stahl, "$\tau$-Lepton Decay Parameters" in Nakamura *et al.* (Particle Data Group), Review of particle physics, J. Phys. G **G37**, 075021 (2010).

[106] G. J. Feldman and R. D. Cousins, A Unified approach to the classical statistical analysis of small signals, Phys. Rev. **D57**, 3873 (1998), arXiv:physics/9711021 [physics.data-an].

[107] K. Melnikov and F. Petriello, Electroweak gauge boson production at hadron colliders through $O(\alpha(s)^2)$, Phys. Rev. **D74**, 114017 (2006), arXiv:hep-ph/0609070 [hep-ph].

[108] Z.-B. Kang and J. Soffer, General positivity bounds for spin observables in particle inclusive production, Phys. Rev. **D83**, 114020 (2011), arXiv:1104.2920 [hep-ph]